USO Summer School *Solar Magnetism*,

June 28 – July 4, 2009, Dwingeloo, The Netherlands

MHD simulations

Oskar Steiner

Kiepenheuer-Institut für Sonnenphysik, Freiburg i.Br.

steiner@kis.uni-freiburg.de

Table of content

Table of content (cont.)

Table of content (cont.)

Part I: Conservation, Consistency, and Convergency

§ 1 Linear and non-linear advection equations

We start with the continuity equation as the reference equation for advection:

$$\frac{\partial \rho}{\partial t} + \boldsymbol{\nabla} \cdot (\rho \boldsymbol{v}) = 0 \ ,$$

in 1-D

$$\frac{\partial \rho}{\partial t} + \frac{\partial}{\partial x}(\rho u) = 0 \ .$$

With $u = \mathrm{const.}$ (the advection velocity) we get the *linear advection equation*

$$\frac{\partial \rho}{\partial t} + u \frac{\partial \rho}{\partial x} = 0 \ .$$

Its solution is

$$\rho(x,t) = \rho_0(x - ut) \ .$$

Linear and non-linear advection equations (cont.)

The initial density profile is simply moved (advected) with velocity u.

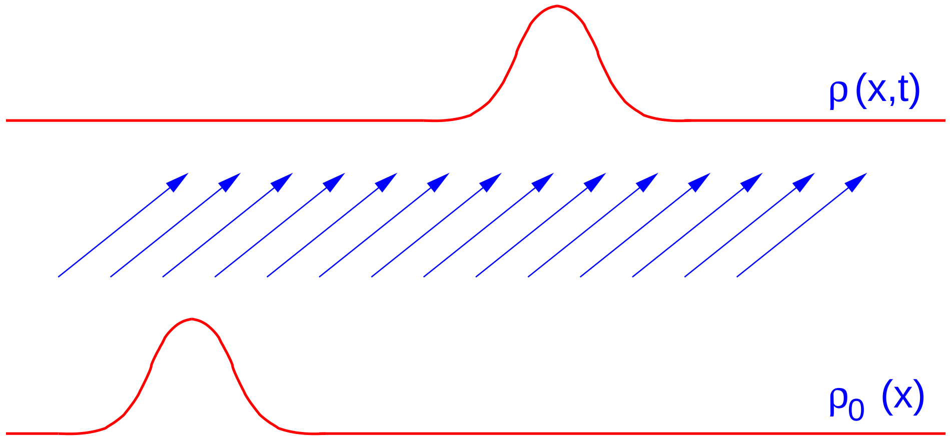

ρ is a "generalized density".

It is remarkable that Eulerian numerical schemes have generally difficulties to solve the linear advection equation accurately. Some amount of diffusion is unavoidable.

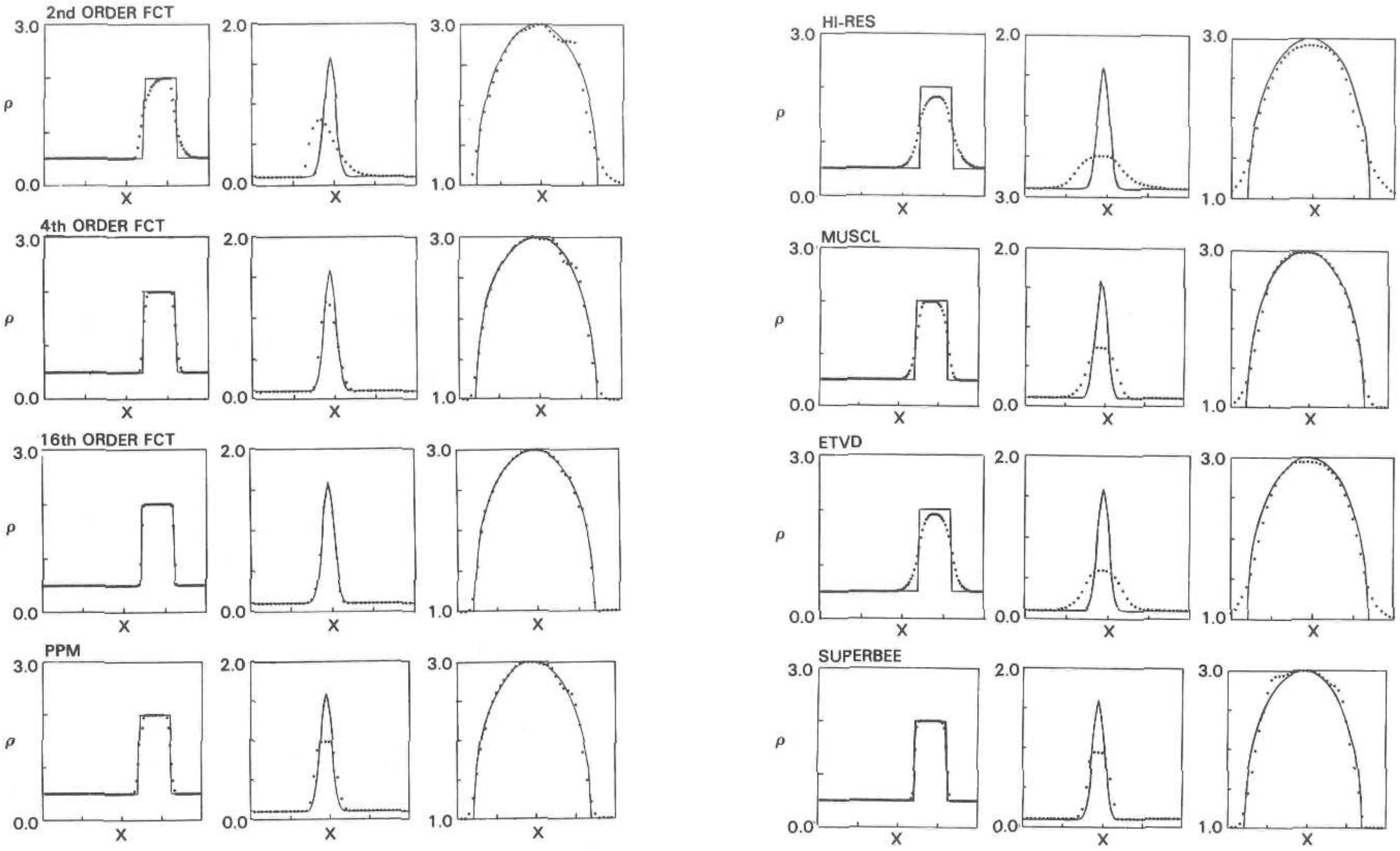

From *Oran & Boris (1987)*

Linear and non-linear advection equations (cont.)

We next consider the momentum equation

$$\frac{\partial}{\partial t}(\rho u) + \frac{\partial}{\partial x}(\rho u^2 + p) - \varepsilon\rho\frac{\partial^2 u}{\partial x^2} = 0\ ,$$

and assume $p = 0$:

$$u\frac{\partial\rho}{\partial t} + \rho\frac{\partial u}{\partial t} + u^2\frac{\partial\rho}{\partial x} + \rho 2u\frac{\partial u}{\partial x} - \varepsilon\rho\frac{\partial^2 u}{\partial x^2} = 0\ .$$

Using the continuity equation, the first term can be written as:

$$u\frac{\partial\rho}{\partial t} = -u\frac{\partial}{\partial x}(u\rho) = -u^2\frac{\partial\rho}{\partial x} - u\rho\frac{\partial u}{\partial x}$$

$$\Rightarrow \quad \rho\frac{\partial u}{\partial t} + \rho u\frac{\partial u}{\partial x} - \rho\varepsilon\frac{\partial^2 u}{\partial x^2} = 0\ .$$

Division by ρ and reordering terms leads to:

Burgers' equation

$$\boxed{\frac{\partial u}{\partial t} + u\frac{\partial u}{\partial x} = \varepsilon\frac{\partial^2 u}{\partial x^2}}$$

and the *inviscid Burgers' equation*

$$\boxed{u_t + uu_x = 0}$$

Linear and non-linear advection equations (cont.)

Burgers' equation

$$\boxed{\frac{\partial u}{\partial t} + u\frac{\partial u}{\partial x} = \varepsilon\frac{\partial^2 u}{\partial x^2}}$$

and the *inviscid Burgers' equation*

$$\boxed{u_t + uu_x = 0}$$

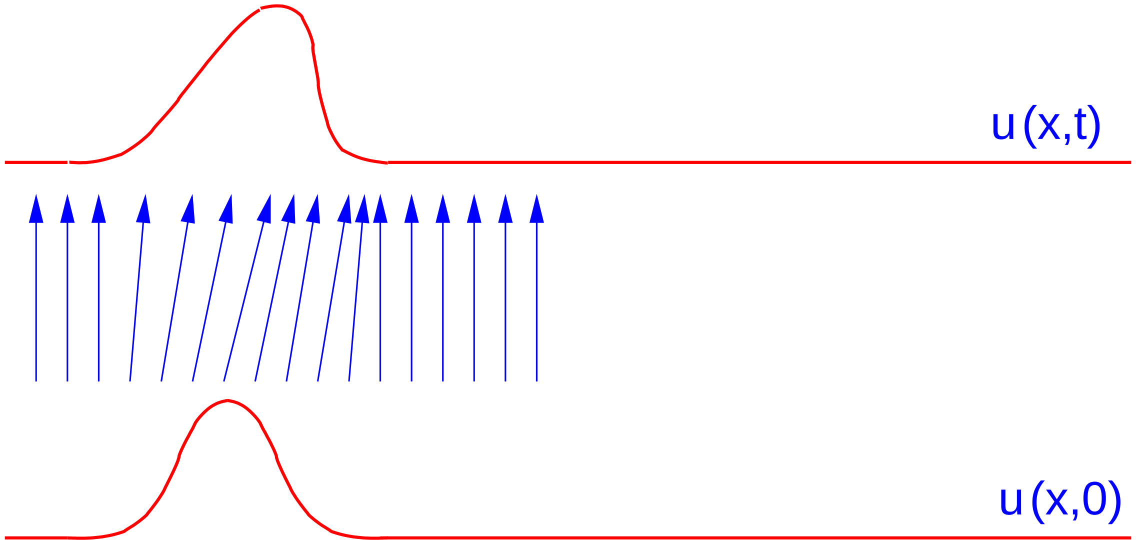

Solutions to the inviscid Burgers equation $u_t + uu_x = 0$:

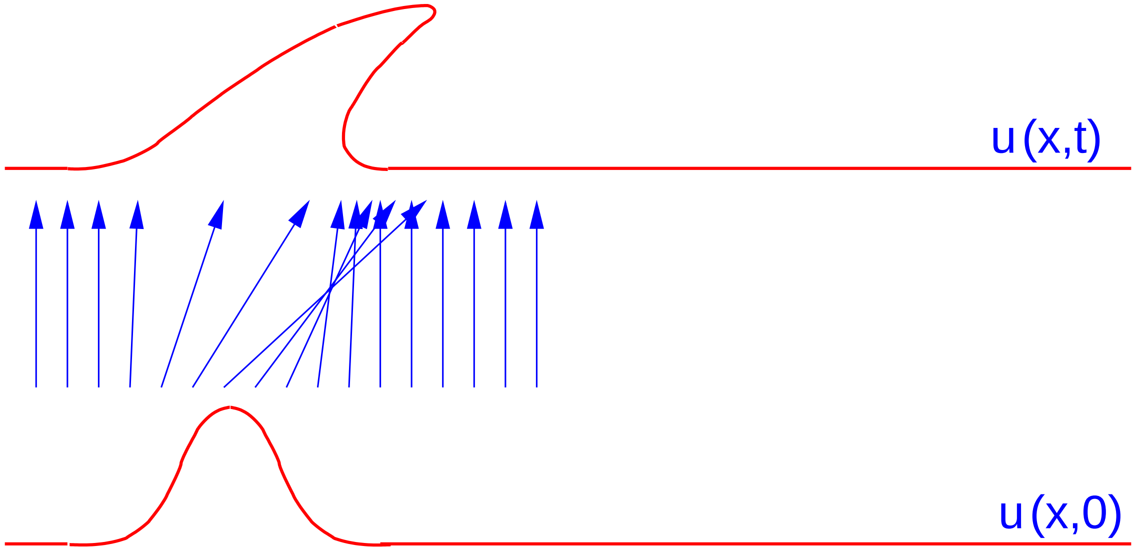

Solutions to the Burgers equation $u_t + uu_x = \varepsilon u_{xx}$:

Consider the inviscid Burgers equation $u_t + uu_x = 0$ with the initial data

$$u_0 = \begin{cases} 1 & \text{for} \quad x \leq 0 \\ 0 & \text{for} \quad x > 0 \end{cases}$$

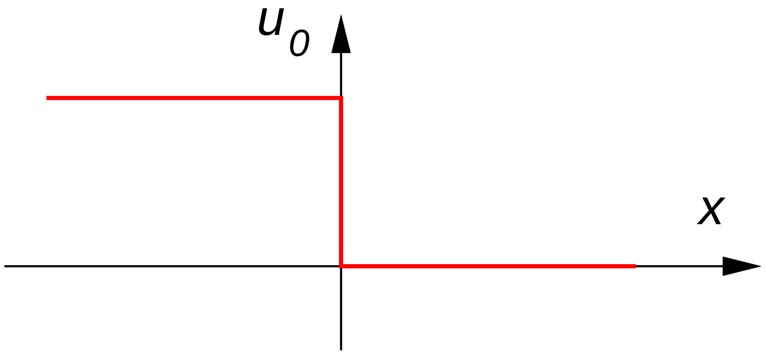

and construct a straightforward discretization:

$$\frac{U_j^{n+1} - U_j^n}{k} + U_j^n \left(\frac{U_j^n - U_{j-1}^n}{h} \right) = 0 \; ,$$

which is an ‘upwind” or “donor cell” scheme. How does this scheme handle the discontinuity of the initial data ?

First we rewrite the scheme in explicite form:

$$U_j^{n+1} = U_j^n - \frac{k}{h} U_j^n \left(U_j^n - U_{j-1}^n \right) \ .$$

Next we compute the first time step:

$$\begin{aligned}
\text{for} \quad x < 0: \quad U_j^1 &= 1 - \frac{k}{h} 1 \, (1 - 1) &= 1 \ , \\
\text{for} \quad x > 0: \quad U_j^1 &= 0 - \frac{k}{h} 0 \, (0 - 0) &= 0 \ , \\
\text{for} \quad U_{j-1} = 1 \quad \text{and} \quad U_j = 0: \quad U_j^1 &= 0 - \frac{k}{h} 0 \, (0 - 1) &= 0 \ .
\end{aligned}$$

First we rewrite the scheme in explicite form:

$$U_j^{n+1} = U_j^n - \frac{k}{h} U_j^n \left(U_j^n - U_{j-1}^n \right) \; .$$

Next we compute the first time step:

$$\begin{aligned}
\text{for} \quad x < 0: \quad U_j^1 &= 1 - \frac{k}{h} 1 \,(1-1) \quad &= 1 \, , \\
\text{for} \quad x > 0: \quad U_j^1 &= 0 - \frac{k}{h} 0 \,(0-0) \quad &= 0 \, , \\
\text{for} \quad U_{j-1} = 1 \quad \text{and} \quad U_j = 0: \quad U_j^1 &= 0 - \frac{k}{h} 0 \,(0-1) \quad &= 0 \, .
\end{aligned}$$

$\Rightarrow$ *After one time step we recover the initial data again!*

Whatever step size h and k we choose, the shock front stays at the same position.

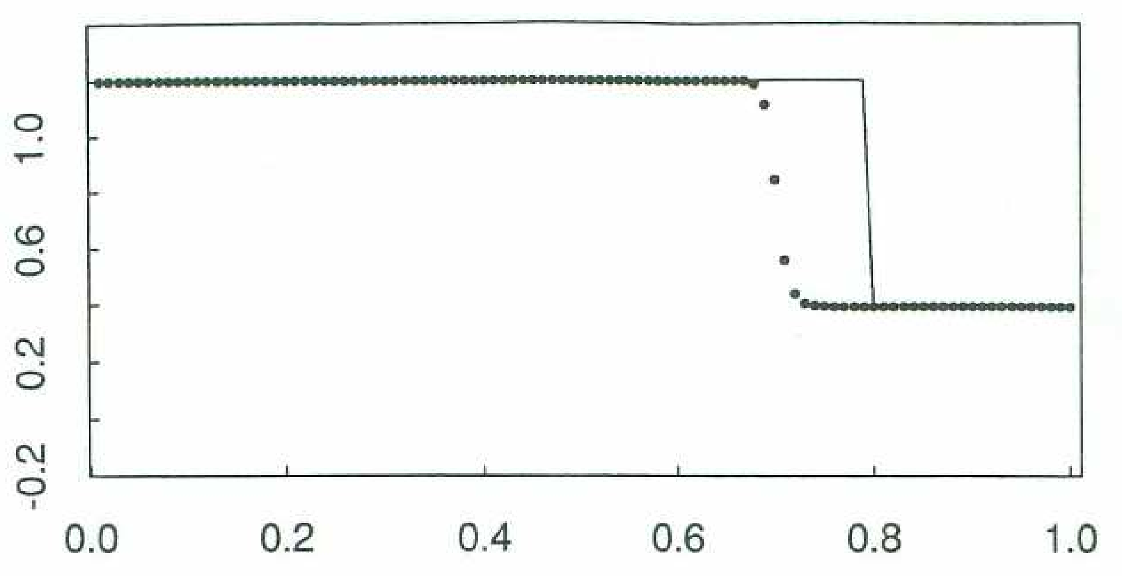

From *R.J. LeVeque (1992)*

True (solid curve) and computed (dotted curve) solution to Burgers' equation with adjacent initial data and using the upwind scheme. Note that the *shock speed is wrong*.

$$u_0 = \begin{cases} 1.2 & \text{for} \quad x \leq 0 \\ 0.4 & \text{for} \quad x > 0 \end{cases}$$

§ 2 Conservative methods

Def.: A scheme is in *conservation law form* if it has the form

$$
\begin{aligned}
U_j^{n+1} &= U_j^n - \frac{k}{h}\left[F(U_{j-p}^n, U_{j-p+1}^n, \ldots, U_{j+q}^n)\right. \\
&\quad \left. - F(U_{j-p-1}^n, U_{j-p}^n, \ldots, U_{j+q-1}^n)\right] \ .
\end{aligned}
$$

F is called the *numerical flux function* .

A good way to obtain conservation law form ist to start discretization from the conservative form of the PDE.

For eample in case of the inviscid Burgers equation:

$$\begin{aligned} \text{quasi linear form} \quad &: \quad u_t + u u_x &= 0\,, \\ \text{conservative form} \quad &: \quad u_t + \left(\tfrac{1}{2}u^2\right)_x &= 0\,. \end{aligned}$$

Using the same upwind discretization as before but starting from the conservative form of the PDE we obtain:

$$\frac{U_j^{n+1} - U_j^n}{k} + \frac{1}{h}\left[\frac{1}{2}(U_j^n)^2 - \frac{1}{2}(U_{j-1}^n)^2\right] = 0\,.$$

The explicit form is

$$U_j^{n+1} = U_j^n - \frac{k}{h}\left[\frac{1}{2}(U_j^n)^2 - \frac{1}{2}(U_{j-1}^n)^2\right] = 0 \ ,$$

which is distinctly different from the difference equation that we had before:

$$U_j^{n+1} = U_j^n - \frac{k}{h} U_j^n \left(U_j^n - U_{j-1}^n\right) \ .$$

The first equation has the form

$$U_j^{n+1} = U_j^n - \frac{k}{h}\left[F(U_j^n) - F(U_{j-1}^n)\right] \ ,$$

hence, it is in conservation law form according to the definition. Applying it to the same initial data as before produces the correct solution with the correct shock speed.

Conservative methods (cont.)

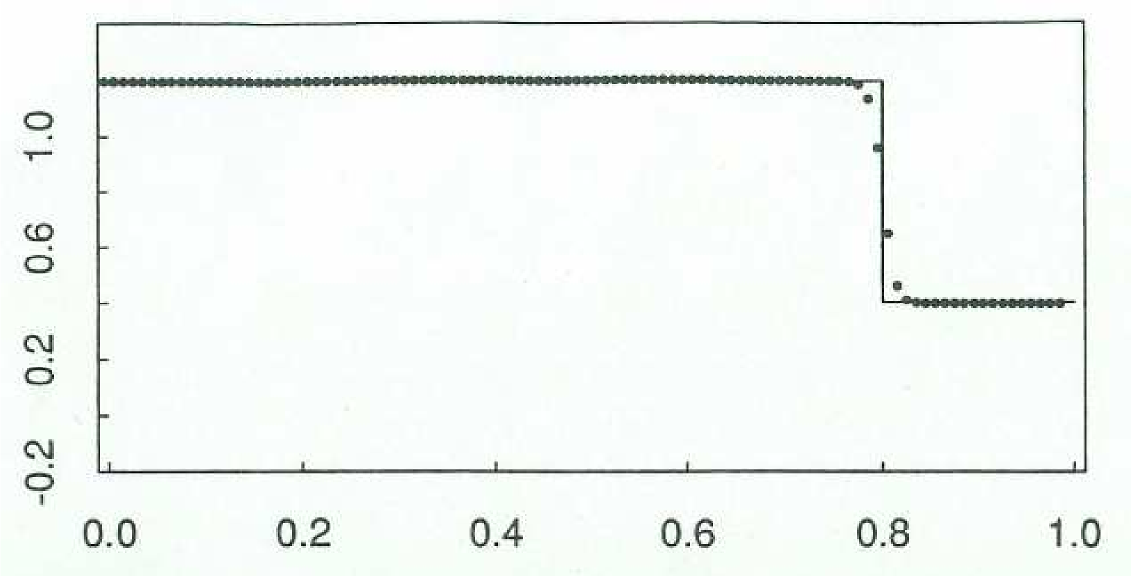

From *R.J. LeVeque (1992)*

True (solid curve) and computed (dotted curve) solution to Burgers' equation with adjacent initial data and using the *conservative upwind scheme*. Note that the *shock speed is correct*.

$$u_0 = \begin{cases} 1.2 & \text{for} \quad x \le 0 \\ 0.4 & \text{for} \quad x > 0 \end{cases}$$

§ 3 Conservation, Consistency, Convergence

Def.: U_j^n: *numerical solution* at grid point j and time $t = (n-1)k$ $\quad$ ($k = \Delta t$)

u_j^n: $= u(x_j, t_n)$ *exact solution* at grid point j and time $t = (n-1)k$

$\mathcal{H}_k$: explicit *numerical scheme* using time steps k so that

$$U^{n+1} = \mathcal{H}_k(U^n)$$

L_k: *local truncation error*

$$L_k(x_j, t) = \frac{1}{k}\left[u(x_j, t+k) - \mathcal{H}_k(u(\,.\,, t); x_j)\right]$$

Then, a method is *consistent* if $\|L_k(\,.\,, t)\| \to 0 \quad$ as $\quad k \to 0$,

where $\|v\| := \int_{-\infty}^{\infty} |v(x)| \mathrm{d}x, \quad$ while $\quad k/h =$ const

A *scheme in conservation law form*

$$
\begin{aligned}
U_j^{n+1} \quad &= \quad U_j^n - \frac{k}{h}\left[F(U_{j-p}^n, U_{j-p+1}^n, \ldots, U_{j+q}^n)\right. \\
&\qquad \left. - F(U_{j-p-1}^n, U_{j-p}^n, \ldots, U_{j+q-1}^n)\right]
\end{aligned}
$$

is *consistent* with the conservative PDE

$$
\frac{\partial u}{\partial t} + \frac{\partial}{\partial x}(f(u))
$$

if

$$
\boxed{\text{F(u,u,...,u) = f(u)}}
$$

and there exists a K such that

$$
|F(U_{j-p}, \ldots, U_{j+q}) - f(u)| \leq K \max_{-p \leq i \leq q} |U_{j+1} - u| \,.
$$

For example Burgers' equation and its conservative upwind scheme are consistent:

$$F(U_j) = \frac{1}{2}(U_j)^2 \Rightarrow F(u) = \frac{1}{2}u^2 = f$$

This scheme is conservative *and* consistent!

Theorem of Lax and Wendroff (1960)

Consider a sequence of grids, indexed by $l = 1, 2, \ldots$ with mesh parameters $k_l, h_l \to 0$ as $l \to \infty$. Let $U_l(x,t)$ denote the numerical solution computed with a *consistent* and *conservative* method on the lth grid. Suppose that U_l converges* to a function u as $l \to \infty$.

Then $u(x,t)$ is *a weak solution of the conservation law*.

* Convergence in the following sense:

Over every bounded set $\Omega = [a,b] \times [0,T]$

$$\int_0^T \int_a^b |U_l(x,t) - u(x,t)| \mathrm{d}x \, \mathrm{d}t \to 0 \text{ as } l \to \infty$$

and $$\mathrm{TV}(U(\,.\,,t)) < R \quad 0 \le t \le T, l = 1, 2, \ldots$$

where $$\mathrm{TV}(v) = \sup \textstyle\sum_{j=1}^{N} |v(\xi_j) - v(\xi_{j-1})|$$

§ 4 Theorem of Godunov

Def.: If we have initial data that are monotone increasing or decreasing, e.g.,

$U_j^0 \geq U_{j+1}^0 \quad \forall j$ (monotonically decreasing) and the numerical scheme produces solutions with

$U_j^n \geq U_{j+1}^n \quad \forall j$ and n, then the *scheme* is said to be *monotone*.

For example, the upwind scheme is a monotone scheme.

Theorem of Godunov (1959)

A *linear, monotonicity preserving* method is at most *first order* accurate.

A scheme $\mathcal{H}$ is linear if $\mathcal{H}(\mathcal{U}+\mathcal{V}) = \mathcal{H}(\mathcal{U}) + \mathcal{H}(\mathcal{V})$.

(It has the general form $\displaystyle U_i^{n+1} = \sum_{k=-k_L}^{k_R} b_k U_{i+k}^n \,, \quad k_L \,, k_R \in \mathbb{N}^+$)

References

LeVeque, R.J.: 2002, Finite Volume Methods for Hyperbolic Problems, Cambridge University Press, Cambridge

LeVeque, R.J.: 1992, Numerical Methods for Conservation Laws, Birkhäuser Verlag, Basel

LeVeque, R.J., Mihalas, D., Dorfi, E.A., and Müller, E.: 1998, Computational Methods for Astrophysical Fluid Flow, O. Steiner & A. Gautschy (eds.), Springer-Verlag, Berlin

Part II: Riemann solvers

§ 5 Three major advancements in the numerical treatment of the hydrodynamic equations

Three major progresses in computational fluid dynamics of the past 50 years include:

- the *conservative formulation* of the computational scheme in terms of finite volumes,
- the technique of approximate *Riemann-solvers* for the computation of numerical fluxes,
- the *flux-limiter* technique for maintaining stability and monotonicity of higher-order accurate scheme.

§ 6 Conservation laws – finite volumes

Consider the continuity equation:

$$\rho_t + \nabla \cdot (\rho \mathbf{u}) = 0 \; . \tag{1}$$

Integration over a finite volume, $\mathcal{V}$, and time period, T, leads to the *integral form* of this equation:

$$\int_{\mathcal{V}} \rho(T, \mathbf{x}) \mathrm{d}V - \int_{\mathcal{V}} \rho(0, \mathbf{x}) \mathrm{d}V = \int_0^T \oint_{\partial\mathcal{V}} (\rho \mathbf{u}) \cdot \mathbf{n} \, \mathrm{d}s \, \mathrm{d}t \tag{2}$$

Solutions to Eq. (2) are called *weak solutions* to the partial differential equation, Eq. (1). Additionally to the solutions of Eq. (1), the set of solutions to Eq. (2) encompasses discontinuous solutions, because no derivatives appear in Eq. (2). Discontinuous solutions to the Euler equations represent *shock fronts* of the real world.

Conservation laws – finite volumes (cont.)

Consider the mass conservation in a one-dimensional tube:

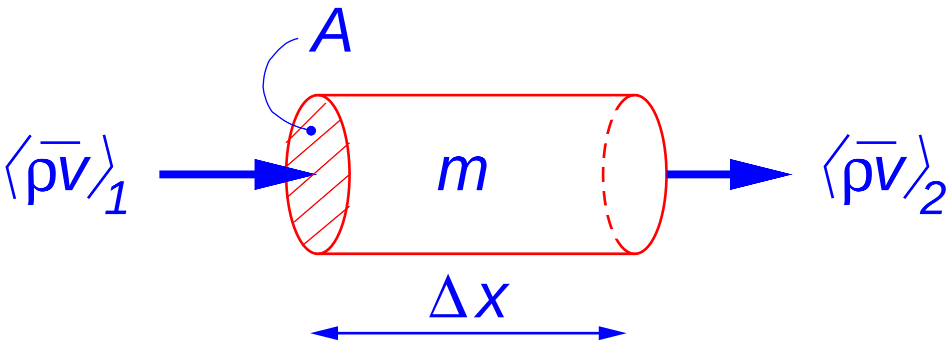

$$m(t+\Delta t) = m(t) + \langle\overline{\rho v}\rangle_1 A\Delta t - \langle\overline{\rho v}\rangle_2 A\Delta t \tag{3}$$

$$\langle\rho\rangle(t+\Delta t) = \langle\rho\rangle(t) - \frac{\Delta t}{\Delta x}\left(\langle\overline{\rho v}\rangle_2 - \langle\overline{\rho v}\rangle_1\right) \tag{4}$$

Eq. (4) has the form of a *conservative finite volume scheme*.

in the limit of $\Delta x \rightarrow 0$ and $\Delta t \rightarrow 0$ $\quad \dfrac{\partial\rho}{\partial t} = \dfrac{\partial(\rho v)}{\partial x}$

But Eq. (3) is *identical to the integral form* Eq. (2):

$$\int_{\mathcal{V}} \rho(T,\mathbf{x})\mathrm{d}V - \int_{\mathcal{V}} \rho(0,\mathbf{x})\mathrm{d}V = \int_0^T \oint_{\partial\mathcal{V}} (\rho\mathbf{u})\cdot\mathbf{n}\,\mathrm{d}s\,\mathrm{d}t$$

Conservation laws – finite volumes (cont.)

The conservative, finite volume formulation has three highly desirable properties:

- Conserved quantities (mass, momentum, energy) remain accurately conserved
- Discontinuous solutions are include by solving the integral form of the partial differential equation
- It fulfills one of two requirements of the theorem of Lax and Wendroff (1960) that says:

  The approximate solution that is computed with a *consistent* and *conservative* scheme *converges* to a weak solution of the conservation law.

Conservation laws – finite volumes (cont.)

Euler's equation in one dimension is given by

$$\mathbf{q}_t + \mathbf{f}(\mathbf{q})_x = 0 \ , \qquad \mathbf{q}_i^{n+1} = \mathbf{q}_i^n + \frac{\Delta t}{\Delta x}\left[\mathbf{f}_{i-1/2} - \mathbf{f}_{i+1/2}\right] ,$$

where

$$\mathbf{q} = \begin{pmatrix} \rho \\ \rho u \\ E \end{pmatrix} \qquad \mathbf{f}(\mathbf{q}) = \begin{pmatrix} \rho u \\ \rho u^2 + p \\ u(E+p) \end{pmatrix}$$

In 3-D we have

$$\mathbf{q}_t + \mathbf{f}(\mathbf{q})_x + \mathbf{g}(\mathbf{q})_y + \mathbf{h}(\mathbf{q})_z = 0 \ ,$$

with

$$\mathbf{q} = \begin{pmatrix} \rho \\ \rho u \\ \rho v \\ \rho w \\ E \end{pmatrix} \qquad \mathbf{f}(\mathbf{q}) = \begin{pmatrix} \rho u \\ \rho u^2 + p \\ \rho u v \\ \rho u w \\ u(E+p) \end{pmatrix} \qquad \cdots$$

§ 7 Riemann solvers

A conservative finite volume scheme is an exact representation of the integral form of the partial differential equation of the conservation law. The problem consists in computing the correct flux function $\mathbf{f}(\mathbf{q})$, i.e., $\langle\overline{\rho v}\rangle$ in the case of the continuity equation.

It turns out that these fluxes can be computed *exactly*.

Idea of S.K. Godunov (1959): Piecewise constant reconstruction with discontinuities at cell interfaces

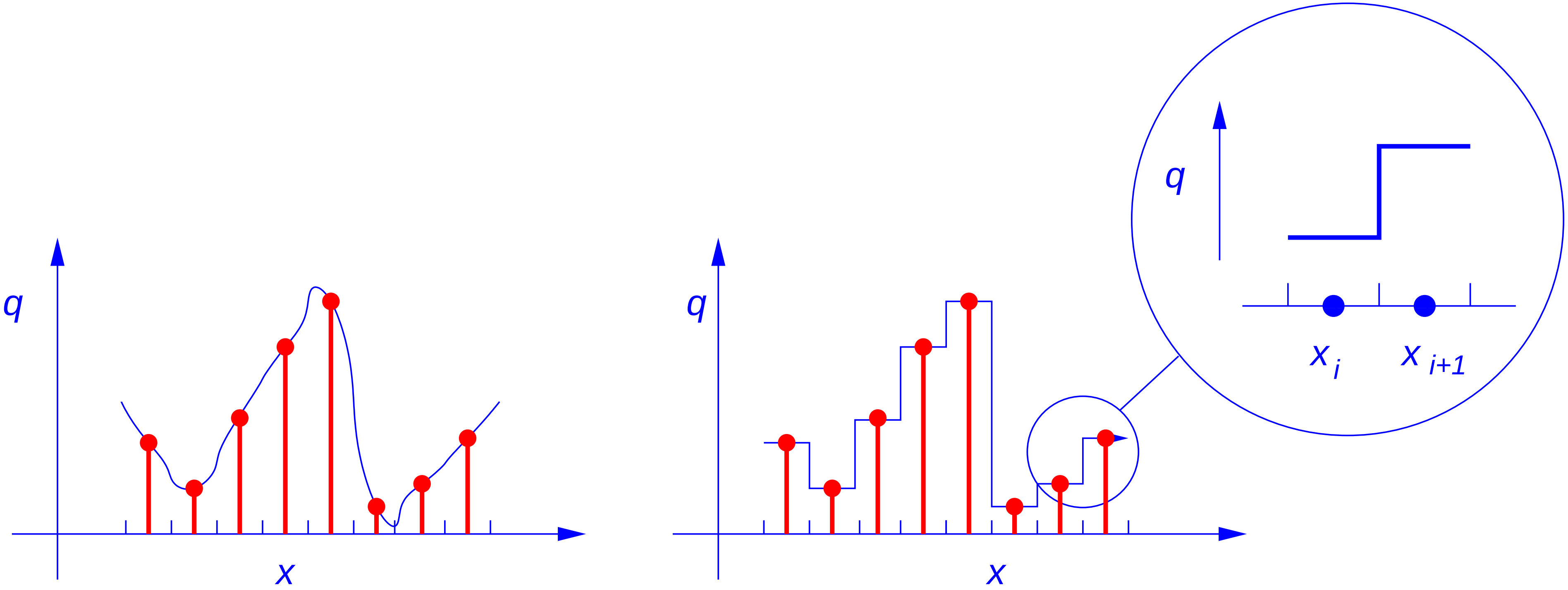

The shock-tube problem

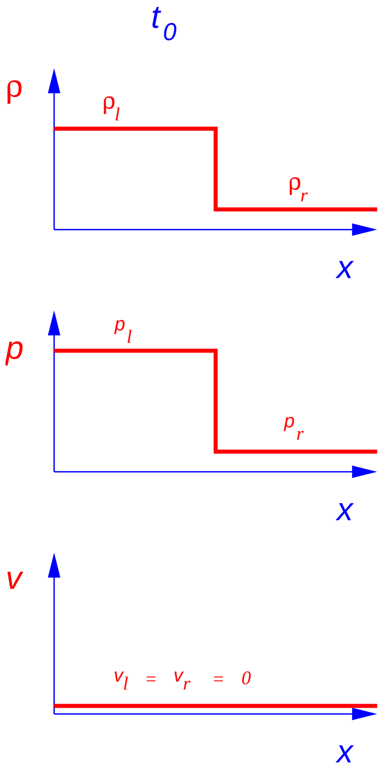

The shock-tube problem

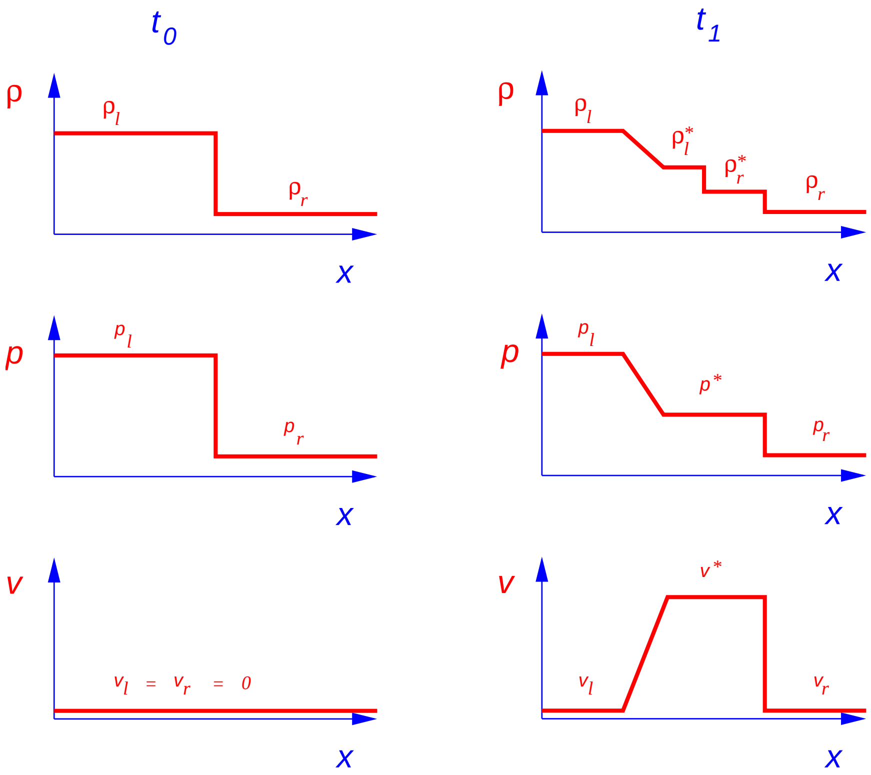

The shock-tube problem

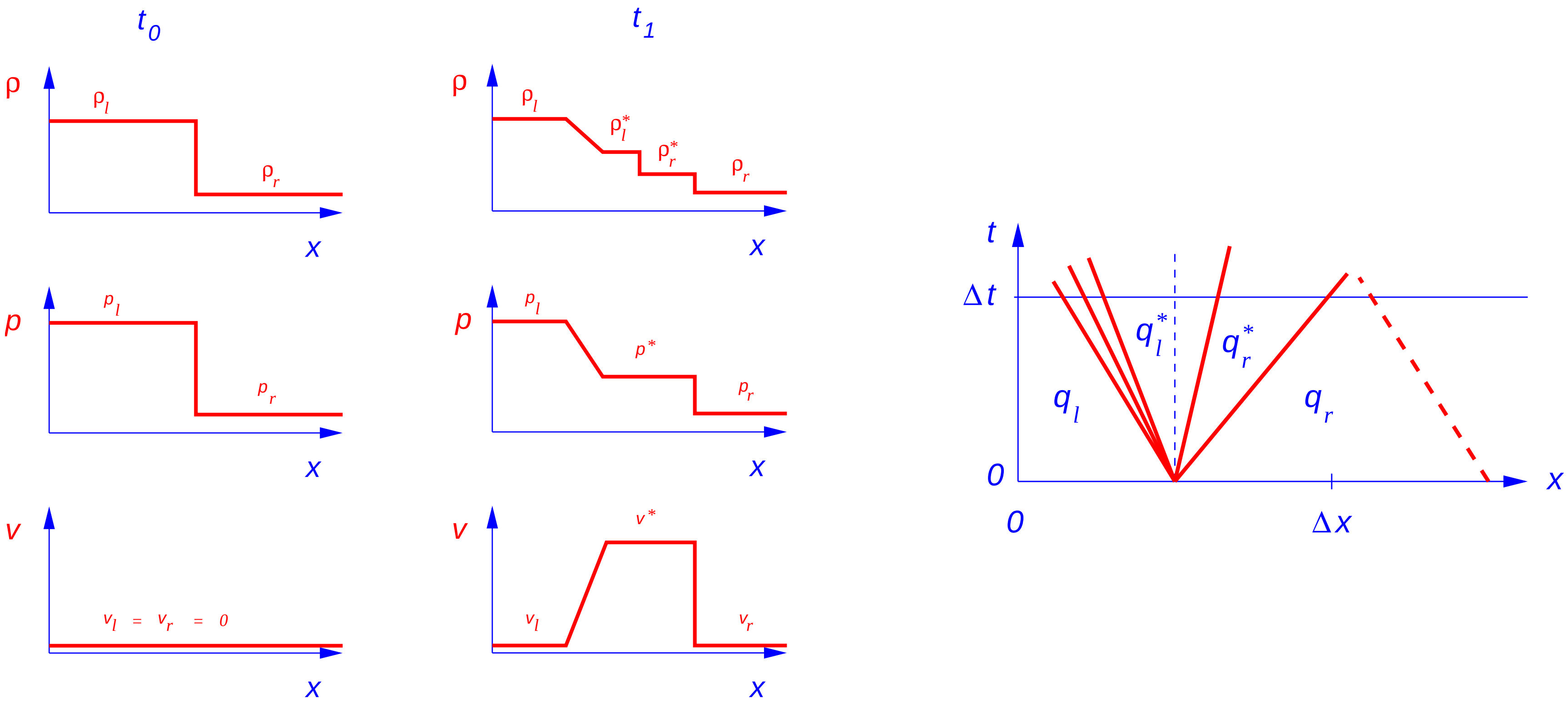

The shock-tube problem

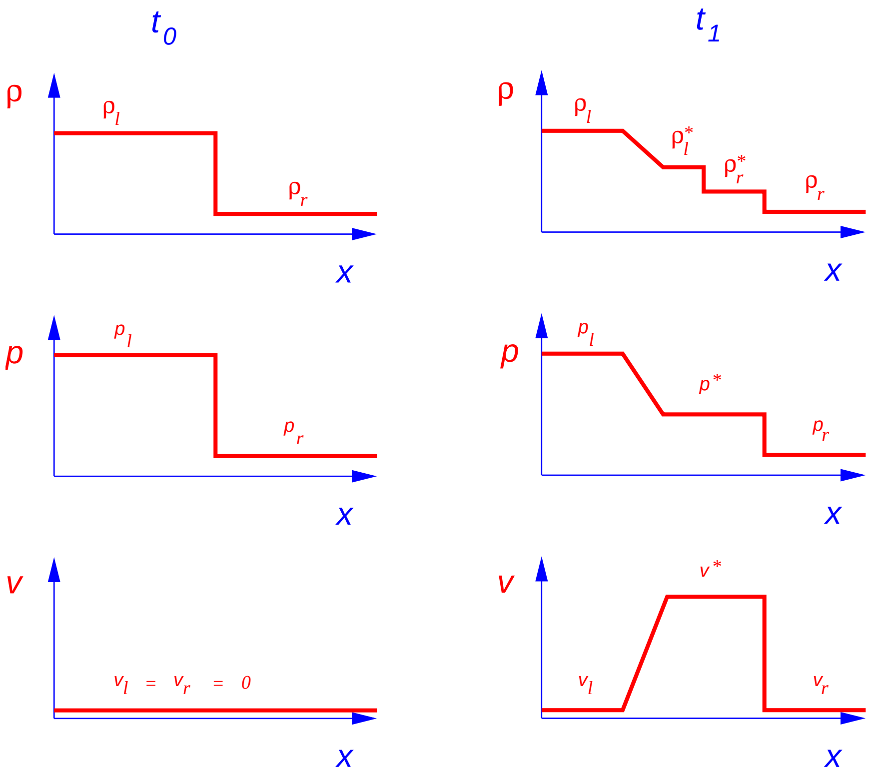

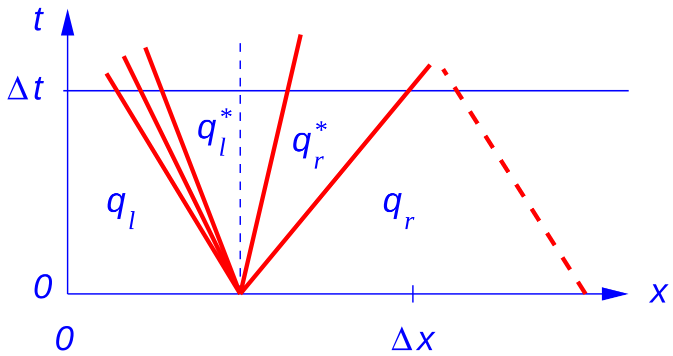

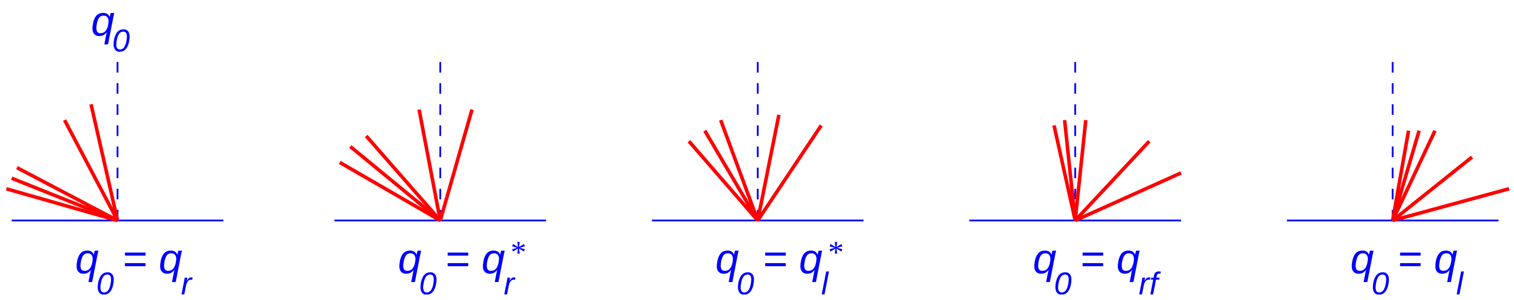

§ 7.1 The Riemann solver of Harten, Lax, and van Leer (HLL)

Consider the system of one-dimensional conservation laws

$$\mathbf{q}_t + \mathbf{f}(\mathbf{q})_x = 0\,, \qquad \mathbf{q}(x,0) = \begin{cases} \mathbf{q}_l & \text{if} \quad x < 0\,, \\ \mathbf{q}_r & \text{if} \quad x > 0\,. \end{cases}$$

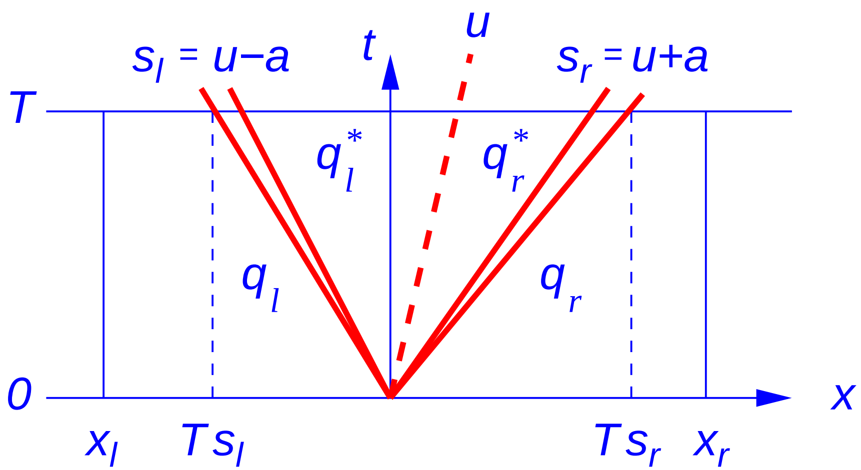

The integral form in the control volume $[x_l, x_r] \times [0, T]$ is given by:

$$\int_{x_l}^{x_r} \mathbf{q}(x,T)\mathrm{d}x = \int_{x_l}^{x_r} \mathbf{q}(x,0)\mathrm{d}x + \int_0^T \mathbf{f}(\mathbf{q}(x_l,t))\mathrm{d}t - \int_0^T \mathbf{f}(\mathbf{q}(x_r,t))\mathrm{d}t$$

The HLL solver (cont.)

$$\begin{aligned}\int_{x_l}^{x_r} \mathbf{q}(x,T)\,\mathrm{d}x &= \int_{x_l}^{x_r} \mathbf{q}(x,0)\,\mathrm{d}x + \int_0^T \mathbf{f}(\mathbf{q}(x_l,t))\,\mathrm{d}t - \int_0^T \mathbf{f}(\mathbf{q}(x_r,t))\,\mathrm{d}t \\ &= x_r\mathbf{q}_r - x_l\mathbf{q}_l + T(\mathbf{f}_l - \mathbf{f}_r)\,, \qquad \mathbf{f}_l = \mathbf{f}(\mathbf{q}_l)\,, \quad \mathbf{f}_r = \mathbf{f}(\mathbf{q}_r)\end{aligned}$$

$$\begin{aligned}\int_{x_l}^{x_r} \mathbf{q}(x,T)\,\mathrm{d}x &= \int_{x_l}^{Ts_l} \mathbf{q}(x,T)\,\mathrm{d}x + \int_{Ts_l}^{Ts_r} \mathbf{q}(x,T)\,\mathrm{d}x + \int_{Ts_r}^{x_r} \mathbf{q}(x,T)\,\mathrm{d}x \\ &= \int_{Ts_l}^{Ts_r} \mathbf{q}(x,T)\,\mathrm{d}x + (Ts_l - x_l)\mathbf{q}_l + (x_r - Ts_r)\mathbf{q}_r\end{aligned}$$

$$\frac{1}{T(s_r - s_l)} \int_{Ts_l}^{Ts_r} \mathbf{q}(x,T)\,\mathrm{d}x := \mathbf{q}^{\mathrm{hll}} = \frac{s_r\mathbf{q}_r - s_l\mathbf{q}_l + \mathbf{f}_l - \mathbf{f}_r}{s_r - s_l}$$

The HLL solver (cont.)

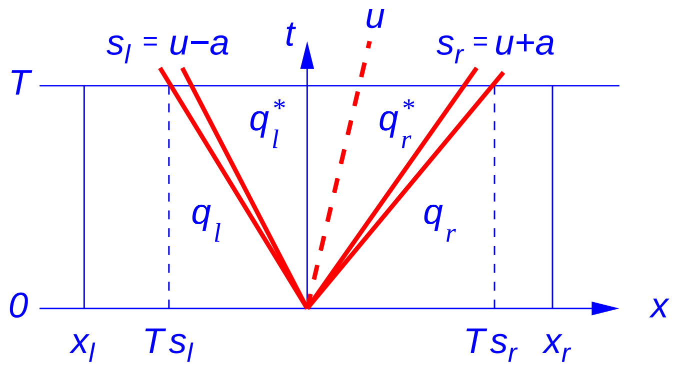

Applying the integral form to the control volume $[x_l, 0] \times [0, T]$ we obtain:

$$\int_{Ts_l}^{0} \mathbf{q}(x,T)\mathrm{d}x = -Ts_l\mathbf{q}_l + T(\mathbf{f}_l - \mathbf{f}_{0l}) \ ,$$

where $\mathbf{f}_{0l}$ is the flux $\mathbf{f}(\mathbf{q})$ along the t-axis. Hence,

$$\mathbf{f}_{0l} = \mathbf{f}_l - s_l\mathbf{q}_l - \frac{1}{T}\int_{Ts_l}^{0} \mathbf{q}(x,T)\mathrm{d}x \ .$$

Doing the same for the control volume $[0, x_r] \times [0, T]$ leads to

$$\mathbf{f}_{0r} = \mathbf{f}_r - s_r\mathbf{q}_r - \frac{1}{T}\int_{0}^{Ts_r} \mathbf{q}(x,T)\mathrm{d}x \ .$$

It follows that

$$\mathbf{f}_{0l} = \mathbf{f}_{0r} \ .$$

Harten, Lax, and van Leer put forward the following approximation:

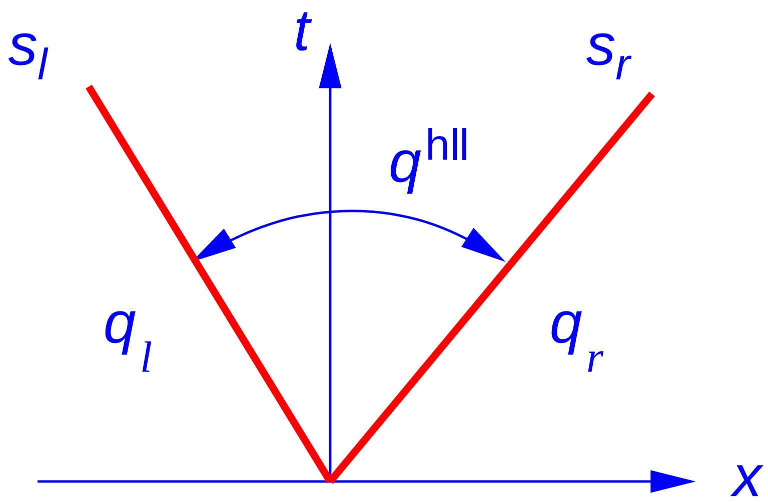

$$\tilde{\mathbf{q}}(x,t) = \begin{cases} \mathbf{q}_l & \text{if} \quad \frac{x}{t} \le s_l \ , \\ \mathbf{q}^{\text{hll}} & \text{if} \quad s_l \le \frac{x}{t} \le s_r \ , \\ \mathbf{q}_r & \text{if} \quad \frac{x}{t} \ge s_r \ . \end{cases}$$

$$\mathbf{f}^{\text{hll}} = \mathbf{f}_l + s_l(\mathbf{q}^{\text{hll}} - \mathbf{q}_l) \quad \text{or}$$

$$\mathbf{f}^{\text{hll}} = \mathbf{f}_r + s_r(\mathbf{q}^{\text{hll}} - \mathbf{q}_r)$$

$$\Rightarrow \quad \mathbf{f}^{\text{hll}} = \frac{s_r\mathbf{f}_l - s_l\mathbf{f}_r + s_l s_r(\mathbf{q}_r - \mathbf{q}_l)}{s_r - s_l}$$

The corresponding intercell flux for the approximate Godunov method is then given by:

$$\mathbf{f}^{\mathrm{hll}}_{i+1/2} = \begin{cases} \mathbf{f}_l & \text{if} \quad 0 \le s_l \ , \\ \dfrac{s_r \mathbf{f}_l - s_l \mathbf{f}_r + s_l s_r (\mathbf{q}_r - \mathbf{q}_l)}{s_r - s_l} & \text{if} \quad s_l \le 0 \le s_r \ , \\ \mathbf{f}_r & \text{if} \quad 0 \ge s_r \end{cases}$$

that can be used in the explicit conservative formula

$$\mathbf{q}_i^{n+1} = \mathbf{q}_i^n + \frac{\Delta t}{\Delta x}\left[\mathbf{f}_{i-1/2} - \mathbf{f}_{i+1/2}\right].$$

§ 7.2 Wave-speed estimates

In order to completely determine the numerical fluxes in the HLL Riemann solver we need estimates for the wave speeds s_l and s_r, and, for the HLLC solver, s^*.

Given a positive speed s^+, a simple choice would consist in

$$s_l = -s^+ , \qquad s_r = s^+ .$$

It is interesting to note that if we set s^+ equal to the maximal speed according to the CFL-condition, i.e.,

$$s^+ = \frac{\Delta x}{\Delta t} ,$$

we obtain *Lax-Friederichs numerical flux*

$$f_{i+1/2} = \frac{1}{2}(f_l - f_r) - \frac{1}{2}\frac{\Delta x}{\Delta t}(q_r - q_l) ,$$

which brings us back to a classical scheme.

Wave-speed estimates (cont.)

More ingenious choices are motivated by a *"Roe average"* of the left and right states, e.g.,

$$s_l = \tilde{u} - \tilde{a}\,, \qquad s_r = \tilde{u} + \tilde{a}\,,$$

where

$$\tilde{u} = \frac{\sqrt{\rho_l}u_l + \sqrt{\rho_r}u_r}{\sqrt{\rho_l} + \sqrt{\rho_r}}\,, \qquad \tilde{a} = \left[(\gamma - 1)(\tilde{H} - \frac{1}{2}\tilde{u}^2)\right]^{\frac{1}{2}}\,,$$

with the enthalpy $H = (E + p)/\rho$ approximated as

$$\tilde{H} = \frac{\sqrt{\rho_l}H_l + \sqrt{\rho_r}H_r}{\sqrt{\rho_l} + \sqrt{\rho_r}}\,.$$

Wave-speed estimates (cont.)

In a different approach we first suppose to have *estimates for p^* and u^** for the pressure and velocity in the Star Region. Then we compute the following wave speeds:

$$s_l = u_l - a_l r_l \,, \qquad s^* = u^* \,, \qquad s_r = u_r + a_r r_r \,,$$

where

$$r_k = \begin{cases} 1 & \text{if} \quad p^* \leq p_k \quad \text{rarefaction head} \\ \left[1 + \frac{\gamma+1}{2\gamma} \left(\frac{p^*}{p_k} - 1 \right) \right]^{\frac{1}{2}} & \text{if} \quad p^* > p_k \quad \text{shock} \end{cases}$$

p^* and u^* can be found from a linearization of the Riemann problem yielding

$$p^* = \frac{1}{2}(p_l + p_r) - \frac{1}{2}(u_r - u_l)\bar{\rho}\bar{a} \,, \qquad u^* = \frac{1}{2}(u_l + u_r) - \frac{1}{2}\frac{(p_r - p_l)}{\bar{\rho}\bar{a}} \,,$$

where

$$\bar{\rho} = \frac{1}{2}(\rho_l + \rho_r) \,, \quad \bar{a} = \frac{1}{2}(a_l + a_r) \,.$$

§ 7.3 The Riemann solver of Roe

Consider again the Riemann problem

$$\begin{aligned} \mathbf{q}_t + \mathbf{f}(\mathbf{q})_x &= 0\,, \\ \mathbf{q}(x,0) &= \begin{cases} \mathbf{q}_l & \text{if} \quad x < 0\,, \\ \mathbf{q}_r & \text{if} \quad x > 0\,, \end{cases} \end{aligned}$$

where for the x-split three-dimensional Euler equation

$$\mathbf{q} = \begin{pmatrix} \rho \\ \rho u \\ \rho v \\ \rho w \\ E \end{pmatrix}, \qquad \mathbf{f}(\mathbf{q}) = \begin{pmatrix} \rho u \\ \rho u^2 + p \\ \rho u v \\ \rho u w \\ u(E+p) \end{pmatrix}.$$

The Roe solver (cont.)

Using the chain rule, the conservation law

$$\mathbf{q}_t + \mathbf{f}(\mathbf{q})_x = 0$$

may be written as

$$\mathbf{q}_t + \mathbf{A}(\mathbf{q})\mathbf{q}_x = 0\,, \qquad \mathbf{A}(\mathbf{q}) = \frac{\partial \mathbf{f}}{\partial \mathbf{q}}\,.$$

Roe's approach consists in replacing the Jacobian matrix $\mathbf{A}(\mathbf{q})$ by a *constant Jacobian*

$$\tilde{\mathbf{A}} = \tilde{\mathbf{A}}(\mathbf{q}_l, \mathbf{q}_r)$$

resulting in the Riemann problem for the *linear system*

$$\begin{aligned} \mathbf{q}_t + \tilde{\mathbf{A}}\mathbf{q}_x &= 0\,, \\ \mathbf{q}(x,0) &= \begin{cases} \mathbf{q}_l & \text{if} \quad x < 0\,, \\ \mathbf{q}_r & \text{if} \quad x > 0\,, \end{cases} \end{aligned}$$

which can be solved exactly.

The Roe solver (cont.)

Once the matrix $\tilde{\mathbf{A}}(\mathbf{q}_l, \mathbf{q}_r)$, its eigenvalues $\tilde{\lambda}_i(\mathbf{q}_l, \mathbf{q}_r)$, and corresponding right eigenvectors $\tilde{\mathbf{k}}^{(i)}(\mathbf{q}_l, \mathbf{q}_r)$ are available, the difference between right and left state can be expanded in terms of the eigenvectors:

$$\Delta\mathbf{q} = \mathbf{q}_r - \mathbf{q}_l = \sum_{i=1}^{m} \tilde{\alpha}_i \tilde{\mathbf{k}}^{(i)} \, ,$$

from which one finds the wave strengths $\tilde{\alpha}_i(\mathbf{q}_l, \mathbf{q}_r)$.

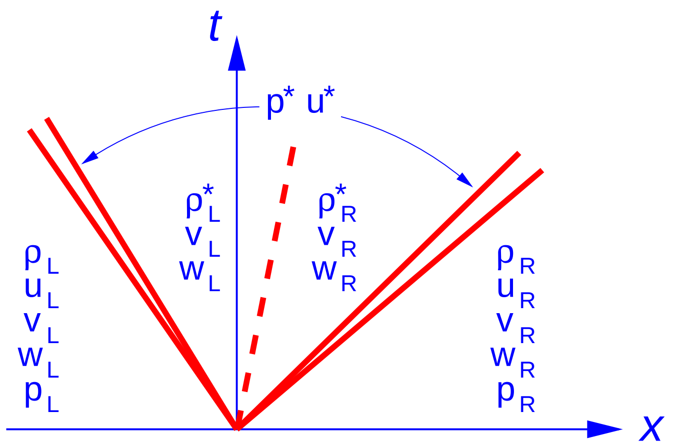

$$\begin{aligned}
\mathbf{q}_{i+1/2}(0) &= \mathbf{q}_l + \sum_{\tilde{\lambda}_i \le 0} \tilde{\alpha}_i \tilde{\mathbf{k}}^{(i)} \, , \quad \text{or} \\
\mathbf{q}_{i+1/2}(0) &= \mathbf{q}_r - \sum_{\tilde{\lambda}_i \ge 0} \tilde{\alpha}_i \tilde{\mathbf{k}}^{(i)} \, , \\
\mathbf{f}_{i+1/2} &= \mathbf{f}_l + \sum_{\tilde{\lambda}_i \le 0} \tilde{\alpha}_i \tilde{\lambda}_i \tilde{\mathbf{k}}^{(i)} \, , \quad \text{or} \\
\mathbf{f}_{i+1/2} &= \mathbf{f}_r - \sum_{\tilde{\lambda}_i \ge 0} \tilde{\alpha}_i \tilde{\lambda}_i \tilde{\mathbf{k}}^{(i)} \, .
\end{aligned}$$

The x-direction Jacobian matrix for the Euler equations, $\mathbf{A}(\mathbf{q})$, is

$$\mathbf{A} = \begin{bmatrix} 0 & 1 & 0 & 0 & 0 \\ \hat{\gamma}H - u^2 - a^2 & (3-\gamma)u & -\hat{\gamma}v & -\hat{\gamma}w & \hat{\gamma} \\ -uv & v & u & 0 & 0 \\ -uw & w & 0 & u & 0 \\ \frac{1}{2}u[(\gamma-3)H - a^2] & H - \hat{\gamma}u^2 & -\hat{\gamma}uv & -\hat{\gamma}uw & \gamma u \end{bmatrix},$$

where $\hat{\gamma} = \gamma - 1$ and $a = \sqrt{\gamma p/\rho}$. The eigenvalues are

$$\lambda_1 = u - a\,, \quad \lambda_2 = \lambda_3 = \lambda_4 = u\,, \quad \lambda_5 = u + a\,.$$

The corresponding right eigenvalues are

$$\mathbf{k}^{(1)} = \begin{bmatrix} 1 \\ u-a \\ v \\ w \\ H-ua \end{bmatrix}, \qquad \mathbf{k}^{(2)} = \begin{bmatrix} 1 \\ u \\ v \\ w \\ \frac{1}{2}V^2 \end{bmatrix}, \qquad \mathbf{k}^{(3)} = \begin{bmatrix} 0 \\ 0 \\ 1 \\ 0 \\ v \end{bmatrix},$$

$$\mathbf{k}^{(4)} = \begin{bmatrix} 0 \\ 0 \\ 0 \\ 1 \\ w \end{bmatrix}, \qquad \mathbf{k}^{(5)} = \begin{bmatrix} 1 \\ u+a \\ v \\ w \\ H+ua \end{bmatrix},$$

where $H = \dfrac{E+p}{\rho}\,, \qquad E = \dfrac{1}{2}\rho V^2 + \rho e\,, \qquad V^2 = u^2 + v^2 + w^2\,.$

The Roe solver (cont.)

Roe requires the constant Jacobian matrix $\tilde{\mathbf{A}} = \tilde{\mathbf{A}}(\mathbf{q}_l, \mathbf{q}_r)$ to satisfy the algebraic properties of the Jacobian $\mathbf{A}(\mathbf{q})$, i.e.,

$$\tilde{\lambda}_i = \tilde{\lambda}_i(\mathbf{q}_l, \mathbf{q}_r) \in \mathbb{R} \quad \forall i \,,$$

$$\tilde{\mathbf{A}}(\mathbf{q}, \mathbf{q}) = \mathbf{A}(\mathbf{q}) \,,$$

$$\mathbf{f}(\mathbf{q}_r) - \mathbf{f}(\mathbf{q}_l) = \tilde{\mathbf{A}}(\mathbf{q}_r - \mathbf{q}_l) \,.$$

These conditions may be fullfilled with the following “Roe averagged” quantities to be used in the formulae for λ_i and $\mathbf{k}^{(i)}$ shown on the brevious pages:

$$\begin{aligned} \tilde{u} &= \frac{\sqrt{\rho_l}u_l + \sqrt{\rho_r}u_r}{\sqrt{\rho_l} + \sqrt{\rho_r}} \,, \\ \tilde{v} &= \frac{\sqrt{\rho_l}v_l + \sqrt{\rho_r}v_r}{\sqrt{\rho_l} + \sqrt{\rho_r}} \,, \\ \tilde{w} &= \frac{\sqrt{\rho_l}w_l + \sqrt{\rho_r}w_r}{\sqrt{\rho_l} + \sqrt{\rho_r}} \,, \end{aligned}$$

$$\begin{aligned} \tilde{H} &= \frac{\sqrt{\rho_l}H_l + \sqrt{\rho_r}H_r}{\sqrt{\rho_l} + \sqrt{\rho_r}} \,, \\ \tilde{a} &= (\gamma - 1)[\tilde{H} - \frac{1}{2}\tilde{V}^2]^{\frac{1}{2}} \,, \\ \tilde{V}^2 &= \tilde{u}^2 + \tilde{v}^2 + \tilde{w}^2 \,. \end{aligned}$$

§ 8 Higher order accurate methods

Piece-wise linear, local reconstruction (variable extrapolation method) as part of the *MUSCL scheme* (Monotone Upstream-centred Scheme for Conservation Laws)

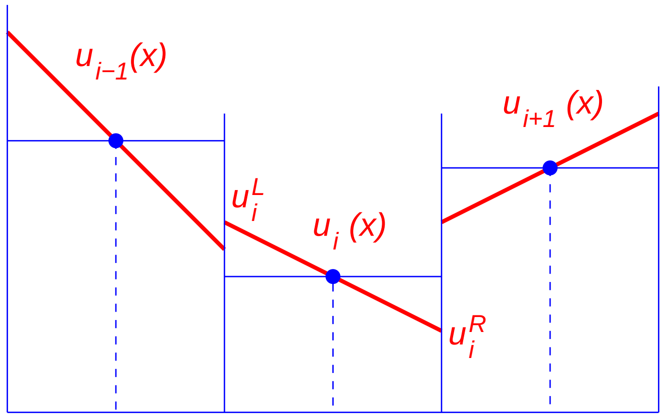

$$
\begin{aligned}
\mathbf{q}_i(x) &= \mathbf{q}_i^n + \frac{x - x_i}{\Delta x}\boldsymbol{\Delta}_i \quad x \in [0, \Delta x]\,, \\
\mathbf{q}_i^L &= \mathbf{q}_i^n - \frac{1}{2}\boldsymbol{\Delta}_i\,, \\
\mathbf{q}_i^R &= \mathbf{q}_i^n + \frac{1}{2}\boldsymbol{\Delta}_i\,,
\end{aligned}
$$

leads to the *Generalized Riemann Problem*

$$
\begin{aligned}
\mathbf{q}_t + \mathbf{f}(\mathbf{q})_x &= 0\,, \\
\mathbf{q}(x,0) &= \begin{cases} \mathbf{q}_i(x) & \text{if} \quad x < 0\,, \\ \mathbf{q}_{i+1}(x) & \text{if} \quad x > 0\,. \end{cases}
\end{aligned}
$$

TVD methods (cont.)

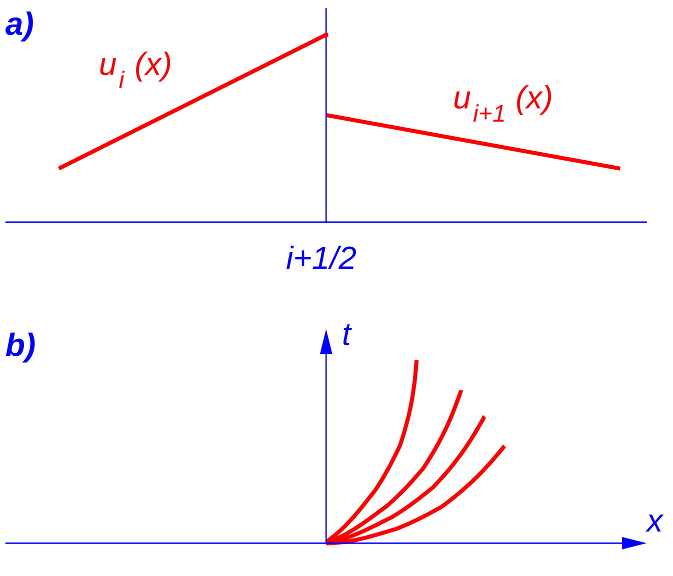

Initial data (a) and solution structure (b) of the generalized Riemann problem.

In the MUSCL-Hancock method intermediate boundary extrapolated values $\tilde{\mathbf{q}}_i^R$ and $\tilde{\mathbf{q}}_{i+1}^L$ are obtained by

$$\begin{aligned} \bar{\mathbf{q}}_i^L &= \mathbf{q}_i^L + \frac{1}{2}\frac{\Delta t}{\Delta x}\left[\mathbf{f}(\mathbf{q}_i^L) - \mathbf{f}(\mathbf{q}_i^R)\right], \\ \bar{\mathbf{q}}_i^R &= \mathbf{q}_i^R + \frac{1}{2}\frac{\Delta t}{\Delta x}\left[\mathbf{f}(\mathbf{q}_i^L) - \mathbf{f}(\mathbf{q}_i^R)\right], \end{aligned}$$

which then form the piece-wise constant data for the conventional Riemann problem

$$\begin{aligned} \mathbf{q}_t + \mathbf{f}(\mathbf{q})_x &= 0\,, \\ \mathbf{q}(x,0) &= \begin{cases} \bar{\mathbf{q}}_i^R & \text{if} \quad x < 0\,, \\ \bar{\mathbf{q}}_{i+1}^L & \text{if} \quad x > 0\,. \end{cases} \end{aligned}$$

An important property of the general scalar conservation law

$$u_t + f(u)_x = 0 \tag{5}$$

is *monotonicity*:

If two initial data functions $v_0(x)$ and $u_0(x)$ for Eq. (5) satisfy $v_0(x) \geq u_0(x)\ \forall x$, then the corresponding solutions $v(x,t)$ and $u(x,t)$ satisfy $v(x,t) \geq u(x,t)\ t > 0$.

Correspondingly, a *monotone scheme* has the following property:

$$\text{if} \quad v_i^n \geq u_i^n \quad \forall i \quad \text{then} \quad v_i^{n+1} \geq u_i^{n+1} \quad \forall i\,.$$

The *Theorem of Godunov* states that: *There are no monotone, linear schemes for the solution of Eq. (5) of second or higher order of accuracy*.

(A linear scheme has generally the form

$$q_i^{n+1} = \sum_{k=-k_L}^{k_R} b_k q_{i+k}^n\,, \quad k_L\,, k_R \in \mathbb{N}^+)$$

In order to circumvent Godunov's theorem, higher order *non-linear* schemes were invented. One way of doing so consists in finding a *slope limiter* ξ_i such that

$$\bar{\mathbf{\Delta}}_i = \boldsymbol{\xi_i} \mathbf{\Delta}_i \,,$$

$$\mathbf{\Delta}_i = \frac{1}{2}(1+\omega)(\mathbf{q}_i^n - \mathbf{q}_{i-1}^n) + \frac{1}{2}(1+\omega)(\mathbf{q}_{i+1}^n - \mathbf{q}_i^n)\,, \quad \omega \in [-1, 1]\,.$$

$\boldsymbol{\xi_i}$ depends in a non-linear way on the ratio $\boldsymbol{r}$, where

$$\boldsymbol{r} = \frac{\mathbf{q}_i^n - \mathbf{q}_{i-1}^n}{\mathbf{q}_{i+1}^n - \mathbf{q}_i^n}$$

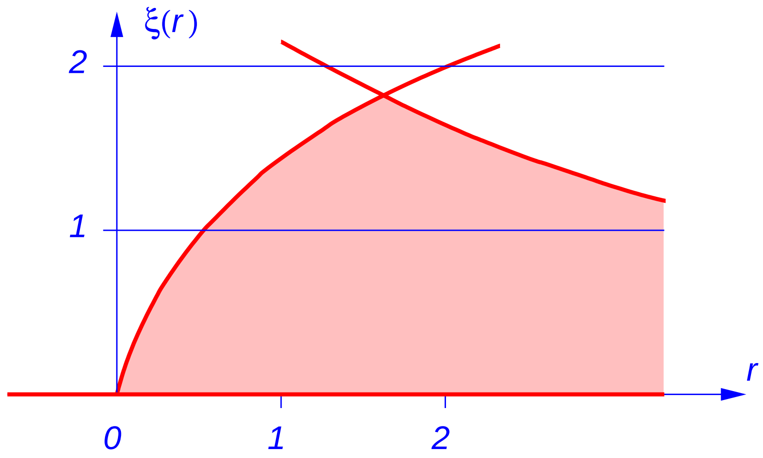

TVD region for slope limiters. For negative $\boldsymbol{r}$ the TVD region is the single line $\boldsymbol{\xi} = \mathbf{0}$, for positive $\boldsymbol{r}$ the TVD region corresponds to the pink region. SUPERBEE, van Leer, MINMOD, etc type of slope limiters are a subset of this region.

§ 9 The positivity problem with HLL when applied to MHD

The HLL-scheme is a positive scheme when applied to the system of the Euler equations. This means that density and pressure remain positive under all circumstances.

It remains positive when applied to the system of one-dimensional MHD equations as long as the longitudinal magnetic field component is continuous, i.e., constant. The transversal components may have discontinuities.

The HLL-middle state can become non-positive if there is a jump in the normal component of the magnetic field across the cell interface.

In planar MHD the solenoidality condition reduces to

$$\frac{\partial B_x}{\partial x} = 0\,,$$

since B_y and B_z are constant in the transversal directions y and z. Hence, $B_x(x) =$ const. However, in multiple dimensions, this need not be the case any more.

However, many multidimensional codes work with *dimensional operator splitting*, where numerical updates are computed separately for each dimensional direction. Each “directional sweep” is treated as a purely one-dimensional problem.

The *problem* with directional splitting in multi-dimensional MHD is that the one-dimensional sweeps “see” at cell boundaries discontinuities in the longitudinal component of the magnetic field.

Remedy proposed by Janhunen (2000): Discontinuities in the normal component of the magnetic field in planar MHD lead to the violation of the solenoidality condition, hence, they signify *magnetic monopoles*. Since we cannot avoid theses discontinuities we modify the MHD equations in a way that they include magnetic monopoles.

The MHD-equations can be derived without using the condition $\nabla \cdot \mathbf{B} = 0$ at first. Powell (1994) derived the following set of equations:

$$
\begin{aligned}
\frac{\partial \rho}{\partial t} + \nabla \cdot (\rho \mathbf{v}) &= 0 \\
\frac{\partial (\rho \mathbf{v})}{\partial t} + \nabla \cdot \left[\rho \mathbf{v}\mathbf{v} + (p + \frac{B^2}{2\mu_0})\mathbb{I} - \frac{1}{\mu_0}\mathbf{B}\mathbf{B} \right] &= -\mathbf{B}(\nabla \cdot \mathbf{B}) \\
\frac{\partial \mathbf{B}}{\partial t} + \nabla \cdot (\mathbf{v}\mathbf{B} - \mathbf{B}\mathbf{v}) &= -\mathbf{v}(\nabla \cdot \mathbf{B}) \\
\frac{\partial E}{\partial t} + \nabla \cdot \left[(E + p + \frac{B^2}{2\mu_0})\mathbf{v} - \frac{1}{\mu_0}(\mathbf{v} \cdot \mathbf{B})\mathbf{B} \right] &= -(\mathbf{v} \cdot \mathbf{B})(\nabla \cdot \mathbf{B})
\end{aligned}
$$

Powell used this system in order to avoid the accumulation of numerical discretization errors in $\nabla \cdot \mathbf{B}$.

Janhunen argues that Powell's monopols were ghost particles with no interaction with the electromagnetic field. The "correct way" to derive monopole MHD would include a force on magnetic monopoles in a similar way as electric charges experience a force in a electric field. He uses a generalization of the Lorentz force and so obtains:

$$
\begin{aligned}
\frac{\partial \rho}{\partial t} + \nabla \cdot (\rho \mathbf{v}) &= 0 \\
\frac{\partial (\rho \mathbf{v})}{\partial t} + \nabla \cdot \left[\rho \mathbf{v}\mathbf{v} + (p + \frac{B^2}{2\mu_0})\mathbb{I} - \frac{1}{\mu_0}\mathbf{B}\mathbf{B} \right] &= 0 \\
\frac{\partial \mathbf{B}}{\partial t} + \nabla \cdot (\mathbf{v}\mathbf{B} - \mathbf{B}\mathbf{v}) &= -\mathbf{v}(\nabla \cdot \mathbf{B}) \\
\frac{\partial E}{\partial t} + \nabla \cdot \left[(E + p + \frac{B^2}{2\mu_0})\mathbf{v} - \frac{1}{\mu_0}(\mathbf{v} \cdot \mathbf{B})\mathbf{B} \right] &= 0
\end{aligned}
$$

The linearized system has an eigenstructure similar to Powell's equations.

Janhunen correspondingly includes a source term in the HLL-solver for the induction equation:

$$
\begin{aligned}
s_B^{\mathrm{hll}} &= \int_0^T \frac{1}{L} \int_{s_l T}^{s_r T} s(x,t)\,\mathrm{d}x\,\mathrm{d}t \\
&\approx \int_0^T \frac{1}{L} \int_{s_l T}^{s_r T} (-v^{\mathrm{hll}}\,\frac{\partial B_x}{\partial x})\,\mathrm{d}x\,\mathrm{d}t \\
&= \int_0^T \frac{1}{L} \int_{s_l t}^{s_r t} (-v^{\mathrm{hll}}\,\frac{\partial B_x}{\partial x})\,\mathrm{d}x\,\mathrm{d}t \\
&= \frac{1}{s_r - s_l} \int_0^T (-v^{\mathrm{hll}})\Delta B_x \frac{\mathrm{d}t}{T} \\
&= -\frac{v^{\mathrm{hll}}\Delta B_x}{s_r - s_l}
\end{aligned}
$$

where $L = (s_r - s_l)T$ and $\Delta B_x = B_{x\,r} - B_{x\,l}$. The only approximation involved is $v \approx v^{\mathrm{hll}}$.

Notice, that the *"Janhunen trick"* is used only for computing cell centered magnetic field components, which in turn are *only used for computing numerical fluxes*. The magnetic field proper of the solution is defined at cell boundaries and updated with a constrained transport (CT) scheme, which strictly maintains $\nabla \cdot \mathbf{B}$.

The positivity problem with HLL when applied to MHD (cont.)

Even when using the Janhunen source term we have encountered instances of *negative pressure* when $\beta_{\rm plasma} \ll 1$. In these cases the total energy is completely dominated by the magnetic energy, so that the internal energy may become negative when computing it by subtraction of the magnetic from the total energy.

We therefore use a *hybrid scheme* in the MHD-module of the CO^{5}BOLD code. In regions with $\beta_{\rm plasma} \ll 1$ we use the equation for internal energy instead of the total energy equation. We thereby *violate strict energy conservation*. In all other regions the total energy equation is used. The switch from total to internal energy equation can be specified as a parameter. A typical value would be $\beta_{\rm switch} = 10^{-3}$.

References

Janhunen, P.: 2000, JCP 160, 649–661

Laney, C.B.: 1998, Computational Gasdynamics, Cambridge University Press, Cambridge

LeVeque, R.J.: 2002, Finite Volume Methods for Hyperbolic Problems, Cambridge University Press, Cambridge

LeVeque, R.J.: 1992, Numerical Methods for Conservation Laws, Birkhäuser Verlag, Basel

LeVeque, R.J., Mihalas, D., Dorfi, E.A., and Müller, E.: 1998, Computational Methods for Astrophysical Fluid Flow, O. Steiner & A. Gautschy (eds.), Springer-Verlag, Berlin

Powell, K.G.: 1994, ICASE Report 94-24

Toro, E.F.: 1999, Riemann Solvers and Numerical Methods for Fluid Dynamics, Springer-Verlag, Berlin

Part III: Concrete implementations

§ 10 Computer Codes

In the following is a non-exhaustive, arbitrarily selected list of codes that may or may not be suitable for serving your needs. Details are without guarantee.

acronym	VAC		
name	Versatile Advection Code	PENCIL	NIRWANA
web page	http://www.phys.uu.nl/˜toth/	http://www.nordita.org/software/pencil-code/	http://nirvana-code.aip.de/
principal author	Gábor Tóth	Wolfgang Dobler	Udo Ziegler
language	dimension independent notation, (convertible to FORTRAN via VAC Preprocessor)	FORTRAN	C
MHD	yes	yes	yes
radiative transfer	no	yes	no
parallelization	HPF, MPI, OpenMP	MPI	MPI
grid	structured grid; adaptive/AMR	Cartesian; adaptive/static	Cartesina, cylidrical, spherical; adaptive/AMR
comments:	The code features a variety of numerical methods for the advection step including TVD schemes and Riemann solvers. There is a version with automatic adaptive mesh refinement, AMR.	Code uses a higher order fnite-difference scheme. Primarily designed to deal with weakly compressible turbulent flows.	Godunov-type central scheme, piecewise linear TVD reconstruction, flux-CT scheme, dual energy formalism

Computer Codes (cont.)

acronym	CO^{5}BOLD	MURaM	ANTARES
name	Conservative Code for the Computation of Compressible Convection in a Box of L Dimensions	MPS/University of Chicago Radiative MHD	A Numerical Tool for Astrophysical REsearch
web page	http://www.astro.uu.se/~bf/co5bold_main.html	http://www.mps.mpg.de/projects/solar-mhd/muram_site/code.html	http://arxiv.org/abs/0905.0177
principal author	Bernd Freytag	Alexander Vögler	H.J. Muthsam
language	FORTRAN	?	FORTRAN
MHD	yes	yes	yes
radiative transfer	yes/non-grey	yes/non-grey	yes/non-grey
parallelization	OpenMP	MPI	MPI; OpenMP
grid	Cartesian; adaptive/static	Cartesian; adaptive/static	Cartesian, spherical; AMR/static
comments:	Riemann solver based code; realistic EOS and opacities; chemical reaction network; dynamic hydrogen ionization	Fourth-order accurate, explicit finite differences TVD scheme; realistic EOS and opacities	Features various high-resolution schemes

acronym	CLAWPACK		
name	Conservation Law Package	A-MAZE	ZEUS-MP/2
web page	http://www.amath.washington.edu/ claw/	http://www.astro.phys.ethz.ch/staff/folini/private/research/a_maze/a_maze.html	http://lca.ucsd.edu/portal/codes/zeusmp2
principal author	Randall J. LeVeque	Rolf Walder	Stone & Norman
language	FORTRAN	FORTRAN	FORTRAN
MHD	yes	yes	yes
radiative transfer	no	yes	no
parallelization	MPI	MPI	MPI
grid	adaptive/AMR	Cartesian; adaptive/AMR	Cartesian, spherical; cylindricalAMR/static
comments:	Features various solvers incl. Riemann solvers; solves problems on curved manifolds	Riemann solver based scheme; NLTE radiative transfer for moving media	

Computer Codes (cont.)

acronym	
name	FLASH
web page	http://flash.uchicago.edu/website/home/
principal author	Alliances Center for Astrophysical Thermonuclear Flashes
language	FORTRAN
MHD	yes
radiative transfer	no
parallelization	MPI
grid	Cartesian, spherical, cylindrical polar; AMR
comments:	HD: split PPM, unsplit MUSCL-Hancock; MHD: split 8-wave solver, unsplit staggered mesh; split relativistic hydro solver; reactive gas dynamics

Computer Codes (cont.): example CO^{5}BOLD code

CO^{5}BOLD stands for COnservative COde for the COmputation of COmpressible COnvection in a BOx of L Dimensions with L=2,3.

CO^{5}BOLD is designed for simulating *hydrodynamics* and *radiative transfer* in the outer and inner layers of stars. Additionally, it can treat *magnetohydrodynamics*, non-equilibrium *chemical reaction networks*, dynamic *hydrogen ionization*, and *dust formation* in stellar atmospheres.

Application examples of CO^{5}BOLD (Courtesy Sven Wedemeyer-Böhm)

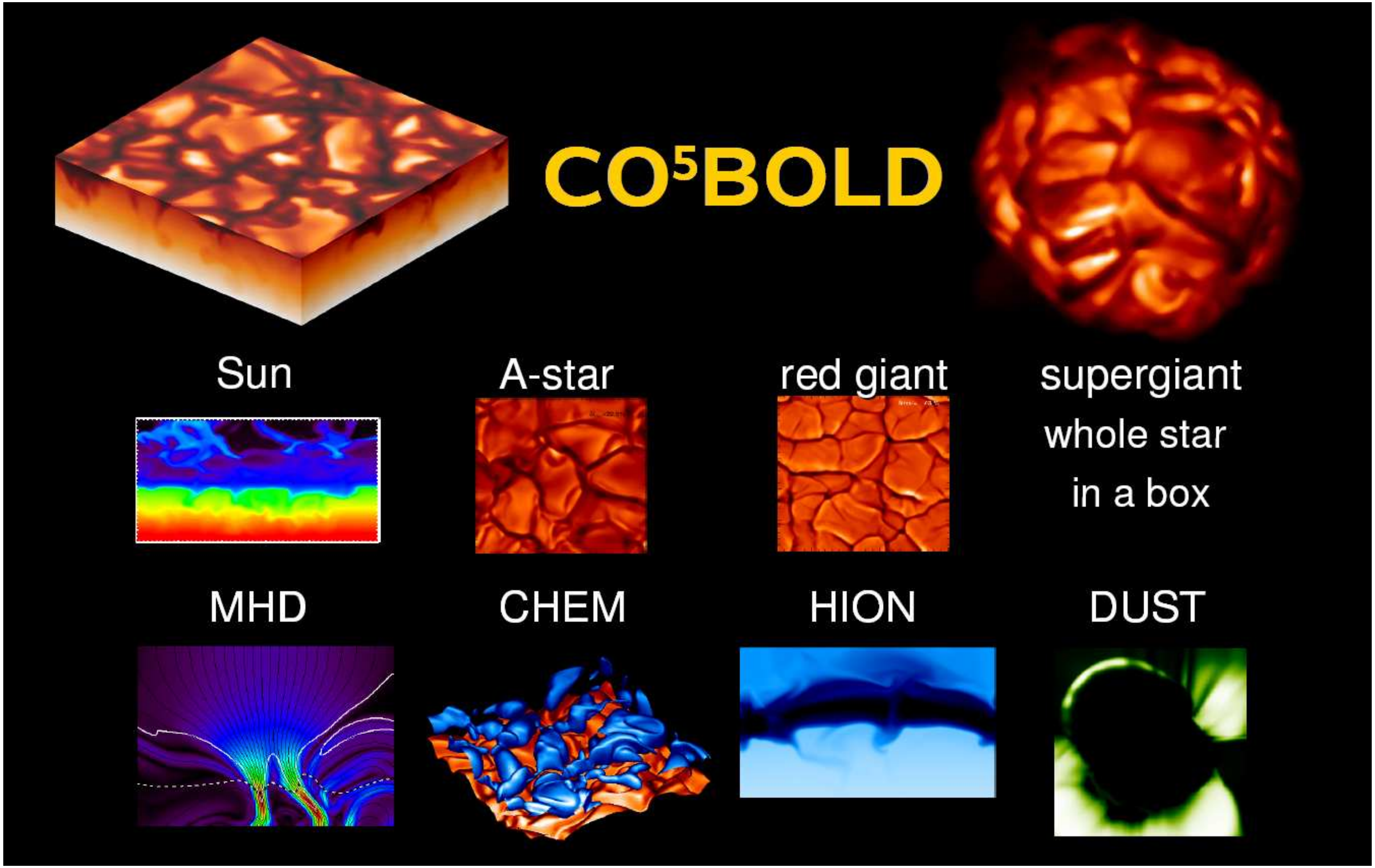

Computer Codes (cont.): example CO^{5}BOLD code

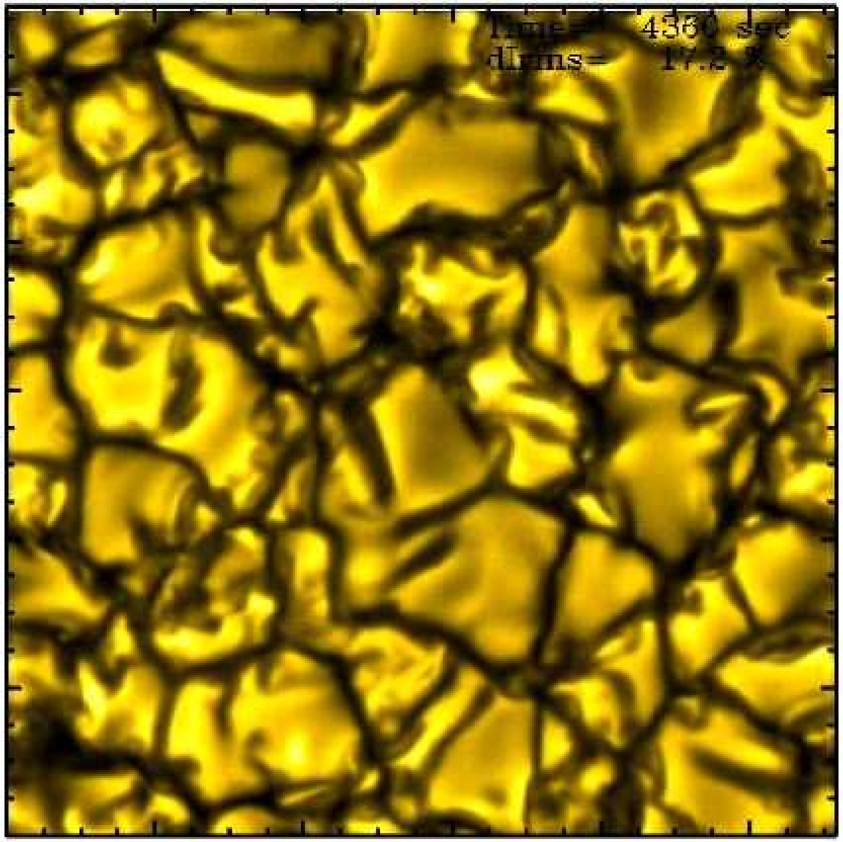

Simulation of solar granulation with CO^{5}BOLD. $400 \times 400 \times 165$ grid cells, 11.2×11.2 Mm, Mean contrast at $\lambda \approx 620$ nm is 16.65%.

Courtesy *M. Steffen, AIP*

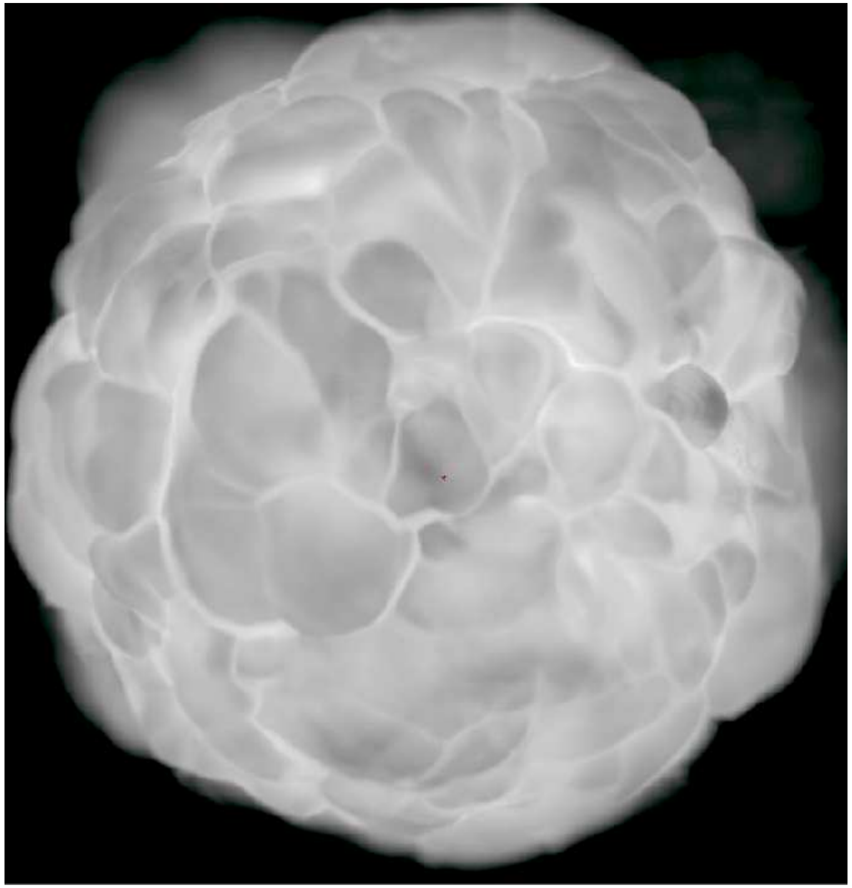

Simulation of a red supergiant with CO^{5}BOLD. 235^3 grid cells, $m_{\rm star} = 12 m_\odot$, $T_{\rm eff} = 3436$ K, $R_{\rm star} = 875 R_\odot$

Courtesy *Bernd Freytag*

Computer Codes (cont.): example CO^5BOLD code

Two-dimensional radiation-hydrodynamic simulation of surface convection including the chromospheric layer. The dimensions of the computational domain are: Width, 5600 km; Height above the surface of $\tau = 1$, 1700 km; Depth below this surface level: 1400 km.

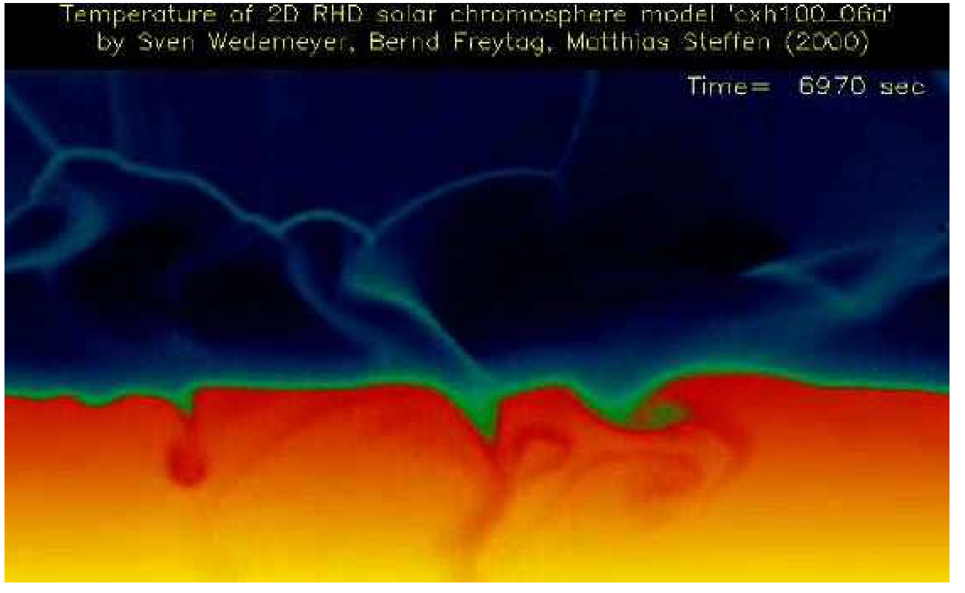

S. Wedemeyer et al. 2004, A&A 414, 1121

Computer Codes (cont.): example CO^{5}BOLD code

CO^{5}BOLD works with

- Cartesian (non-equidistant) grids,
- realistic equation of state,
- non-local, multidimensional radiation transport,
- realistic opacities, opacity binning
- various boundary conditions

CO^{5}BOLD is programmed with

- FORTRAN 90,
- OpenMP directives,

The manual for CO^{5}BOLD can be found under

`http://www.astro.uu.se/~bf/co5bold_main.html`

Just type CO5BOLD in Google.

§ 11 Equations and boundary conditions

The three-dimensional computational domain encompasses the integral layers from the upper convection zone to the middle chromosphere.

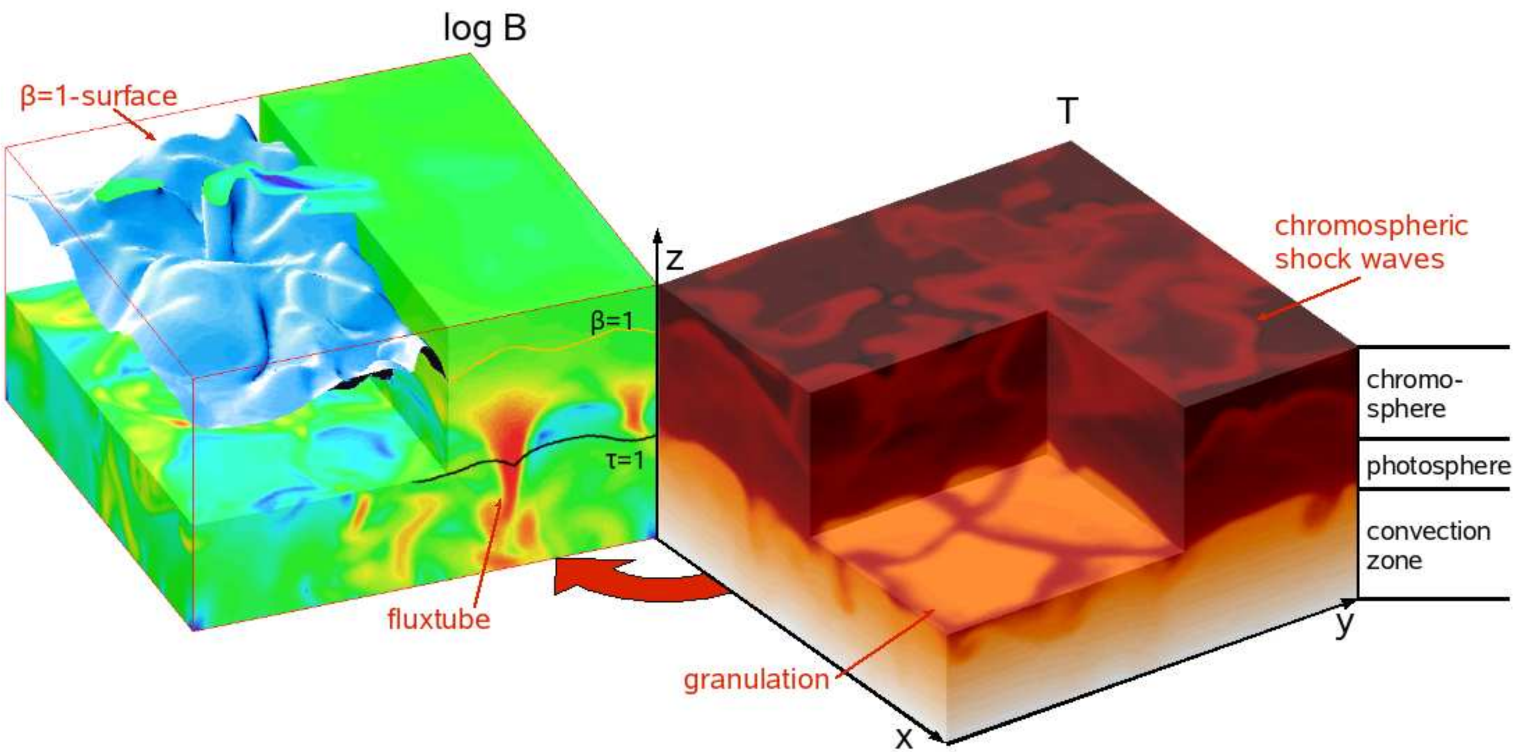

With 120^3 grid cells, the spatial resolution in the horizontal direction is 40 km, while in the vertical direction it is 20 km throughout the photosphere and chromosphere increasing to 50 km through the convection-zone layer.

Equations and boundary conditions (cont.)

The ideal MHD-equations can be written in conservative form as:

$$\frac{\partial \boldsymbol{U}}{\partial t} + \boldsymbol{\nabla} \cdot \boldsymbol{\mathcal{F}} = \boldsymbol{S} \, ,$$

where the vector of conserved variables $\boldsymbol{U}$, the source term $\boldsymbol{S}$ due to gravity and radiation, and the flux tensor $\boldsymbol{\mathcal{F}}$ are

$$\boldsymbol{U} = (\rho, \rho\boldsymbol{v}, \boldsymbol{B}, E) \; , \qquad \boldsymbol{S} = (0, \rho\boldsymbol{g}, 0, \rho\boldsymbol{g}\cdot\boldsymbol{v} + q_{\mathrm{rad}}) \; ,$$

$$\boldsymbol{\mathcal{F}} = \begin{pmatrix} \rho\boldsymbol{v} \\ \rho\boldsymbol{v}\boldsymbol{v} + \left(p + \frac{\boldsymbol{B}\cdot\boldsymbol{B}}{8\pi}\right)\boldsymbol{I} - \frac{\boldsymbol{B}\boldsymbol{B}}{4\pi} \\ \boldsymbol{v}\boldsymbol{B} - \boldsymbol{B}\boldsymbol{v} \\ \left(E + p + \frac{\boldsymbol{B}\cdot\boldsymbol{B}}{8\pi}\right)\boldsymbol{v} - \frac{1}{4\pi}\left(\boldsymbol{v}\cdot\boldsymbol{B}\right)\boldsymbol{B} \end{pmatrix} .$$

The tensor product of two vectors $\boldsymbol{a}$ and $\boldsymbol{b}$ is the tensor $\boldsymbol{a}\boldsymbol{b} = \boldsymbol{C}$ with elements $c_{mn} = a_m b_n$.

Equations and boundary conditions (cont.)

The total energy E is given by

$$E = \rho\epsilon + \rho\frac{\boldsymbol{v}\cdot\boldsymbol{v}}{2} + \frac{\boldsymbol{B}\cdot\boldsymbol{B}}{8\pi},$$

where ϵ is the thermal energy per unit mass. The additional solenoidality constraint,

$$\boldsymbol{\nabla}\cdot\boldsymbol{B} = 0,$$

must also be fulfilled. The MHD equations must be closed by an equation of state which gives the gas pressure as a function of the density and the thermal energy per unit mass

$$p = p(\rho, \epsilon)\,,$$

usually available to the program in tabulated form. The radiative source term is given by

$$q_{\mathrm{rad}} = 4\pi\rho\int\kappa_\nu(J_\nu - B_\nu)\mathrm{d}\nu\,,$$

$$J_\nu(\boldsymbol{r}) = \frac{1}{4\pi}\oint I_\nu(\boldsymbol{r},\boldsymbol{n})\mathrm{d}\Omega\,, \qquad I(\boldsymbol{r},\boldsymbol{n}) = I_0 e^{-\tau_0} + \int_0^{\tau_0}\left(\frac{\sigma}{\pi}T^4(\tau)\right)e^{-\tau}\mathrm{d}\tau$$

Equations and boundary conditions (cont.)

Typical boundary conditions for the thermal variables and velocities

$$\frac{\partial v_{x,y,z}}{\partial z} = 0 \quad (\,\mathrm{or} \quad v_z = 0\,)\,; \;\lim_{t\to\infty} \epsilon = \epsilon_0$$

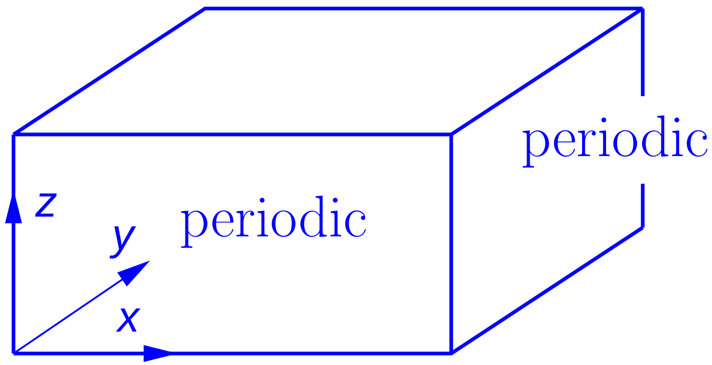

$$\frac{\partial v_{x,y}}{\partial z} = 0\,; \;\int \rho v_z \,\mathrm{d}\sigma = 0\,; \;\mathrm{outflow:}\; \frac{\partial s}{\partial z} = 0$$

$$\mathrm{inflow:}\; s = s_0$$

Periodic lateral boundary conditions in all variables. *Open bottom boundary* in the sense that the fluid can freely flow in and out of the computational domain under the condition of vanishing total mass flux.

Reflecting (closed) top boundary or open (transmitting) top boundary.

Boundary conditions for the magnetic field:

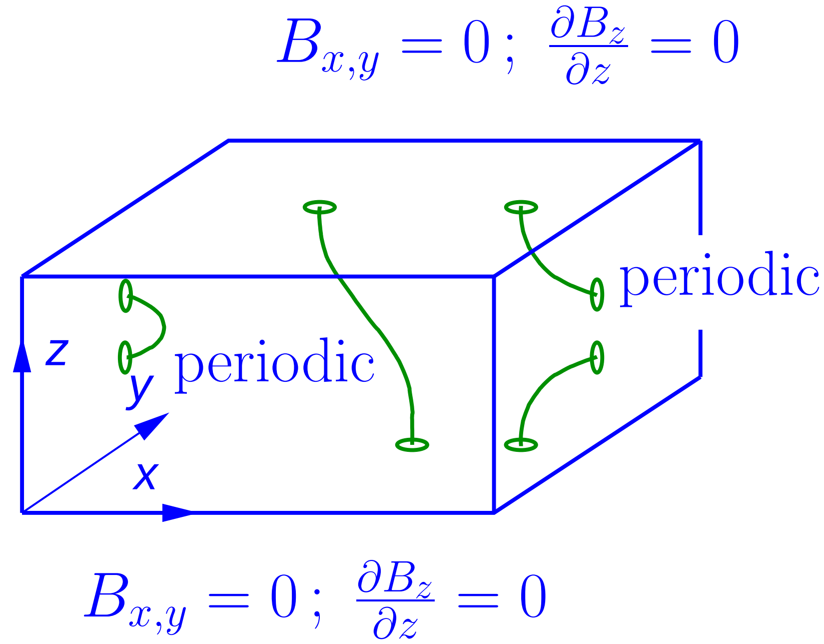

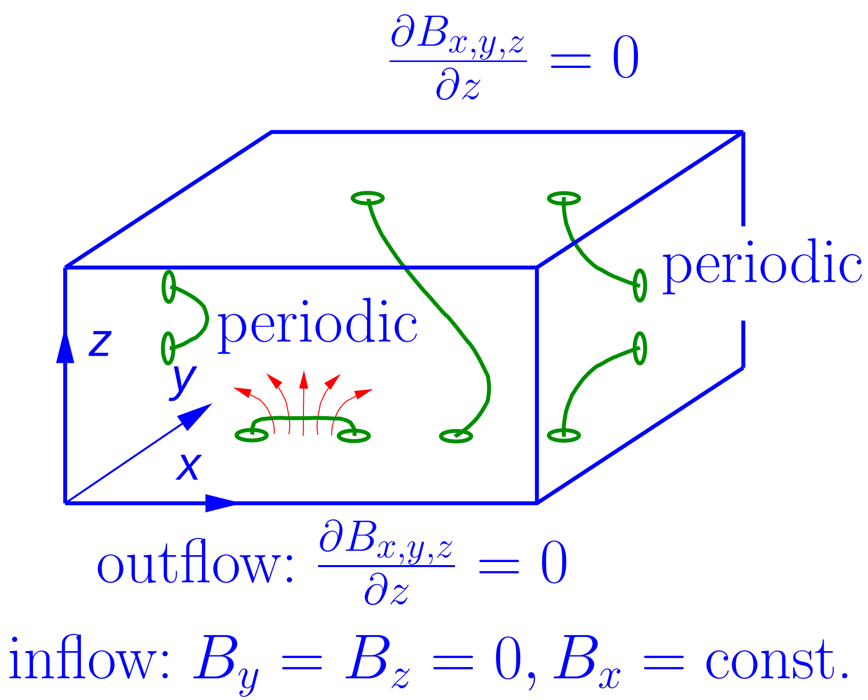

§ 12 Radiation transfer

The radiative source term is given by

$$q_{\rm rad} = -\boldsymbol{\nabla}\cdot\boldsymbol{F}_{\textsf{rad}} = 4\pi\rho\int\kappa_\nu(J_\nu - B_\nu)\mathrm{d}\nu\,,$$

$$J_\nu(\boldsymbol{r}) = \frac{1}{4\pi}\oint I_\nu(\boldsymbol{r},\boldsymbol{n})\mathrm{d}\Omega\,, \qquad I(\boldsymbol{r},\boldsymbol{n}) = I_0 e^{-\tau_0} + \int_0^{\tau_0}\left(\frac{\sigma}{\pi}T^4(\tau)\right)e^{-\tau}\mathrm{d}\tau$$

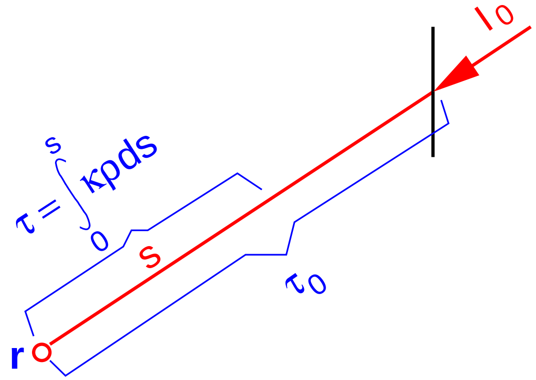

κ_ν: opacity per unit mass [cm^{2}g^{-1}]

τ: optical distance to $\boldsymbol{r}$

Radiation transfer (cont.)

The (magneto-)hydrodynamics step (advection step) is done independently of the radiative transfer step by *operator splitting*. The radiative transfer step consists of an energy update step.

Radiative transfer scheme:

- Formal solution of the one-dimensional radiation transfer equation for 'long rays'. Typically 6 angles in altitude (θ direction) and 4 angles in azimuth (φ direction)
- Realistic (tabulated) opacities
- Grey (one representative frequency point) or frequency dependent treatment with multi-group method (typically 5 opacity bands)
- Strict LTE (no scattering, radiation pressure ignored). $\Rightarrow$ All rays are independent of each other lending itself to good parallelization

1. Interpolation from HD grid to RT ray system

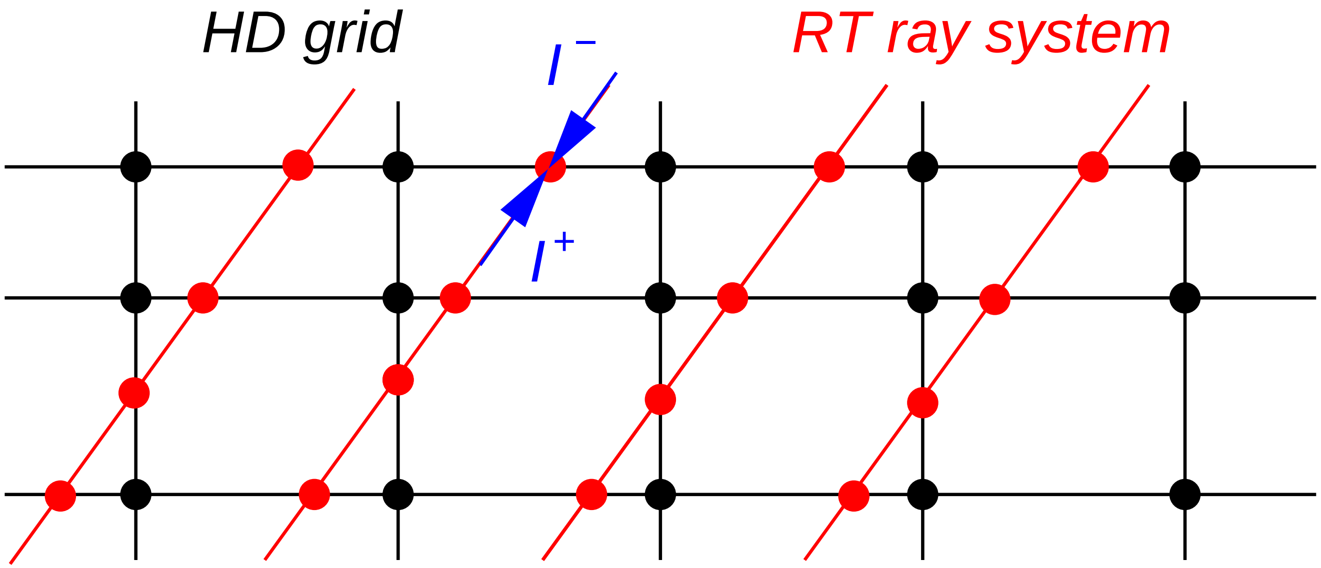

HD grid: ρ, e $\xrightarrow{\text{EOS}}$ p, T $\longrightarrow$ source function S, opacity $\rho\kappa$

$\longrightarrow$ interpolation (linear) $\longrightarrow$ RT Rays system: S, $\rho\kappa$

(no velocity needed)

2. Solution of transfer equation along rays

Ray system: $\rho\kappa \quad \longrightarrow \quad \tau$, $S(\tau)$

$$\frac{\partial^2 y_\nu}{\partial \tau_\nu^2} = y_\nu - \frac{\partial^2 S_\nu}{\partial \tau_\nu^2}; \quad y_\nu = \underbrace{\frac{1}{2}(I_\nu^+ + I_\nu^-)}_{u_\nu} - S_\nu$$

Solution using the Fautrier scheme

Boundary conditions:

Top($\tau > 0$): incident intensity according to $T(\tau = 0) = T_{\rm surf}$

Bottom: $(u - S) = 0$ or specified flux $\partial u / \partial \tau = f(T_{\rm eff})$

$\Rightarrow (u - S)$ along ray at each depth point

3. Back-interpolation from RT ray system to HD grid

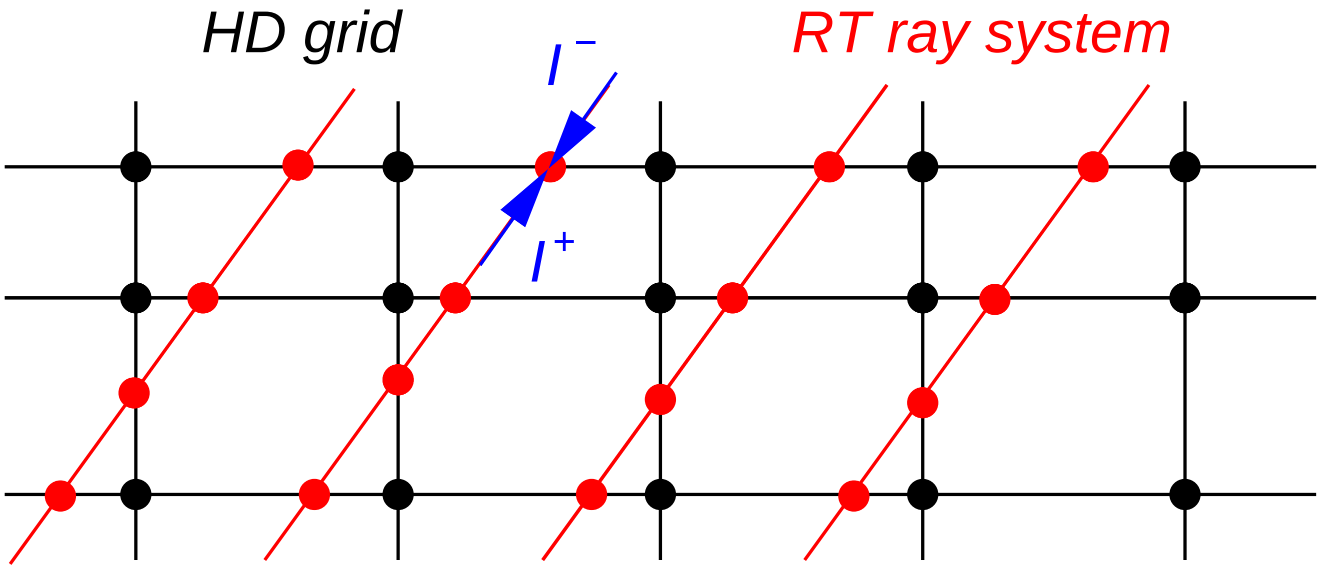

RT Ray system: $\rho\kappa(u - S)$ $\longrightarrow$ flux conservative back-interpoation

$\longrightarrow$ HD grid: $\rho\kappa(u - S)$

4. Angle and frequency integration on HD grid

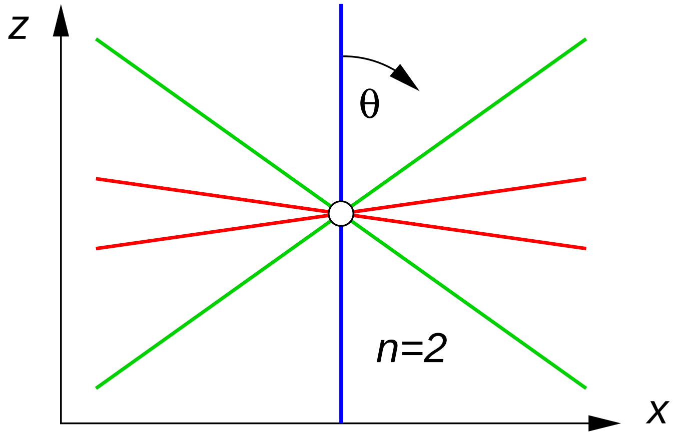

Lobatto or Gauss quadrature formula for

θ-integration

1 vertical and n inclined rays

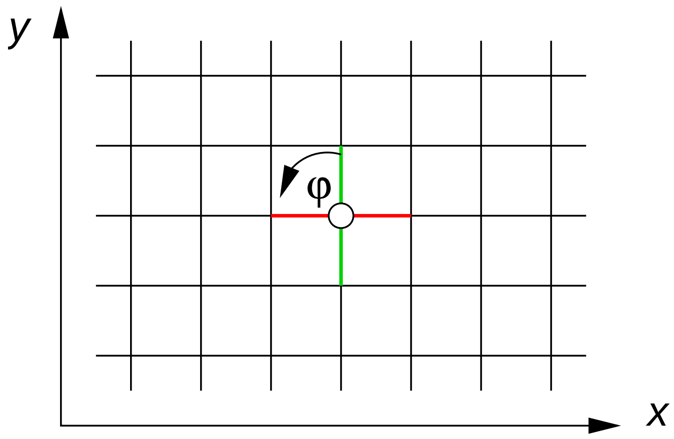

Simple φ-integration

$\phi = 0°, 90°, 180°, 270°$ (fixed for 3-D)

5. Energy update

Summation over θ, φ, and frequency:

$$Q_{\rm rad} = 4\pi \int_0^\infty \rho\kappa_\nu (J_\nu - S_\nu) \mathrm{d}\nu = \sum_{k=1}^{N_{\rm bin}} \sum_{j=1}^{N_\varphi} w_{\varphi,j} \sum_{i=1}^{N_\theta} w_{\theta,i}\, q(\theta_i, \varphi_j, b_k)$$

where $q(\theta_i, \varphi_j, b_k) = \rho\kappa(u - S)(\theta_i, \varphi_j, b_k)$.

Energy update:

$$e(t + \Delta t) = e(t) + \Delta t \frac{Q_{\rm rad}}{\rho}$$

Radiative flux:

$$\int_{z_0}^{z_1} \langle Q_{\rm rad}(x, y, z) \rangle_{x,y} \mathrm{d}z = \langle F_{\rm rad}(x, y, z_1) \rangle_{x,y} - \langle F_{\rm rad}(x, y, z_0) \rangle_{x,y}$$

MSrad3D control parameters

Parameter	Description	Example
opta file	name of opacity table	g2vb.opta
n_radband	gray or multi group RT (1,2,3,4)	2
c_radhtautop	opacity scale height at upper bndr	60.0E+05
c_tsurf	$T_{\rm surf}$ = c_tsurf $T_{\rm eff}$	0.73
n_radthickpoint	number of layers with diffusion RT	48
n_radtheta	number of θ angles (0...4)	2
n_radphi	number of φ angles (0...6 in 2-D)	2
n_radsubray	number of rays per Δx of DS-grid	1
n_radtaurefine	number of RT levels per Δz of HD grid	3
radraybase	quadrature method for θ-integration	lobatto
bottom_bound	lower bnd condition for RT	inoutflow

Radiation transfer (cont.)

MSrad3D controlparameter *c_radhtautop* and *c_tsurf*

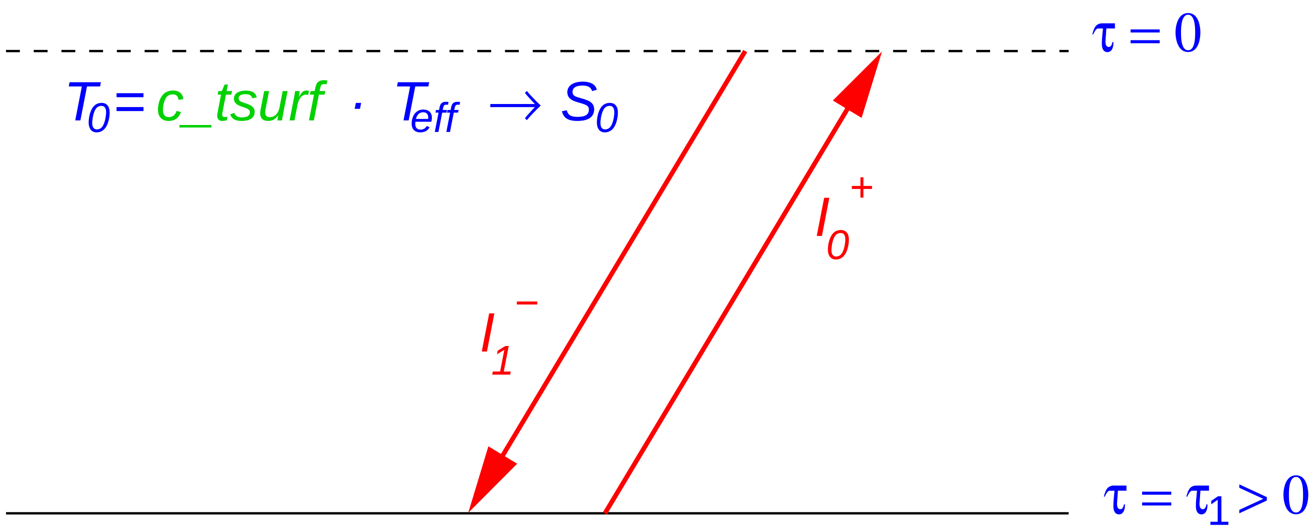

upper boundary of physical domain, index 1

$\tau_1 = c\_radhtautop \cdot \rho_1 \kappa_1 ; \; T_1 \rightarrow S_1$

$$
\begin{aligned}
I_1^- &= S_0\{(1-f)/\tau_1 - f\} + S_1\{1-(1-f)/\tau_1\}, \qquad f = e^{-\tau_1} \\
I_0^+ &= I_1^+ e^{-\tau_1} + S_1\{(1-f)/\tau_1 - f\} + S_0\{1-(1-f)/\tau_1\}
\end{aligned}
$$

MSrad3D controlparameter *n_radthickpoints*

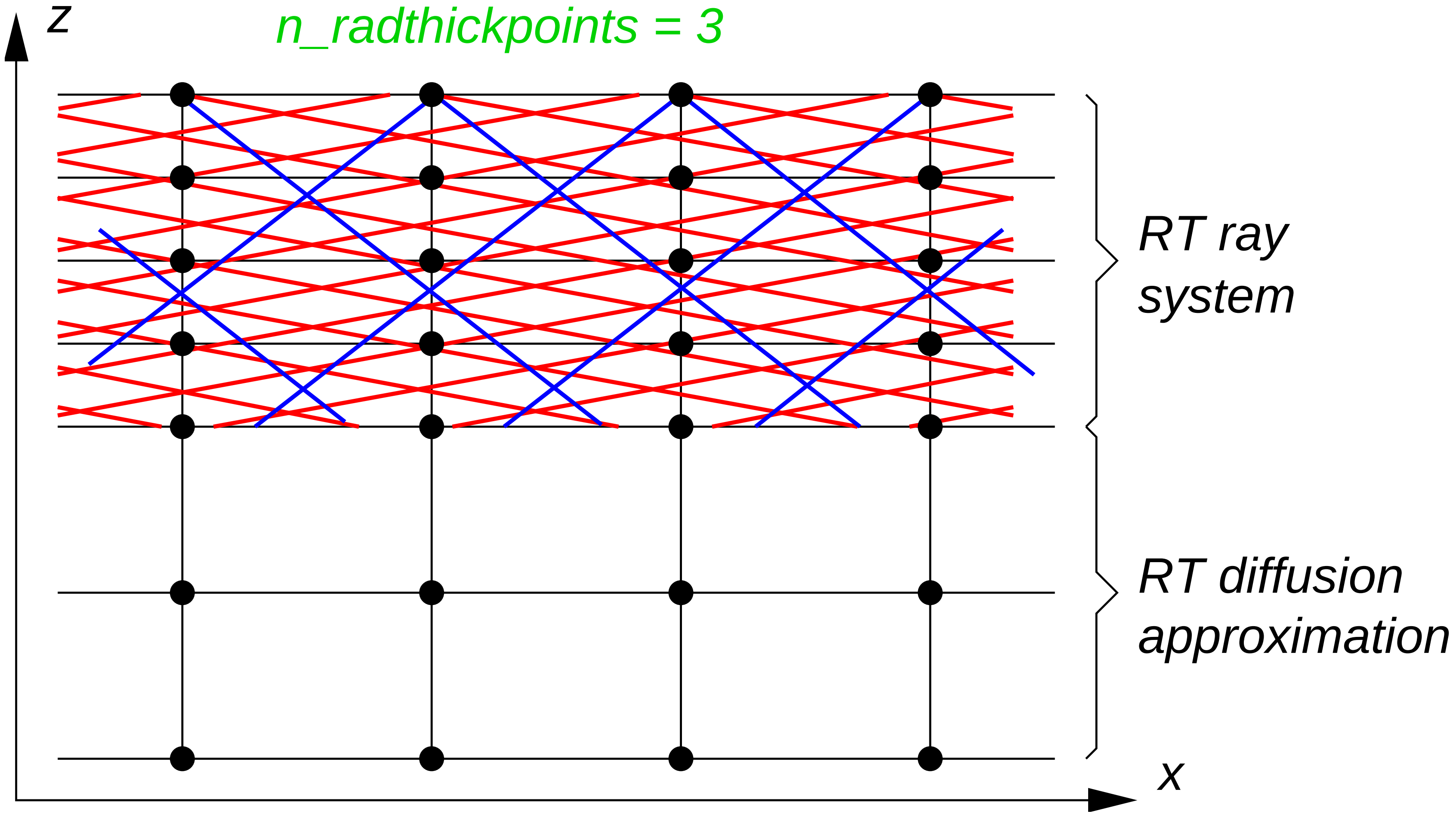

MSrad3D controlparameter *c_radsubray*

n_radsubray = 3

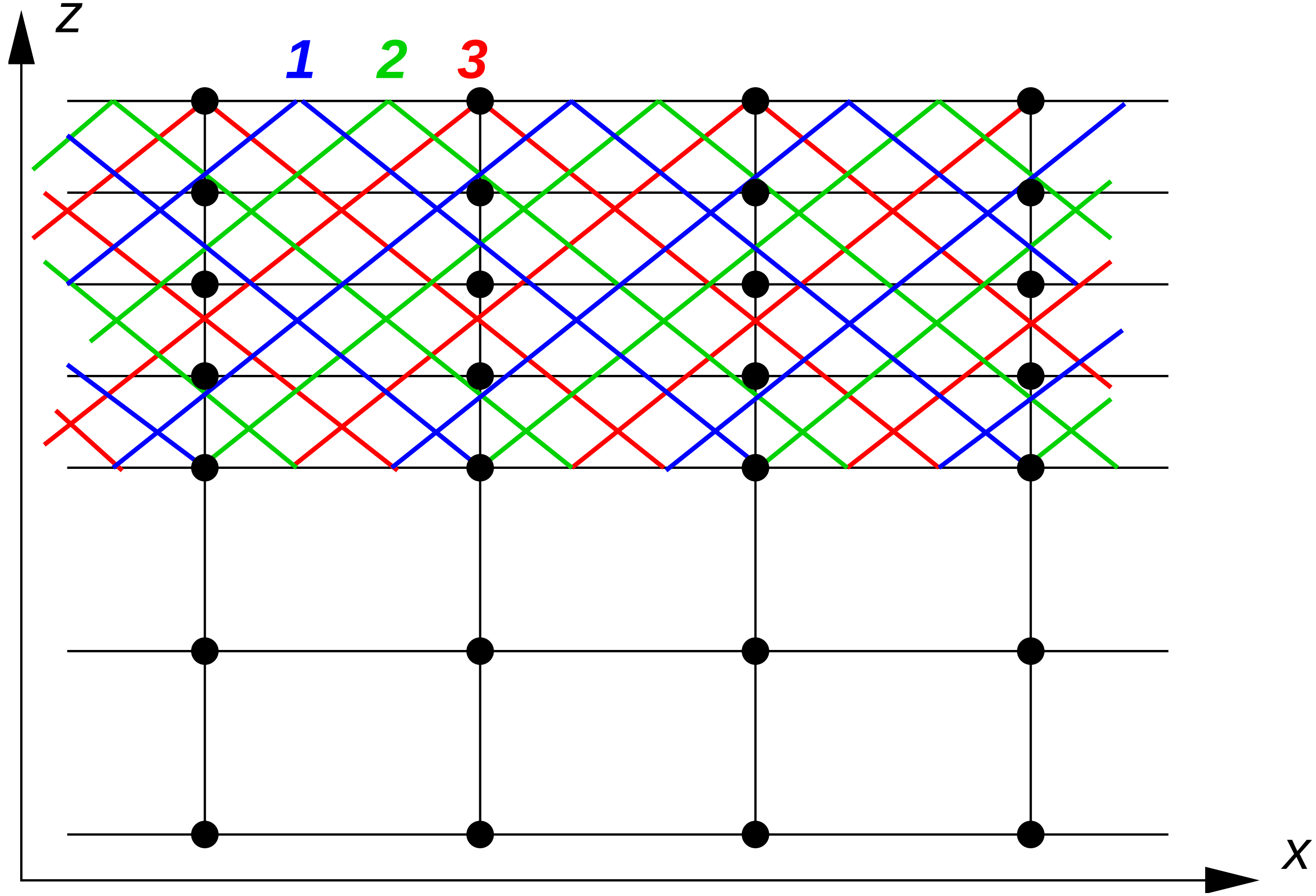

MSrad3D controlparameter *n_radhtaurefine*

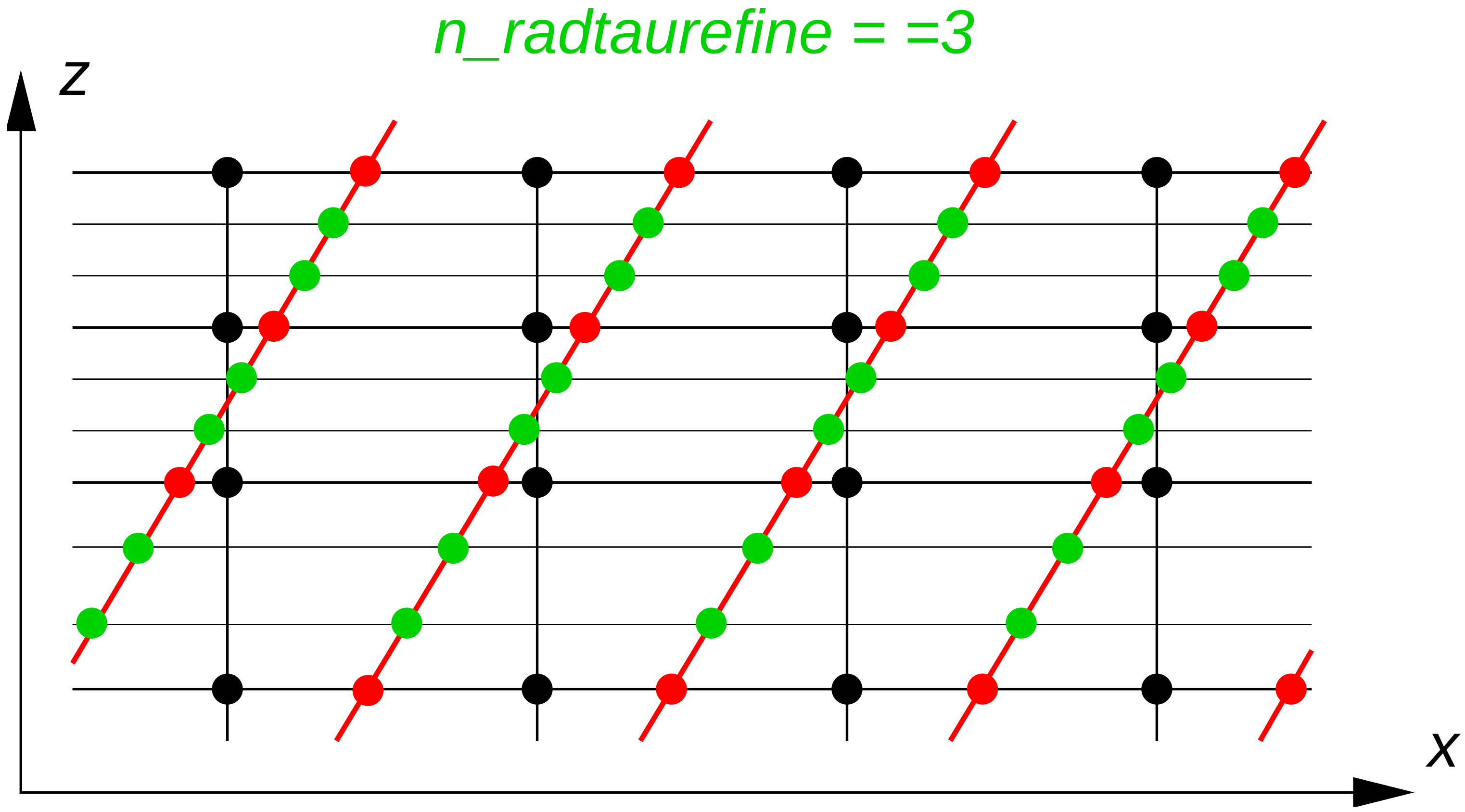

MSrad3D controlparameter *bottom_bound* The radiation transfer equation is solved using a modified Fautrier scheme.

$$\frac{\partial^2 y_\nu}{\partial \tau_\nu^2} = y_\nu - \frac{\partial^2 S_\nu}{\partial \tau_\nu^2}; \quad y_\nu = \underbrace{\frac{1}{2}(I_\nu^+ + I_\nu^-)}_{u_\nu} - S_\nu$$

Boundary conditions:

bottom_bound $=$ inoutflow $\quad \Rightarrow \quad y_\nu = (y_\nu - S_\nu) = 0 \qquad (\nabla F_{\rm rad} = 0)$

else $\quad \Rightarrow \quad \partial u_\nu / \partial \tau = (3/4) F_{\rm rad} / \pi w_\nu \cos(\theta)$

§ 12.1 Multi-group radiation transfer

Nordlund, 1982; Ludwig, 1992

$$q_{\mathrm{rad}} = -\boldsymbol{\nabla} \cdot \boldsymbol{F}_{\textsf{rad}} = 4\pi\rho \int \kappa_\lambda (J_\lambda - B_\lambda)\, \mathrm{d}\lambda \,,$$

$$\begin{aligned}
\int \kappa_\lambda (J_\lambda - B_\lambda)\, \mathrm{d}\lambda &= \sum_j \kappa_{\lambda_j} (J_{\lambda_j} - B_{\lambda_j})\, w_{\lambda_j} \\
&= \sum_i \sum_{j(i)} \kappa_{\lambda_j} (J_{\lambda_j} - B_{\lambda_j})\, w_{\lambda_j} \\
&= \sum_i \sum_{j(i)} \kappa_{\lambda_j} (\boldsymbol{\Lambda}_{\lambda_j}(B_{\lambda_j}) - B_{\lambda_j})\, w_{\lambda_j} \\
&\approx \sum_i \kappa_i (\boldsymbol{\Lambda}_i - \mathbf{1}) (\sum_{j(i)} B_{\lambda_j}\, w_{\lambda_j}) \\
&\doteq \sum_i \kappa_i (\boldsymbol{\Lambda}_i - \mathbf{1}) (B_i\, w_i) \doteq \sum_i \kappa_i (J_i - B_i) w_i
\end{aligned}$$

Strategy for opacity binning:

- concentrate on radiative transfer in vertical direction,
- group together frequencies with as similar a $\tau_\nu(s)$-relationship as possible, so that $\mathbf{\Lambda}_{\lambda_{j(i)}}$ is very similar $\forall j$ of a given bin i,
- choose clever averaging procedure for κ_ν, (Rosseland averages for $\tau_i > 1$, Planck averages for $\tau_i < 1$).

The art of opacity binning: Constructing the bands (H.-G. Ludwig, Paris Obs.)

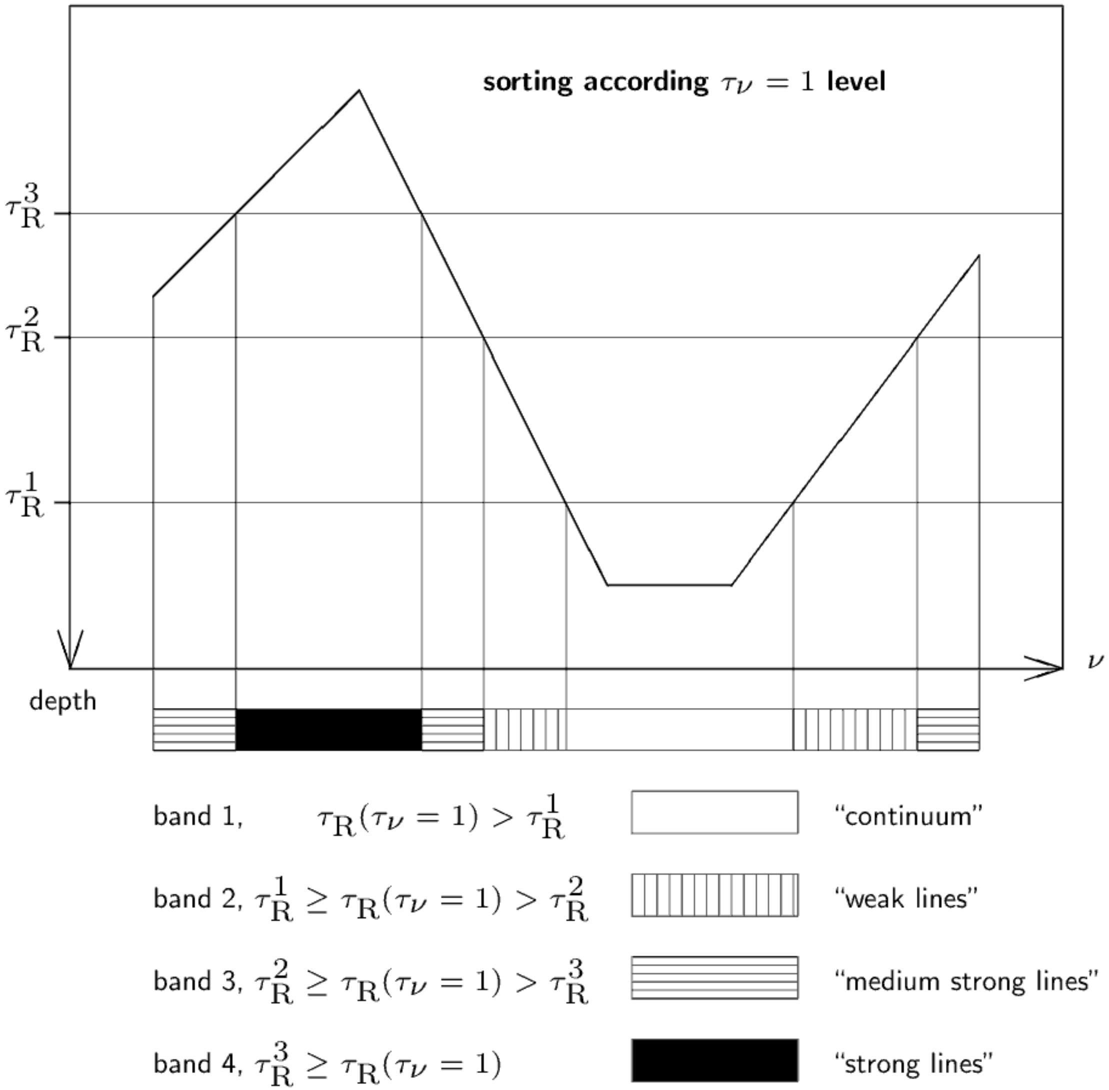

Testing the OBM. Integrated radiative flux

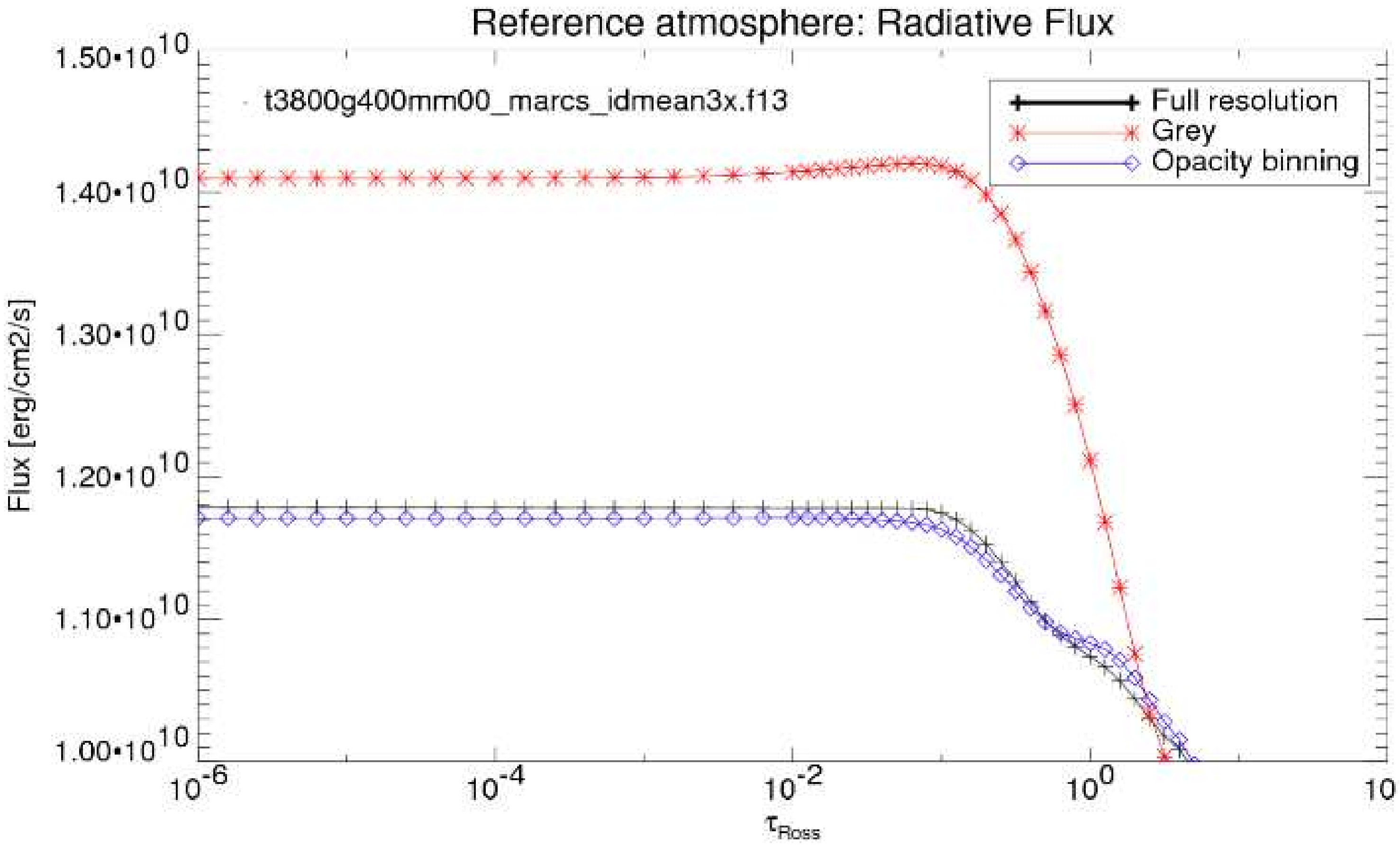

Intensity maps for different opacity bins

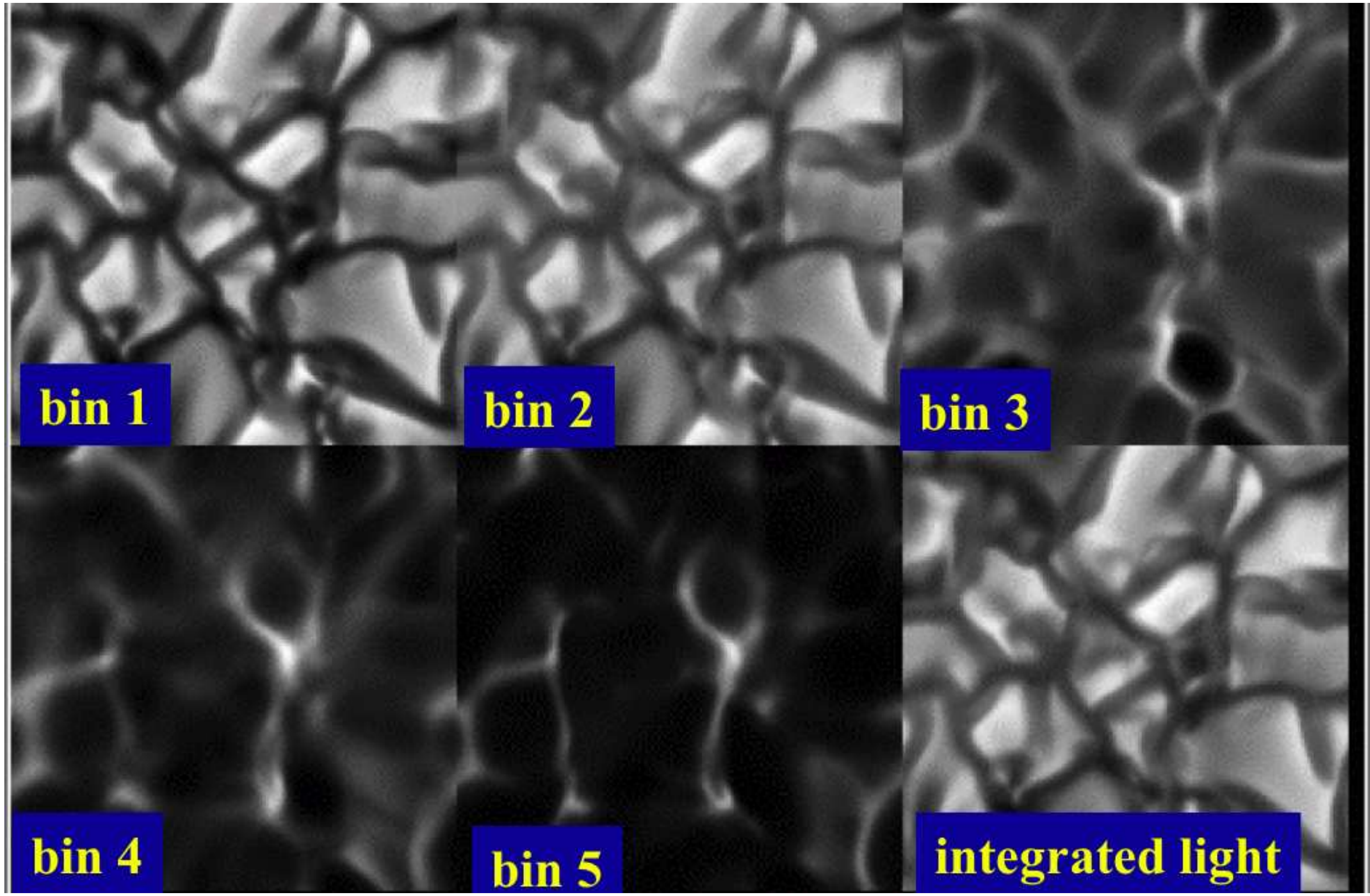

Notice that bin 3 to 5 show “inverse granulation” as their opacities represent medium to strong line cores.

Mean enthalpy flux, kinetic energy flux, and radiative energy flux as a function of height

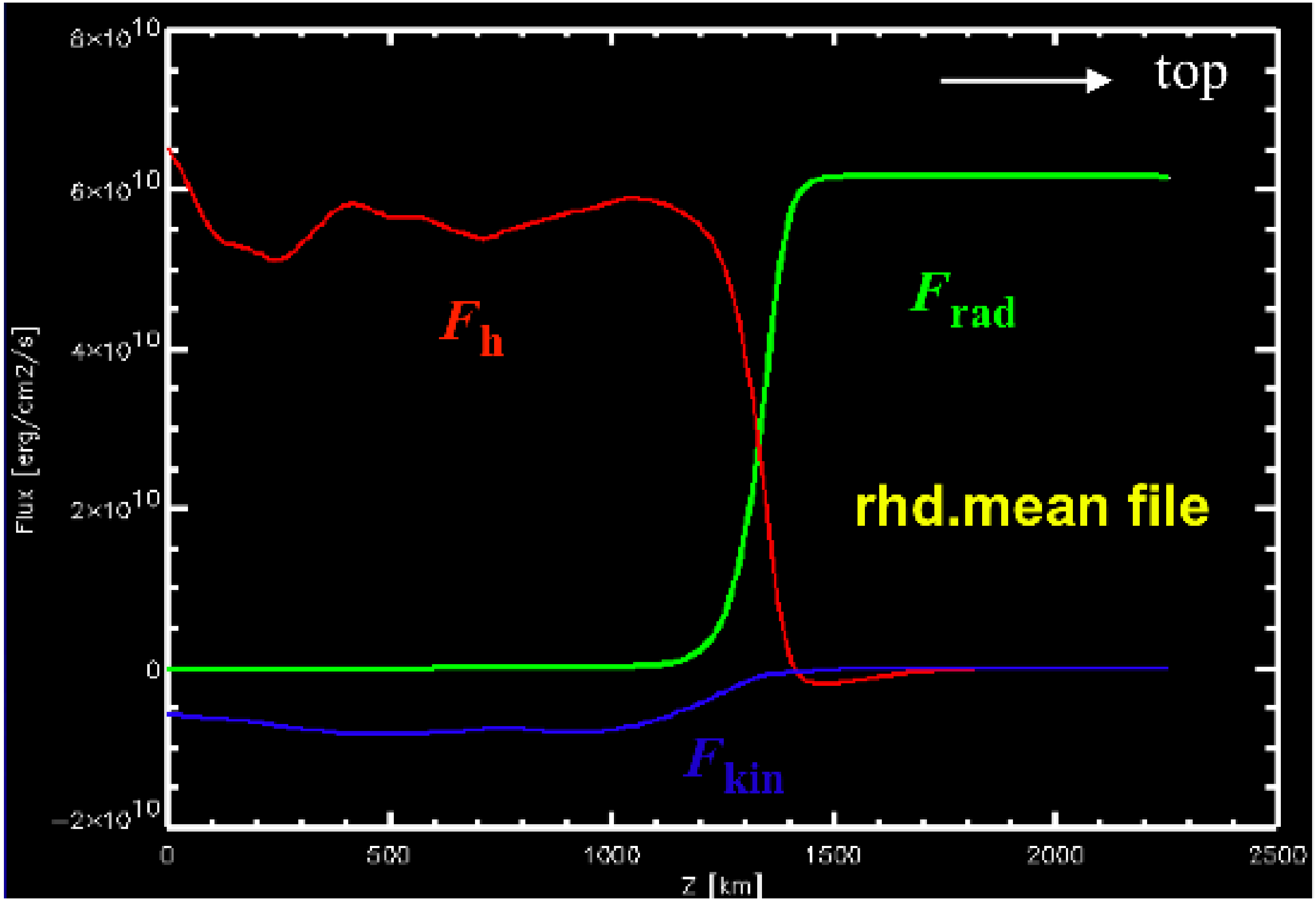

Radiative cooling (bright) and heating (dark), $Q_{\rm rad}$

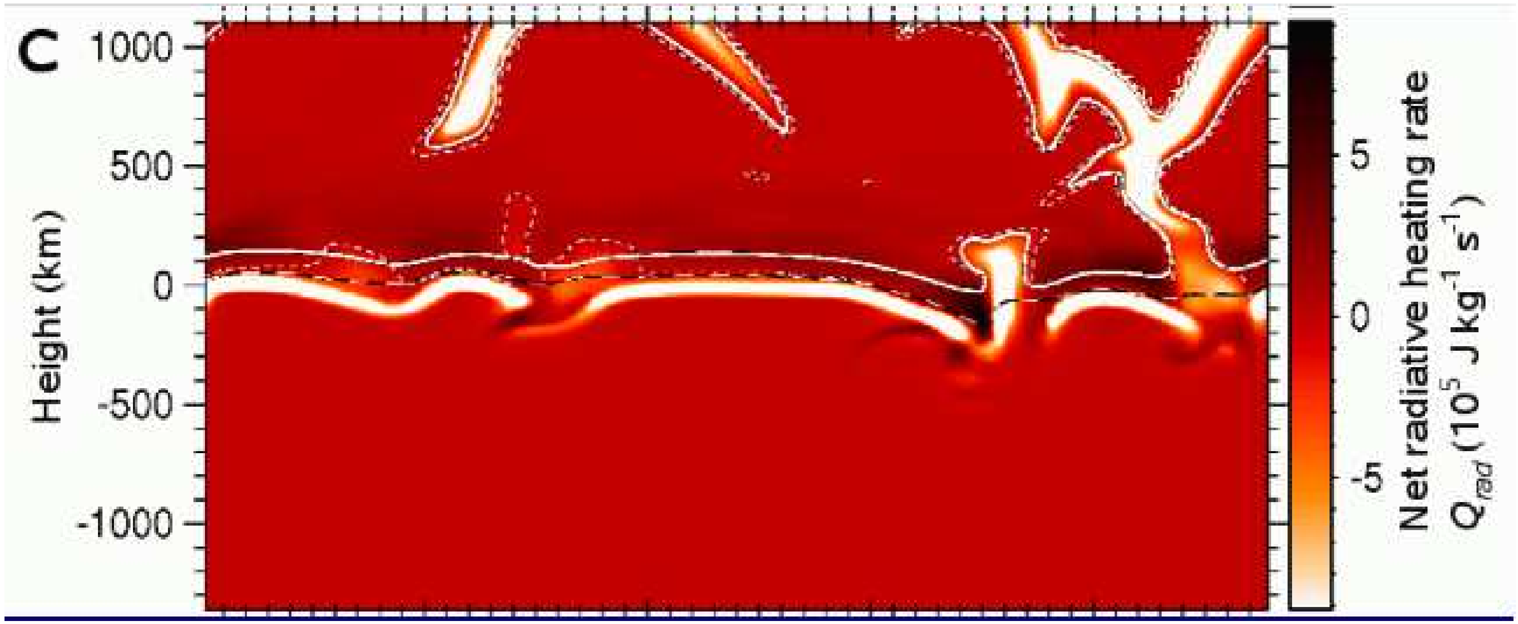

Note that there is slight radiative heating in the low photosphere due to the "line blanketing".

§ 13 Chemical reaction network

For certain applications, e.g., the effect of CO in the solar atmosphere, an optional module for the treatment of a network of chemical reactions was added to the CO^{5}BOLD code. For further details see *Wedemeyer-Böhm et al. (2005), A&A 438, 1043* and *Wedemeyer-Böhm & Steffen (2007), A&A 462, L31*.

The *operator splitting* method is used in order to account for the time evolution of chemical species. In a *first step* the chemical species are advected together with all the other hydrodynamic quantities:

$$\frac{\partial n_i}{\partial t} + \nabla \cdot (n_i \boldsymbol{v}) = 0 \,,$$

where n_i is the number density of a chemical species and $\boldsymbol{v}$ the velocity of the hydrodynamical flow.

Chemical reaction network (cont.)

In a *second step* (between the hydro step and the radiation-transfer step), the change in number density due to chemical reactions is accounted for:

$$
\begin{aligned}
\left(\frac{\partial n_i}{\partial t}\right)_{\rm chem} \quad = \quad & -n_i \sum_j k_{2,ij}\, n_j \\
& + \sum_j \sum_l k_{2,jl}\, n_j n_l \\
& - n_j \sum_j \sum_l k_{3,ijl}\, n_j n_l \\
& + \sum_j \sum_l \sum_m k_{3,jlm}\, n_j n_l n_m \ ,
\end{aligned}
$$

where n_i is the number densities of species i, which decreases or increases due to two-body reactions with rates $k_{2,ij}$ and $k_{2,jl}$, respectively. Three-body reactions are analogously accounted for by the third and fourth term with rates $k_{3,ijl}$ and $k_{3,jlm}$. It results in a (stiff!) system of of ordinary differential equations.

Chemical reaction network (cont.)

The rates have the basic form

$$k = \alpha \, T_{300}^{\beta} \, \mathrm{e}^{-\gamma/T} \; ,$$

where $T_{300} = T/300\,$K. For catalytic reactions the number density of a representative metal n_{M} enters: The rates have the basic form

$$k = n_{\mathrm{M}} \alpha \, T_{300}^{\beta} \, \mathrm{e}^{-\gamma/T} \; .$$

The coefficients α, β, and γ are compiled in tables, e.g., in *Wedemeyer-Böhm et al. (2005), A&A 438, 1043*

Chemical reaction network (cont.)

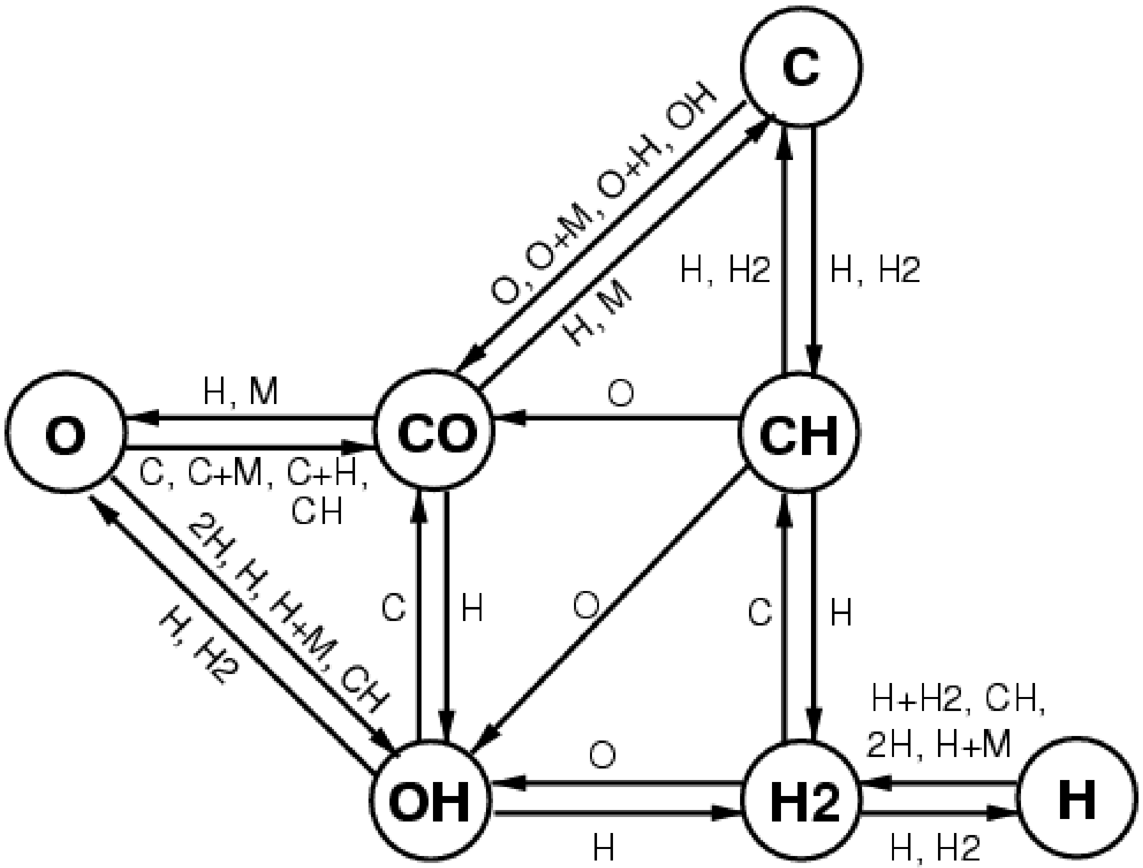

Chemical reaction network:

7 chemical species, H, H_2, C, O, CO, CH, OH, plus a representative metal M

27 chemical reactions

Chemical reaction network (cont.)

Radiative cooling via CO lines:

- Two opacity bands:

  1.) *continuum band* with Rosseland mean opacity κ_{R} without infrared.

  2.) *infrared band* at 4.7 μm with Rosseland mean opacity plus CO line opacity, $\kappa_{\mathrm{R}} + \kappa_{CO}$.

- CO opacity calculated from (time dependent) CO number density.

Application examples:

- movie of CO number density in two-dimensional hydrodynamic solar convection.

- animation of “CO clouds” from a three-dimensional simulation.

§ 14 Non-equilibrium Hydrogen ionization in CO^{5}BOLD

The assumption of strict LTE and the “grey” approximation may be tenable when studying the dynamics of magnetic fields in the chromosphere – it is certainly not adequate for quantitative spectroscopy.

CO^{5}BOLD uses an approximative treatment of the time dependent hydrogen ionization along the lines of *E. Sollum* (Oslo). See *Leenaarts & Wedemeyer-Böhm (2006) A&A 460, 301* for the details.

Under the condition of the solar chromosphere the assumption of LTE (local thermodynamic equilibrium) is not valid. Even the assumption of statistical equilibrium in the rate equations is not valid. Kneer (1980) showed that the relaxation timescale for the ionization of hydrogen varies from 100 s to 1000 s in the middle to upper chromosphere.

In order to compute the *time dependent hydrogen ionization* in a three-dimensional environnment, simplifications are needed. We employ the *method of fixed radiative rates*. We solve the time-dependent rate equations

$$\frac{\partial n_i}{\partial t} + \nabla \cdot (n_i \mathrm{v}) = \sum_{j \neq i}^{n_l} n_j P_{ji} - n_i \sum_{j \neq i}^{n_l} P_{ij}$$

$P_{ij} = C_{ij} + R_{ij}$.

In the method of fixed radiative rates we assume that the radiation field in each transition, both, bound-bound and bound-free, can be described by a formal radiation temperature:

$$J_\nu = \frac{2h\nu^3}{c^2} \frac{1}{\mathrm{e}^{h\nu/kT_{\mathrm{rad}}} - 1}$$

Thus, we obtain the *fixed radiative rates* for bound-bound transitions

$$\begin{aligned} R_{lu} &= B_{lu} J_{\nu_0} = \frac{4\pi^2 e^2}{h\nu_0 m_e c} f_{lu} \frac{2h\nu_0^3}{c^2} \frac{1}{\mathrm{e}^{h\nu_0/kT_{\mathrm{rad}}} - 1} \\ R_{ul} &= A_{ul} + B_{ul} J_{\nu_0} = \frac{g_l}{g_u} \mathrm{e}^{h\nu_0/kT_{\mathrm{rad}}} R_{lu} \end{aligned}$$

Non-equilibrium Hydrogen ionization in CO^{5}BOLD (cont.)

The hydrogen bound-free excitations have a Kramer's absorption cross section:

$$\sigma_{ic}(\nu) = \alpha_0 \left(\frac{\nu_0}{\nu}\right)^3 , \nu > \nu_0 \,,$$

where α_0 is the absorption cross-section at the edge frequency ν_0. In this case the radiative rate coefficients are

$$\begin{aligned} R_{ic} &= 4\pi \int_{\nu_0}^{\infty} \frac{\sigma_{ic}(\nu)}{h\nu} J_\nu \mathrm{d}\nu = \frac{8\pi}{c^2} \alpha_0 \nu_0^3 \int_{\nu_0}^{\infty} \frac{1}{\nu} \frac{1}{\mathrm{e}^{h\nu/kT_{\mathrm{rad}}} - 1} \mathrm{d}\nu \\ &= \frac{8\pi}{c^2} \alpha_0 \nu_0^3 \sum_{n=1}^{\infty} E_1 \left[n \frac{h\nu_0}{kT_{\mathrm{rad}}} \right] , \quad E_1 \text{ being the first exponential integral} \\ R_{ci} &= 4\pi \left[\frac{n_i}{n_c}\right]_{\mathrm{LTE}} \int_{\nu_0}^{\infty} \frac{\sigma_{ic}(\nu)}{h\nu} \left(\frac{2h\nu^3}{c^2} + J_\nu \right) \mathrm{e}^{-h\nu/kT_e} \mathrm{d}\nu \\ &= \frac{8\pi}{c^2} \alpha_0 \nu_0^3 \left[\frac{n_i}{n_c}\right]_{\mathrm{LTE}} \sum_{n=1}^{\infty} E_1 \left[\left(n \frac{T_e}{T_{\mathrm{rad}}} + 1 \right) \frac{h\nu_0}{kT_e} \right] . \end{aligned}$$

Non-equilibrium Hydrogen ionization in CO^{5}BOLD (cont.)

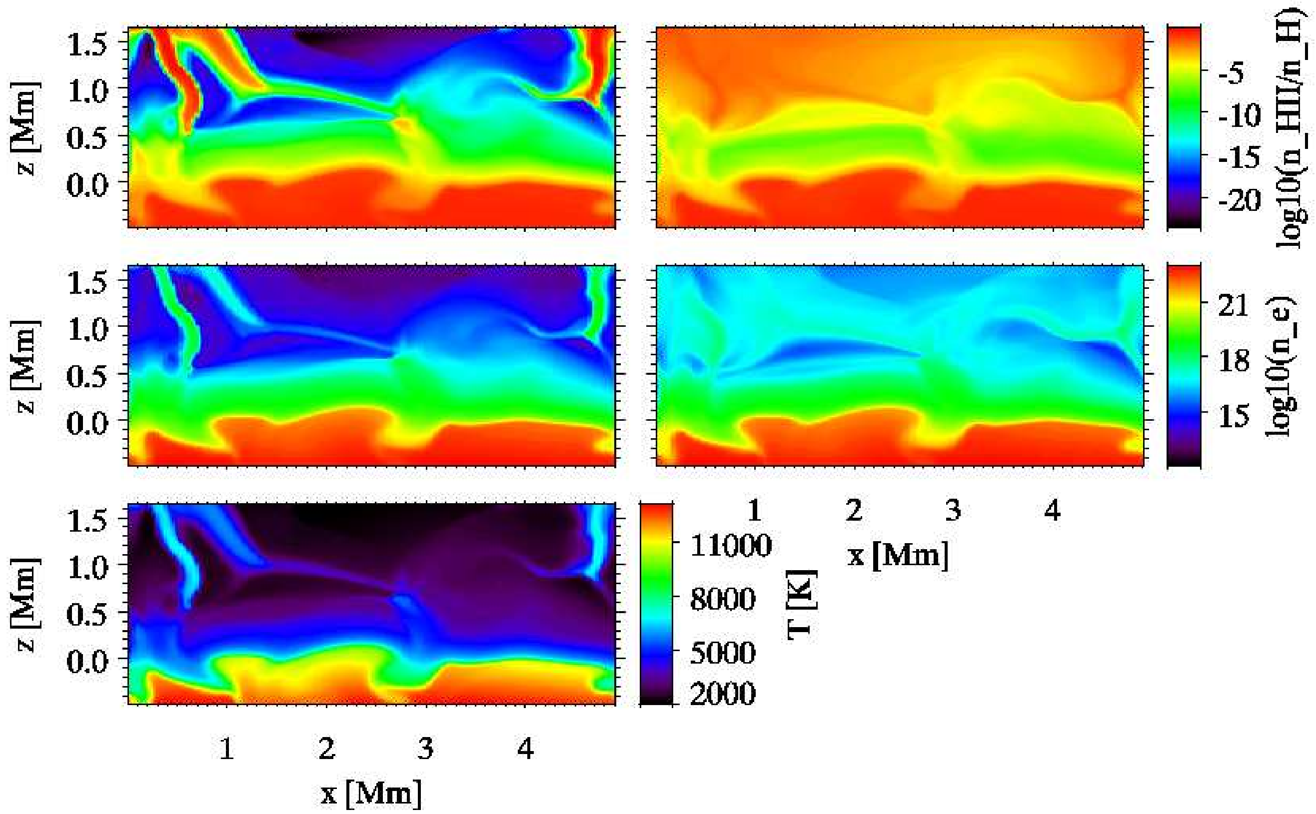

Effect of dynamic H-ionization in the upper part of a 2-D simulation. *Left column: LTE* ionization degree and electron density. *Right column:* Corresponding *time-dependent NLTE* quantities. Bottom left: Gas temperature, which is the same for the LTE and the time-dependent case. *Leenaarts & Wedemeyer-Böhm 2006*

References

Freytag, B., Steffen, M., and Dorch, B.: 2002, *Spots on the surface of Betelgeuse – Results from new 3D stellar convection models*, Astronomical Notes/AN 323, 213-219

Freytag, B., Steffen, M., Ludwig, H.-G., and Holweger, H.: 2004, *Numerical simulation of the three-dimensional structure and dynamics of the non-magnetic solar chromosphere*, A&A 414, 1121-1137

Freytag, B. et al.: 2008, *CO^{5}BOLD user manual*, http://www.astro.uu.se/˜bf/co5bold_main.html

Leenaarts, J. and Wedemeyer-Böhm, S.: 2006, *Time-dependent hydrogen ionisation in 3D simulations of the solar chromosphere. Methods and first results*, A&A 460, 301-307

Ludwig, H.-G.: 1992, *Nichtgrauer Strahlungstransport in numerischen Simulationen stellarer Konvektion*, Ph.D. thesis, Christian-Albrechts-UniversitŁt, Kiel

Nordlund, Å: 1982, *Numerical simulations of the solar granulation*, A&A 107, 1-10

Sollum, E.: 1999, Masters thesis, University of Oslo, Norway

References (cont.)

Wedemeyer-Böhm, S., Kamp, I., Bruls, J., and Freytag, B.: 2005, *Carbon monoxide in the solar atmosphere. I. Numerical method and two-dimensional models*, A&A 438, 1043-1057

Wedemeyer-Böhm, S. and Steffen, M.: *Carbon monoxide in the solar atmosphere. II. Radiative cooling by CO lines*, A&A 462, L31-L35

Wedemeyer-Böhm, S. and Steiner, O.: 2006, *CO^{5}BOLD Workshop*, http://folk.uio.no/svenwe/cws2006/index.html

Part IV: Aspects of computational astrophysics

§ 15 Role of computer simulations

How can astrophysicists

- inform about the first milliseconds of a core collapse supernova,
- know about the past million years of dynamical evolution of a present day galaxy,
- know about the structure formation of the early universe,
- talk about the state of the plasma of stellar interiors as if they had it examined in the laboratory?

Answer: With the help of computational astrophysics!

Role of computer simulations (cont.)

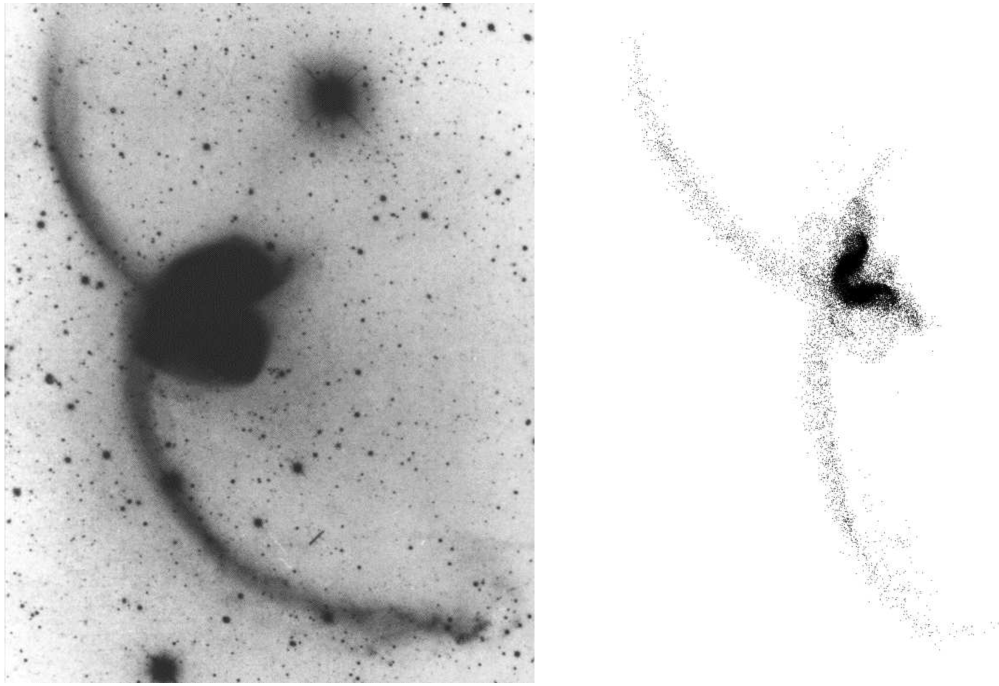

The antenna nebula NGC 4038/4039 evolved from a collision of two similarly sized spiral nebulae. *Left:* Observed present state. *Right:* Present state from a computer simulation of the complete collision (www.ifa.hawaii.edu/˜barnes).

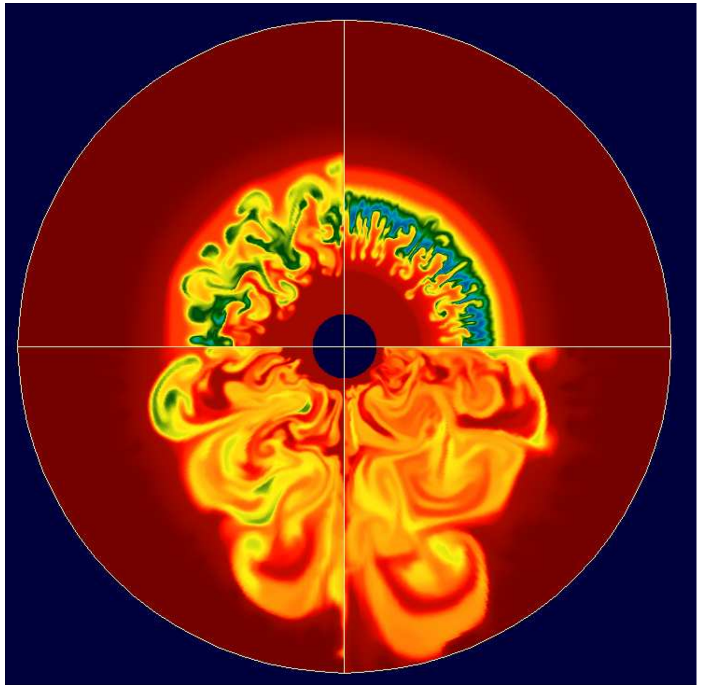

Four instants in the formation of a neutron star in the course of a supernova explosion. From the top right panel counterclockwise 3 milliseconds apart in a radial region from $R = 15$ km to $R = 155$ km (www.MPA-Garching.MPG.de).

Historical Perspective:

- 1950's and 1960's: Stellar evolution calculations (Martin Schwarzshild in the U.S. and Rudolph Kippenhahn in Göttingen, Germany). At that time *computers were viewed as tools for the numerical integration* rather than as a tool for experimentation.

- 1960's: N-body stellar dynamics simulations (e.g. tidal interaction of galaxies) and hydrodynamical systems (e.g. core collapse supernovae). Notion of *computational astrophysics as experimental astronomy*.

  These simulations are generally *motivated by the question "What happens if?"* more so than "What is the solution to these equations?".

Computational astrophysics is the experimentation with astrophysical objects in a virtual (numerical) laboratory, comparable to the manipulation with real probes in classical physics experiments.

Role of Computational astrophysics:

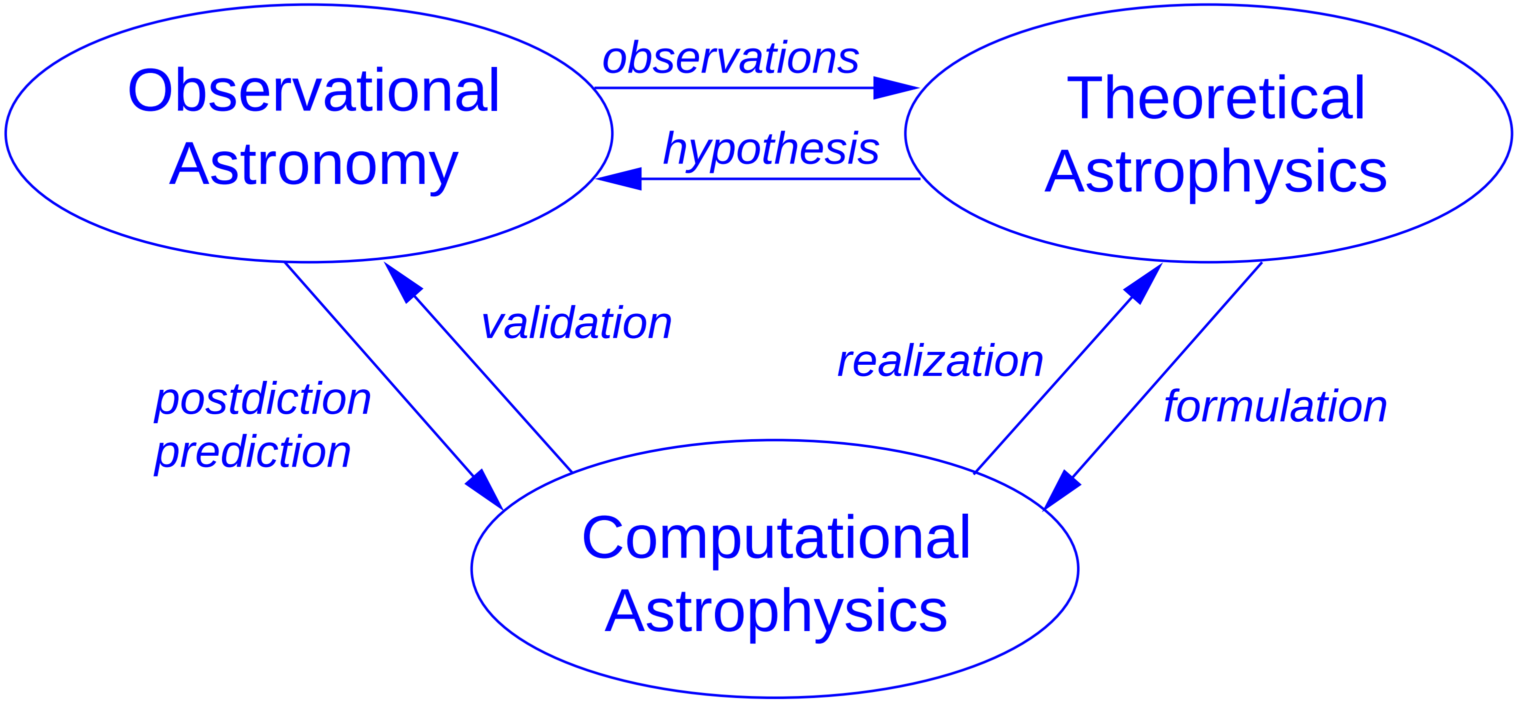

Adapted from *M. Norman (1997)*

Role of computer simulations (cont.)

Interaction theory $\leftrightarrow$ computational astrophysics

- Theory provides the mathematical formulation for the simulation.
- Analytical properties of the solution can be incorporated into the numerical algorithm (e.g., conservation laws, Rankine-Hugoniot relations, etc.).
- Analytical solutions provide *test problems* for validation.
- Complex simulation results can post facto be reduced to *analytical toy models*, which nonetheless capture the essential physics (to become enshrined in astronomy textbooks).
- Simulations provide realizations of the theoretical formulation. They may hint at missing ‘physics’ in the formulation and build *physical intuition* regarding the phenomena embodied in the governing equations.
- *Numerical experiments* aim at revealing the essential physics of an astrophysical process.

Interaction observation $\longleftrightarrow$ computational astrophysics

- Observations provide the final *validation* of the simulation.
- *Postdiction* of available observational data in the early phase.
- *Prediction* of observational data with more mature simulations.

For the comparison of simulation results with observations it is essential that observable quantities, for short *observables*, are computed, i.e., *synthesized* from the simulation data. Results from such “numerical” or *“virtual observations”* are sometimes called *“synthetic data”*.

The generation of synthetic observables from the simulation data is often as time consuming as the simulation itelf.

Progress in computational astrophysics:

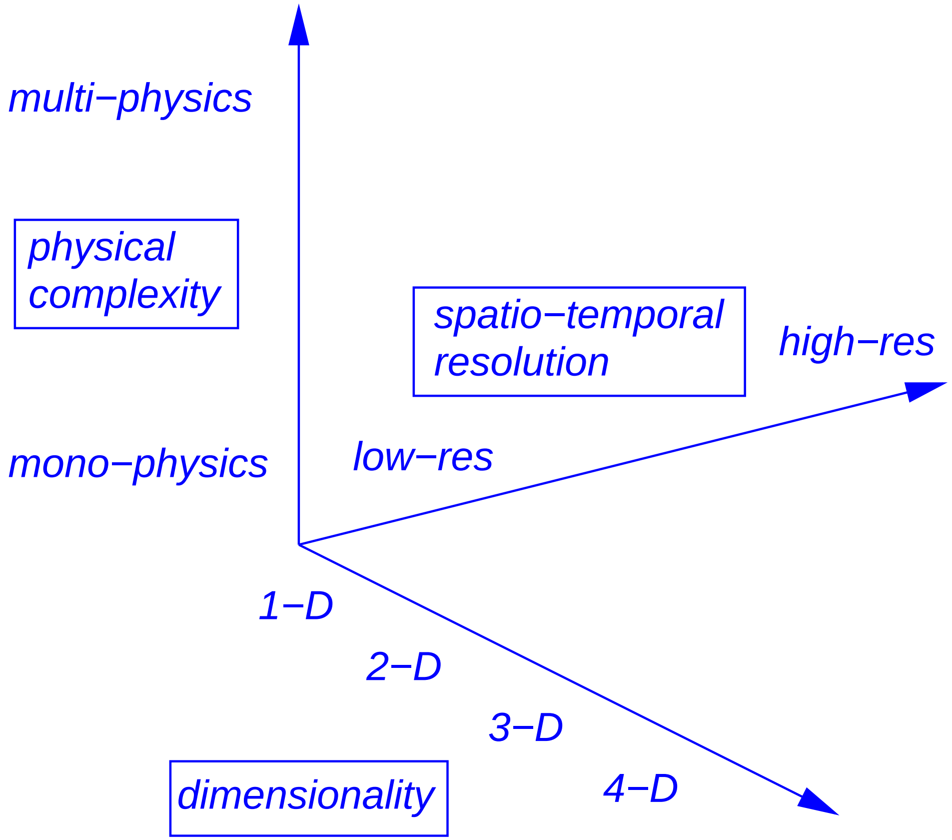

Adapted from *M. Norman (1997)*

References

Kippenhahn, R.: 2008, Als die Computer die Astronomie eroberten, Reviews in Modern Astronomy 20, 1-14

Norman, M.: 1997, Computational Astrophysics: The "New Astronomy" for the 21st Century, in ASP Conf. Series Vol. 123, D.A. Clarke & M.J. West (eds.), p. 3-14

Ostriker, J.P.: 2000, Historical Reflection on the Role of Numerical Modeling in Astrophysics, Reviews in Modern Astronomy 13, 1-11

Part V: MHD simulations: Case studies

§ 16 *Case study I:* Magnetic fields of the quiet Sun

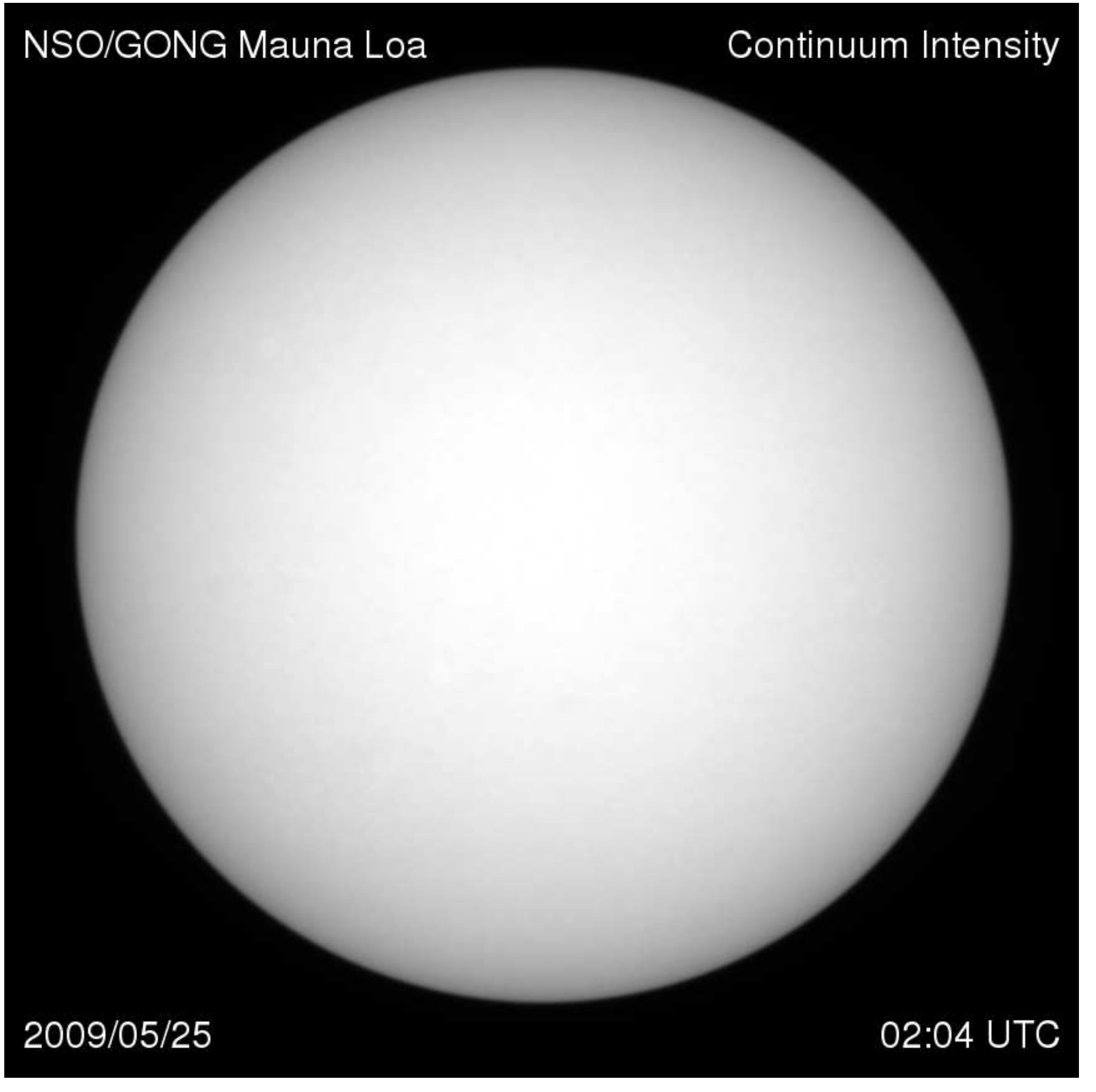

Case study I: Magnetic fields of the quiet Sun (cont.)

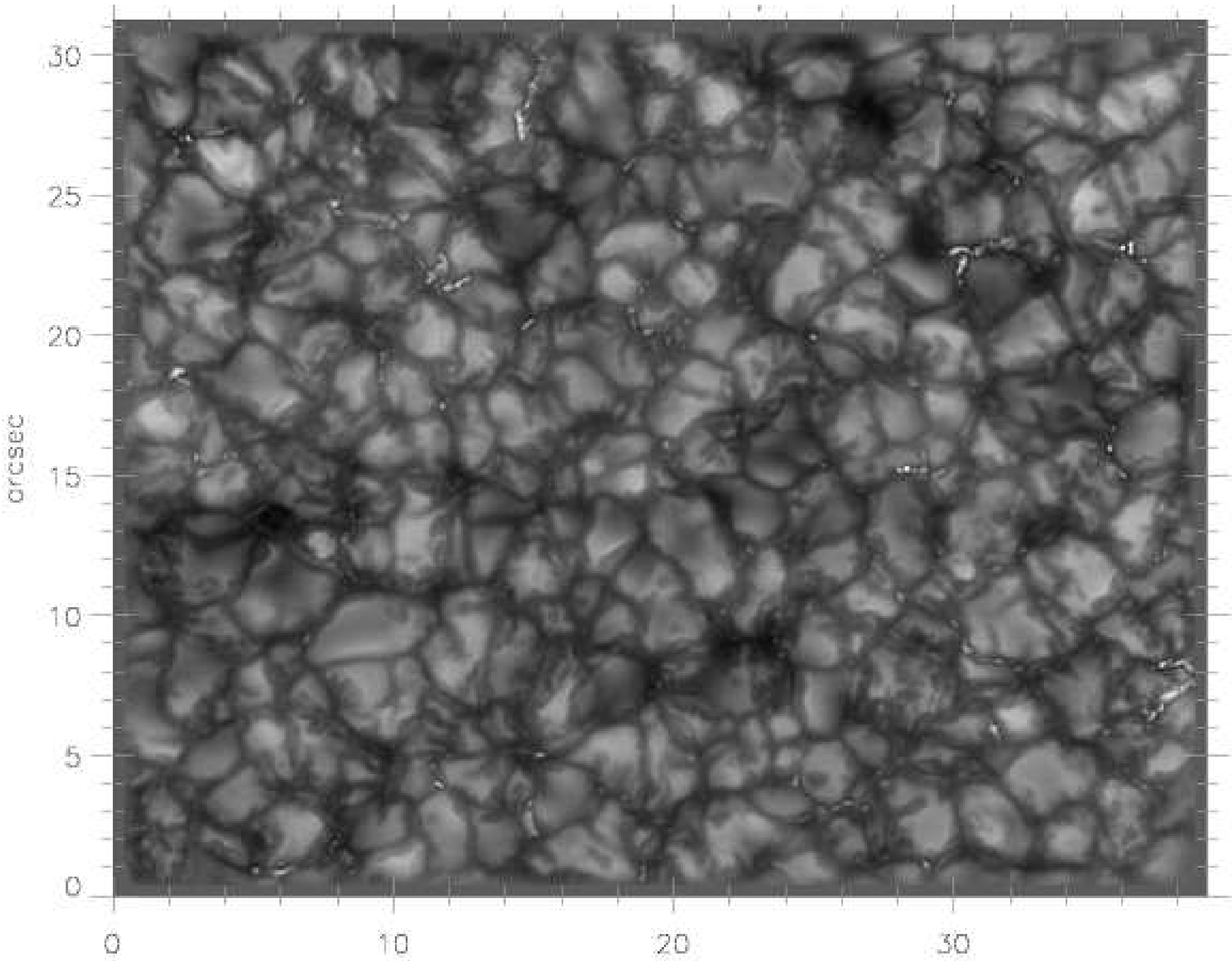

Continuum at 395 nm with the VTT and KAOS at Tenerife

The filigree, *Dunn & Zirker, 1973*.
Facular points, *Mehltretter, 1973*.
G-band bright points, *Muller, 1985*.
Ribbon bands, Flowers etc., *Berger et al. 2004*.

Case study I: Magnetic fields of the quiet Sun (cont.)

Hinode (Solar-B) launched on 22 September 2006. The Solar Optical Telescope (SOT) has an aperture of 50 cm featuring an image stabilization system consisting of a piezo-driven tip-tilt mirror. The Spectral-polarimeter (SP) generates Stokes $IQUV$ spectral images.

`http://solar-b.nao.ac.jp`

Case study I: Magnetic fields of the quiet Sun (cont.)

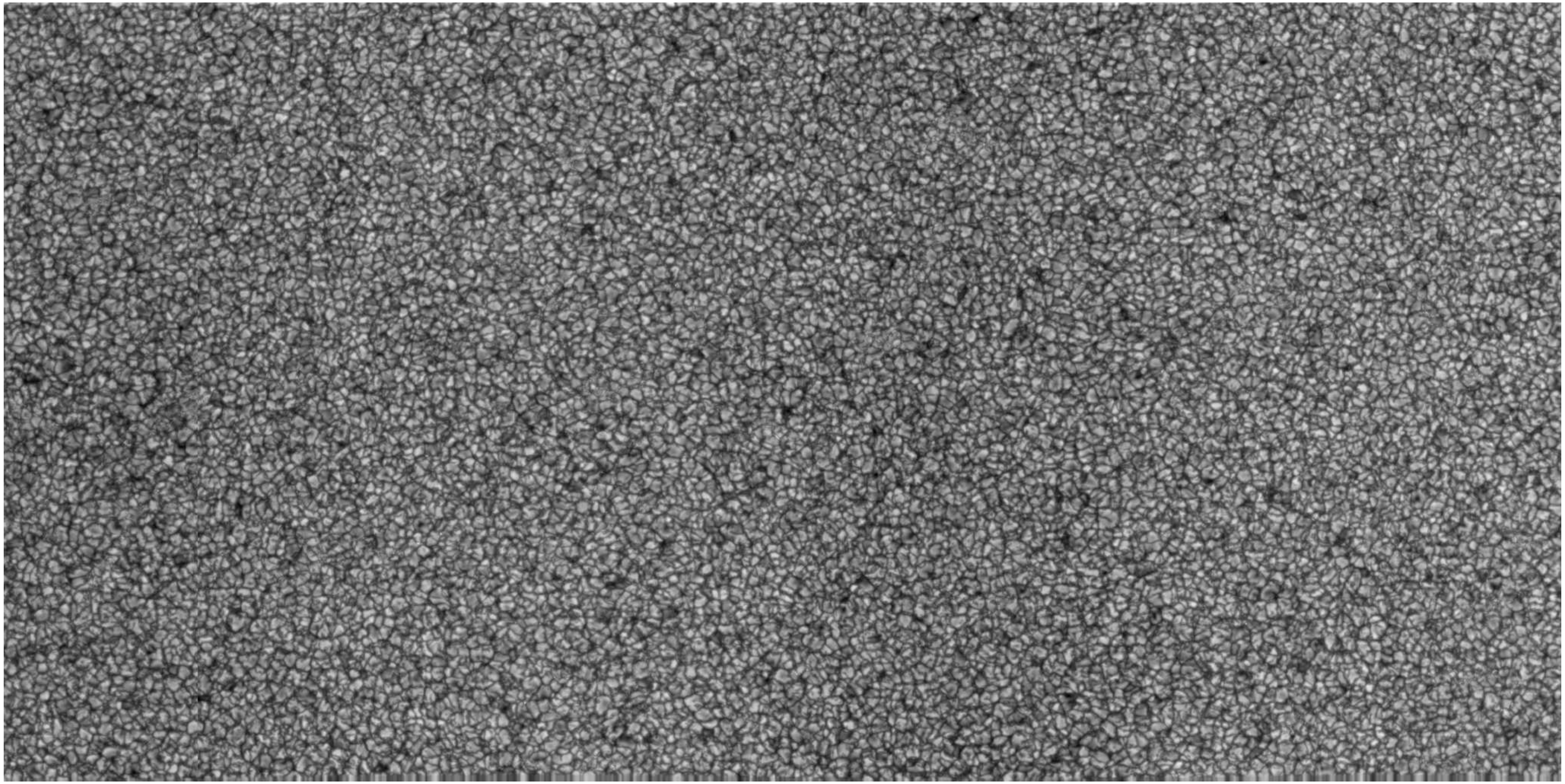

Continuum intensity at 630 nm over a field of view of $302'' \times 162''$. From *Lites et. al. 2008, ApJ 672, 1237*

Case study I: Magnetic fields of the quiet Sun (cont.)

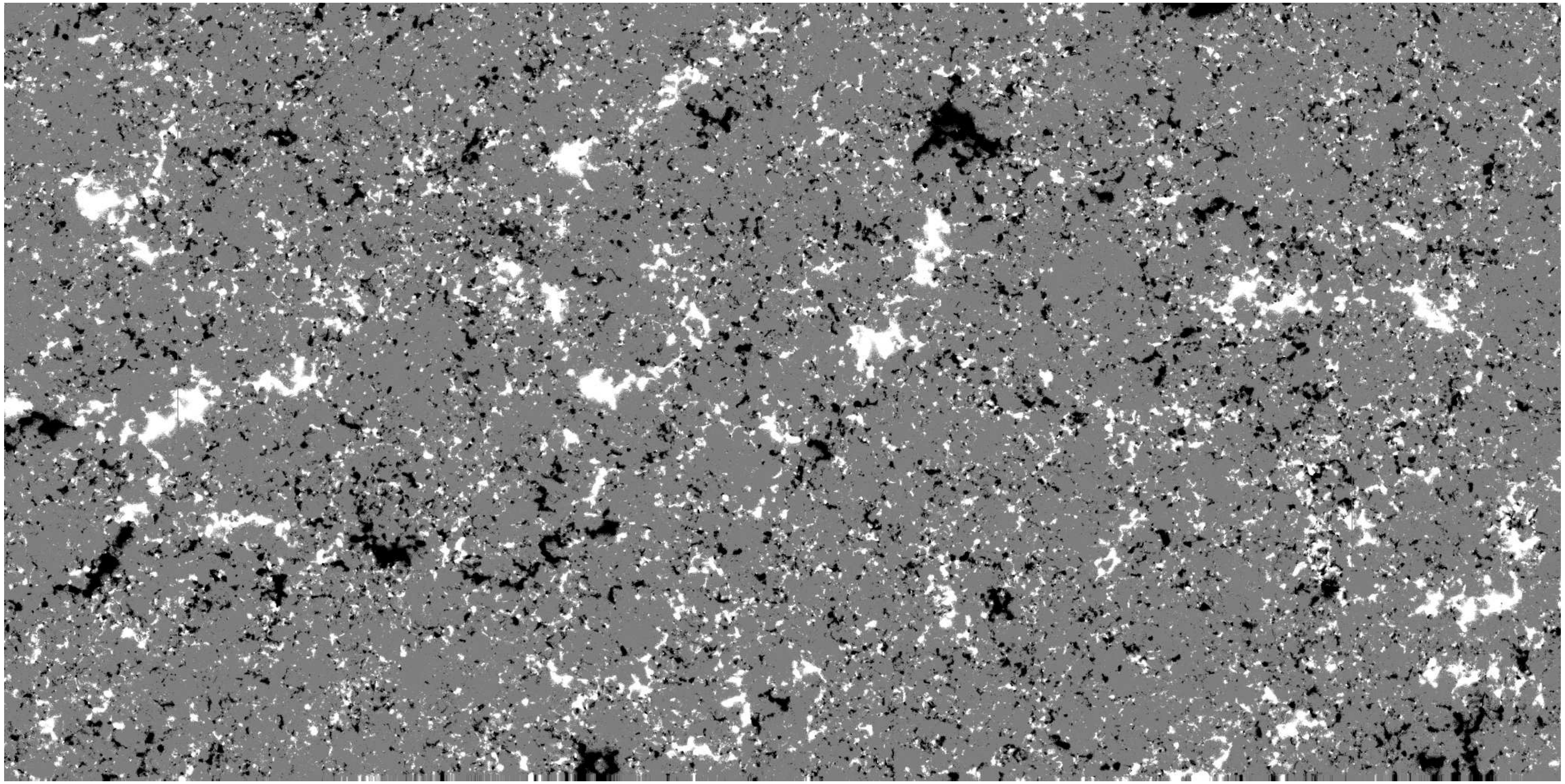

Apparent vertical magnetic flux density, $B^{\rm L}_{\rm app}$, of the quiet Sun over a field of view of $302'' \times 162''$. The grey scale saturates at ± 50 Mx cm^{-2}. 2048 steps to 5 s. $\langle |B^{\rm L}_{\rm app}| \rangle = 11.7$ *Mx cm*$^{-2}$. From *Lites et. al. 2008, ApJ 672, 1237*

Case study I: Magnetic fields of the quiet Sun (cont.)

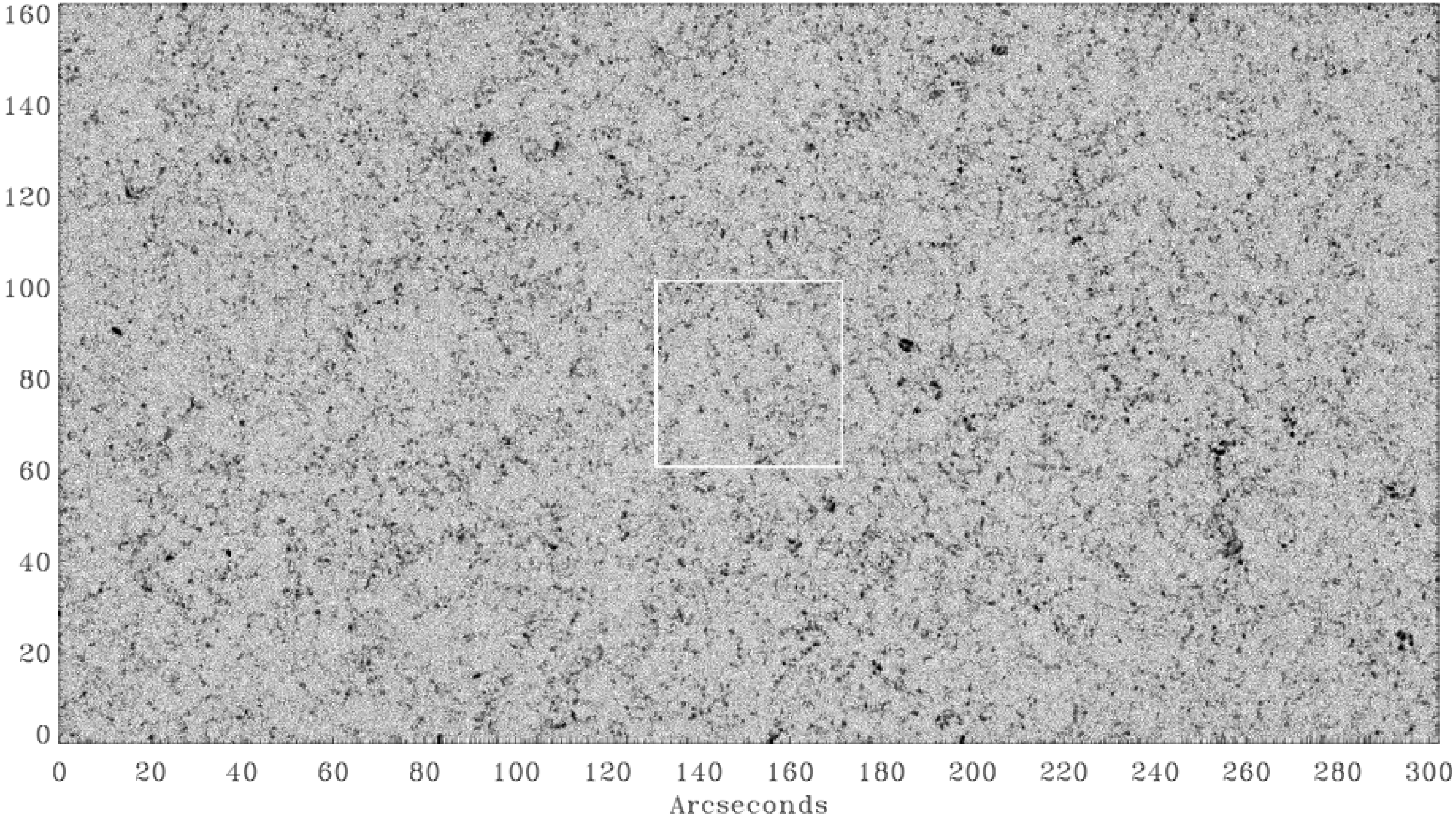

Apparent horizontal magnetic flux density, $B^{\mathrm{T}}_{\mathrm{app}}$, of the quiet Sun over a field of view of $302'' \times 162''$. The grey scale saturates at ± 200 Mx cm^{-2}. 2048 steps to 5 s.

$\langle B^{\mathrm{T}}_{\mathrm{app}} \rangle = 60.0$ *Mx cm*$^{-2}$. From *Lites et. al. 08*

Case study I: Magnetic fields of the quiet Sun (cont.)

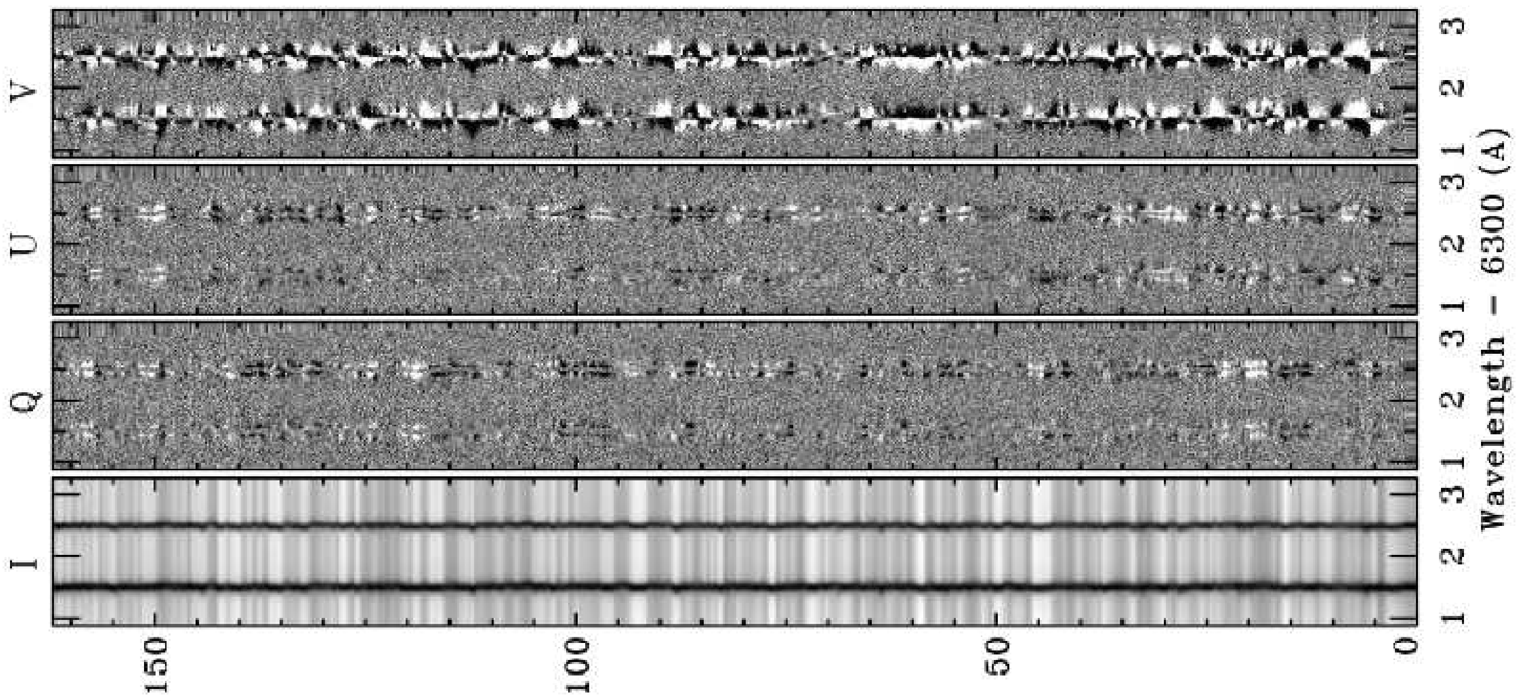

Deep mode *Stokes spectra* with an integration time of 67.2 s and a rms polarization in the continuum of 3×10^{-4}. From a 2-hour time series Lites et al. obtain mean apparent longitudinal and transversal field strengths of $\langle B_{\mathrm{app}}^{\mathrm{L}} \rangle = 11.0$ Mx cm^{-2} and $\langle B_{\mathrm{app}}^{\mathrm{T}} \rangle = 55.3$ Mx cm^{-2}. From *Lites et al. 08*

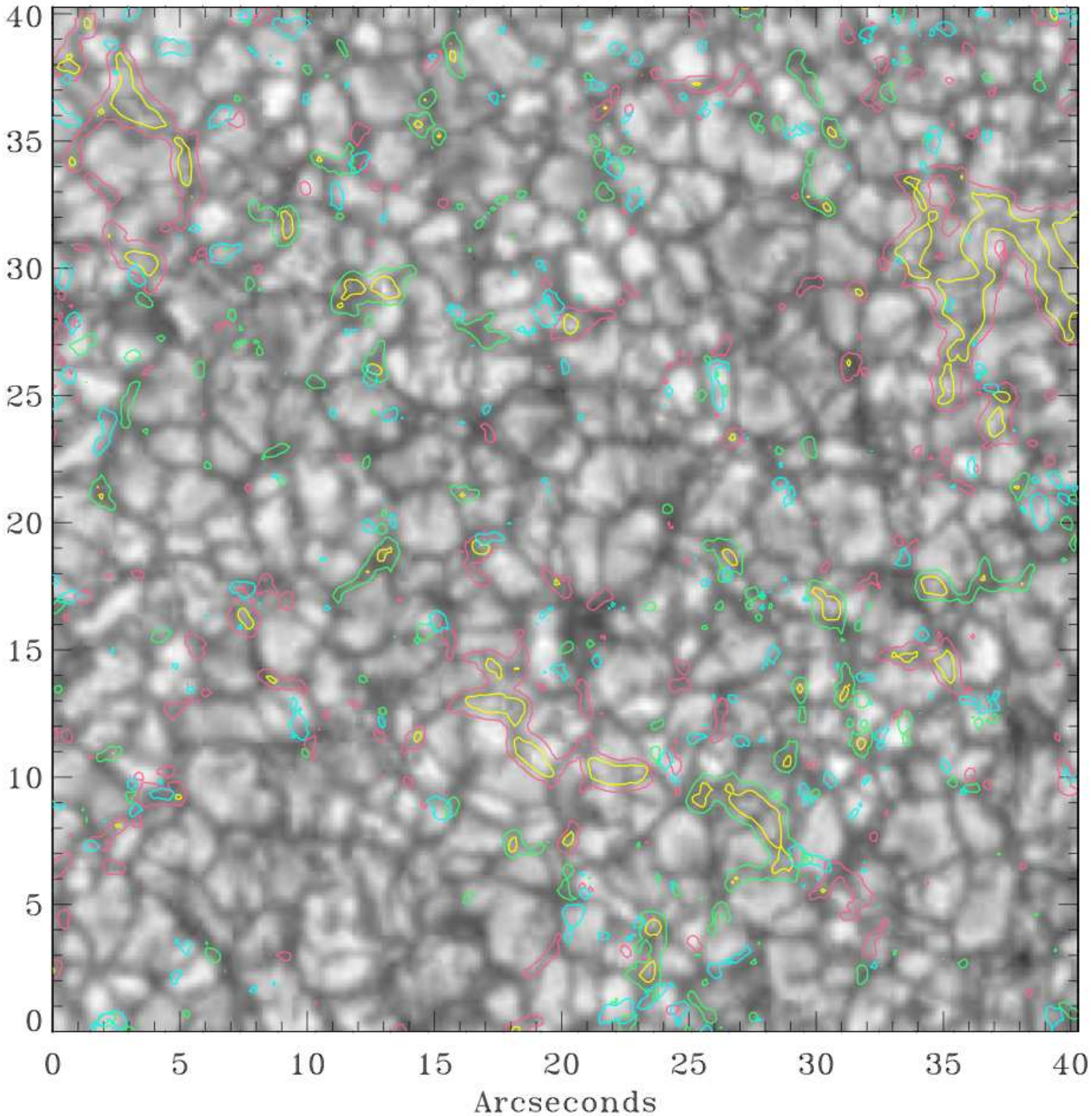

Red and *green*: contours of $B^{\mathrm{L}}_{\mathrm{app}} = 24$ Mx cm^{-2}, respectively positive and negative. *Yellow*: contours of $B^{\mathrm{L}}_{\mathrm{app}} = 100$ Mx cm^{-2}. *Blue* contours correspond to $B^{\mathrm{T}}_{\mathrm{app}} = 122$ Mx cm^{-2}. Horizontal flux preferentially occurs at locations between lanes and granule centers. From *Lites et. al. 08*

Case study I: Magnetic fields of the quiet Sun (cont.)

A predominance of horizontally directed magnetic fields in the quiet Sun was also reported by *Orozco Suárez et al. 07* from *HINODE* measurements and by *Harvey et al. 07* from center-to-limb measurements with GONG and SOLIS.

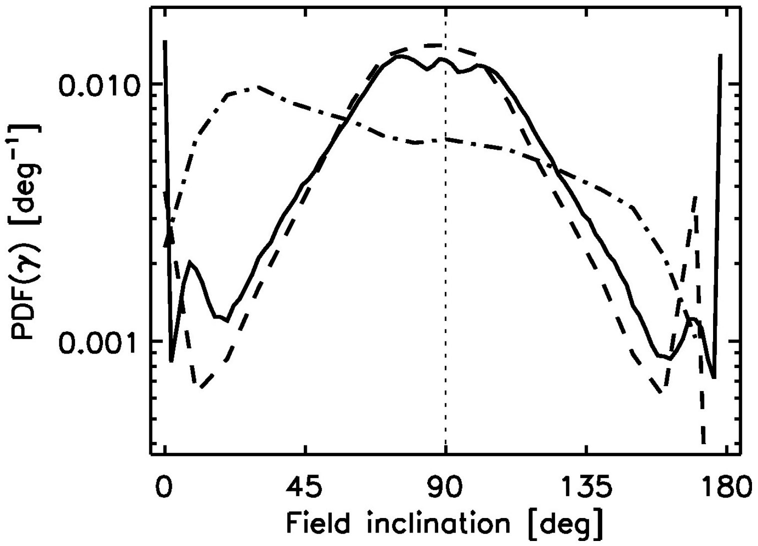

Probability density of the magnetic field inclination in the inter-network. From *Orozco Suárez et al. 07*.

Ishikawa et. al. 08 detected transient horizontal magnetic fields in plage regions with SOT/HINODE

Previously, *Meunier et al. 1998* and *Martinez Pillet et al. 97* reported observations of weak and strong horizontal field in quiet Sun regions.

Questions:

- Do simulations of the surface layers of the Sun intrinsically produce horizontal magnetic fields ?
- If yes, how do they originate ?
- How does the polarimetric signal from simulations compare to measurements ?

Schüssler & Vögler 2008, A&A 481, L5-L8

Steiner, Rezaei, Schaffenberger, and Wedemeyer-Böhm 2008, ApJ 680, L85-L88

Grossmann-Doerth et al. 1998 noted: “we find in all simulations also strong horizontal fields above convective upflows”

§ 17 Numerical simulation of near surface magnetoconvection

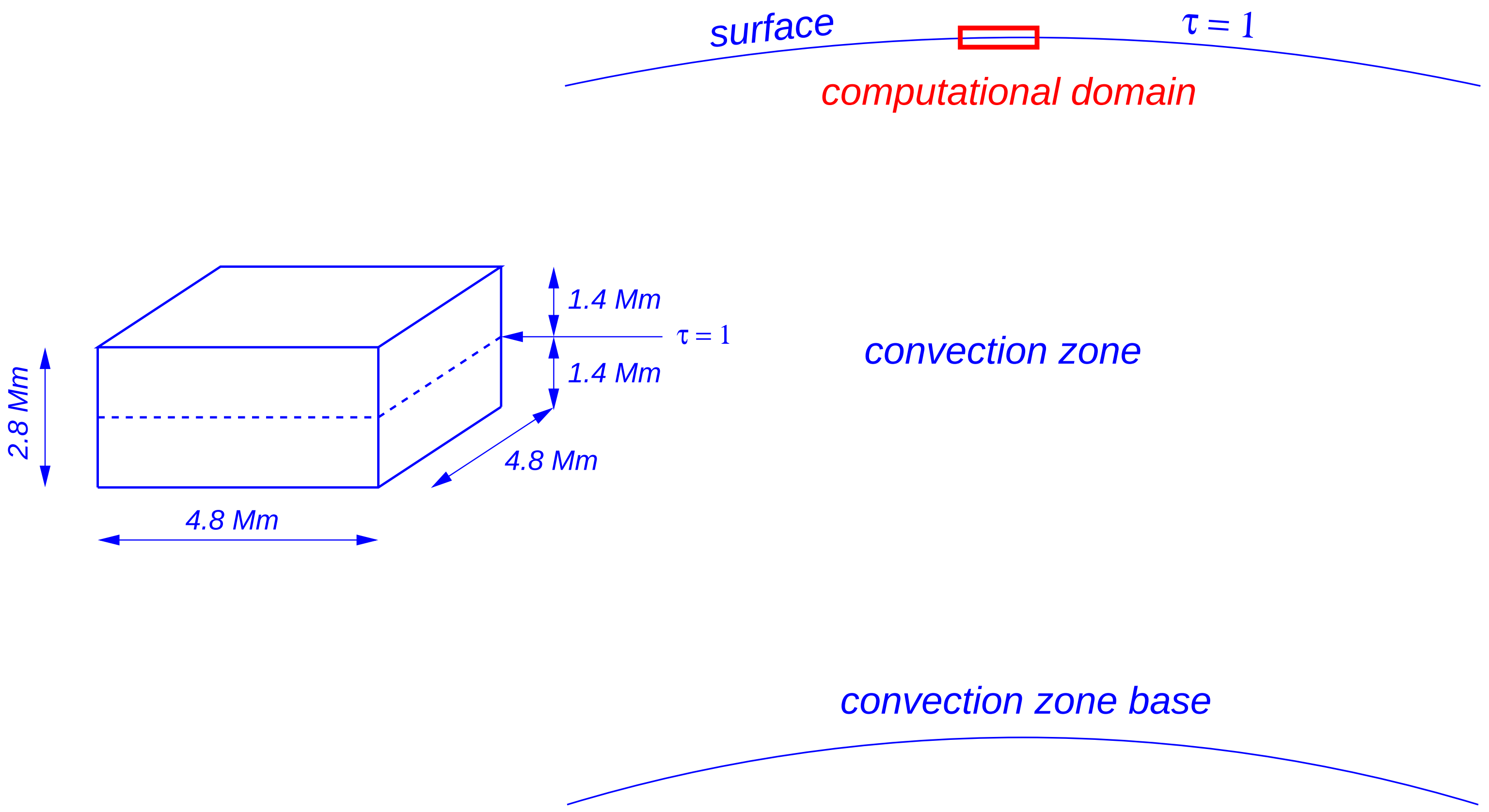

Typical size of a three-dimensional computational box (left) on scale with the convection zone boundaries (right)

Different initial states and boundary conditions for the magnetic field

v10

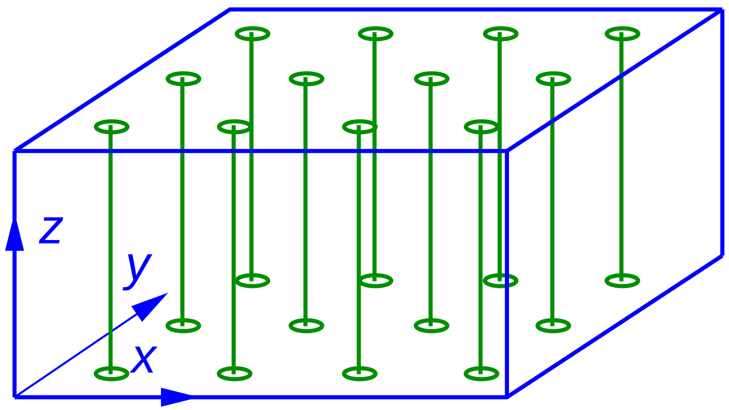

Initial homogeneous, vertical, unipolar **B**-field of 10 G.

$B_{x,y} = 0; \quad \partial B_z / \partial z = 0$

h20

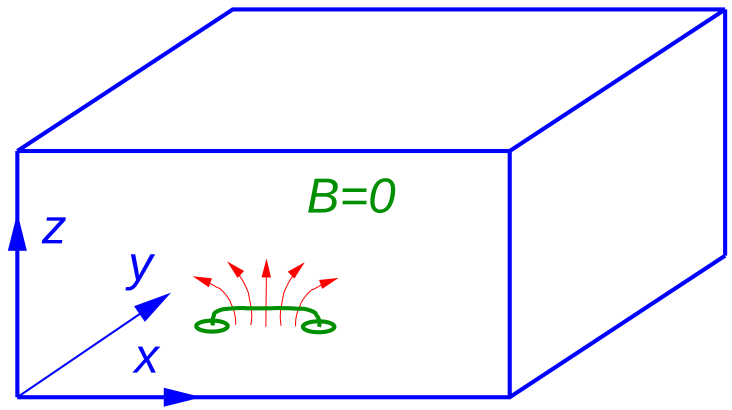

Fluid that enters the simulation domain from below carries horizontal magnetic field of $B_x = 20$ G.

$\partial B_{x,y,z} \partial z = 0$

$\longrightarrow$ more

Numerical simulation of near surface magnetoconvection (cont.)

Vertical cross sections through 3-D simulation domain

v10

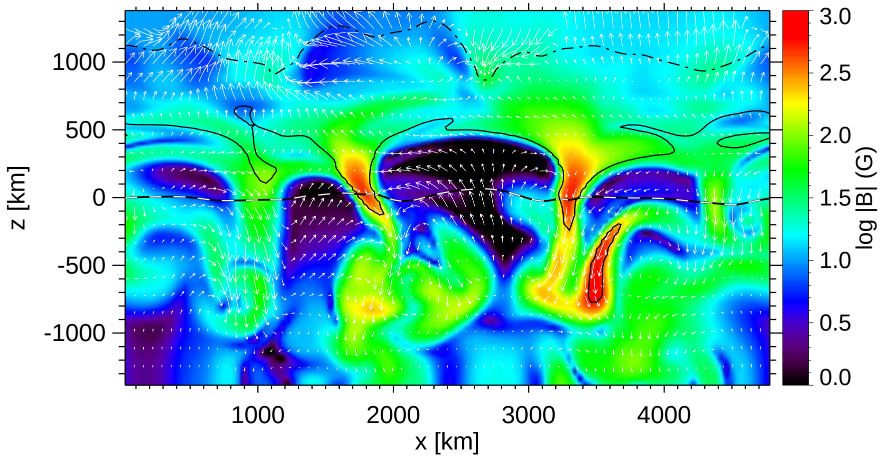

Colors indicate $0 \leq \log |B| \leq 3.0$

h20

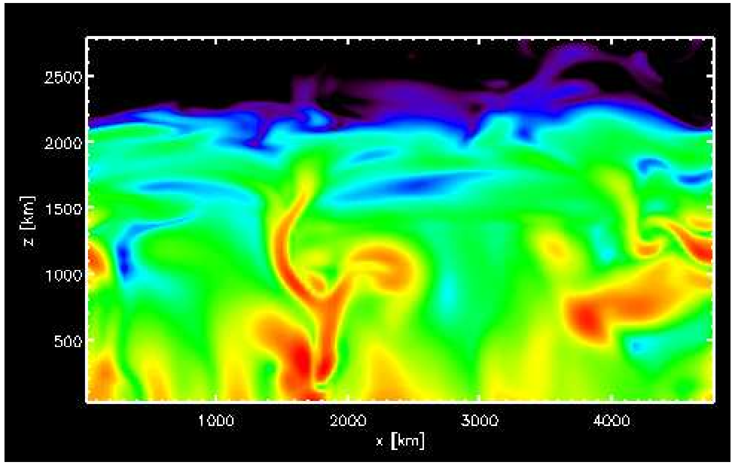

Colors indicate $0.5 \leq \log |B| \leq 2.5$

Numerical simulation of near surface magnetoconvection (cont.)

Horizontally and temporally averaged absolute vertical and horizontal magnetic flux density as a function of height for both runs.

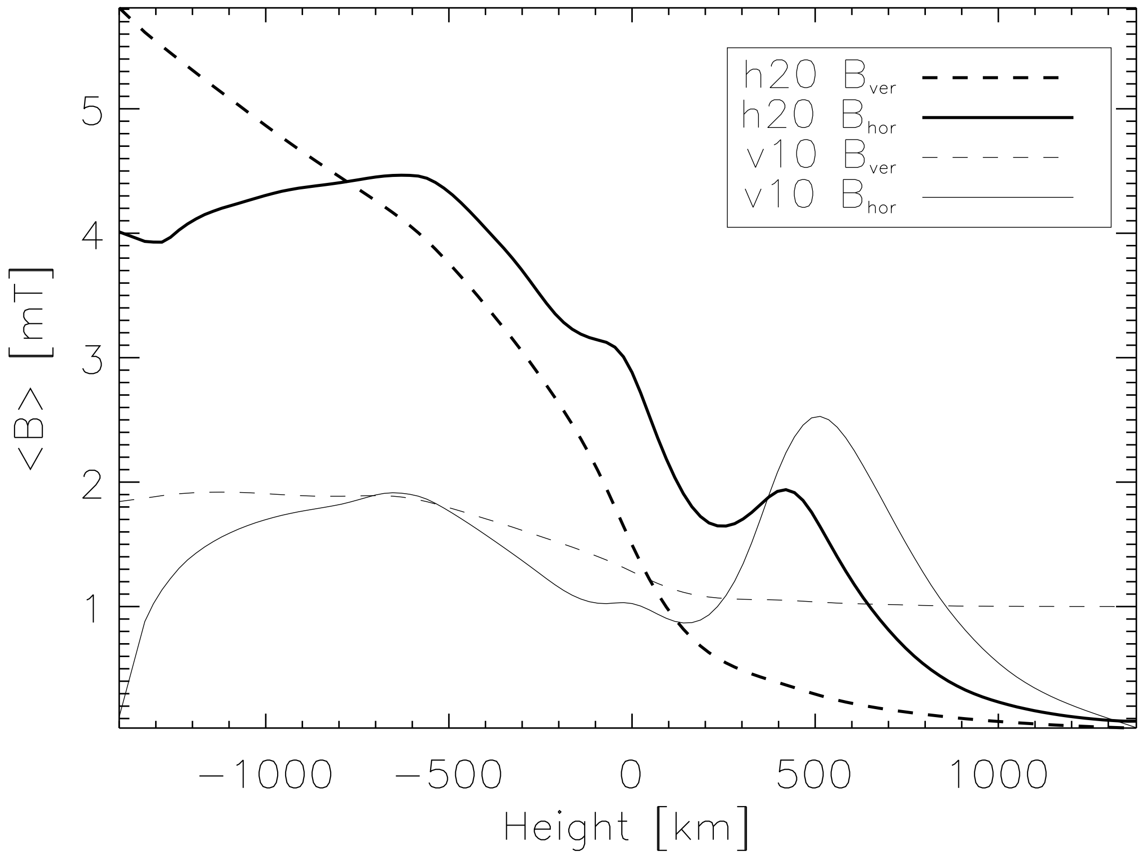

$$\langle B_{\rm hor}\rangle = \langle \sqrt{B_x^2 + B_y^2}\,\rangle$$

run v10:

$$\langle B_{\rm hor}\rangle / \langle |B_{\rm ver}|\rangle (500\,\text{km}) = 2.5$$

run h20:

$$\langle B_{\rm hor}\rangle / \langle |B_{\rm ver}|\rangle (420\,\text{km}) = 5.6$$

Numerical simulation of near surface magnetoconvection (cont.)

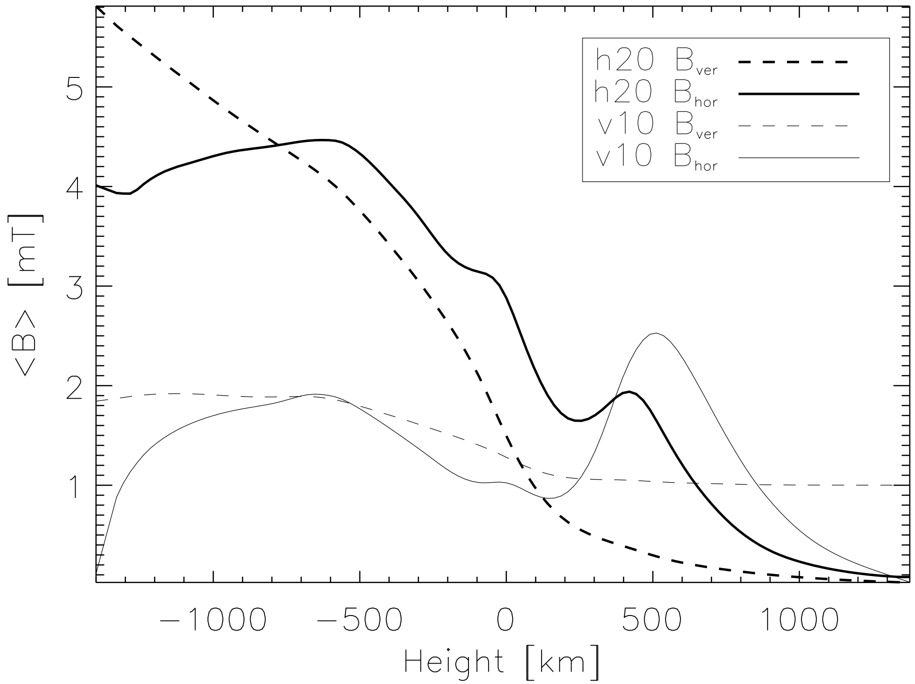

$\langle B_{\rm hor} \rangle$ (———-) and $\langle B_{\rm ver} \rangle$ (– – – – – –) as a function of height z for run h20 (heavy) and run v10 (thin).

From *Steiner et al. 2008*

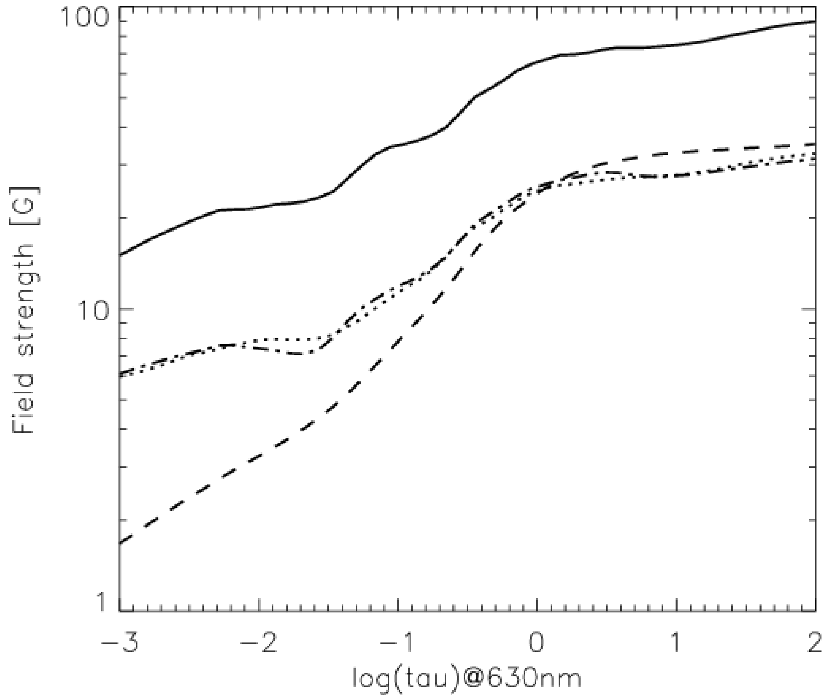

$\langle B_x \rangle$ (— · — · — · —), $\langle B_y \rangle$ (. . . . . .), and $\langle B_{\rm ver} \rangle$ (- - - - -) as a function of $\log \tau_{630\ \rm nm}$.

From *Schüssler & Vögler 2008*

Numerical simulation of near surface magnetoconvection (cont.)

Vertical section through computational domain...

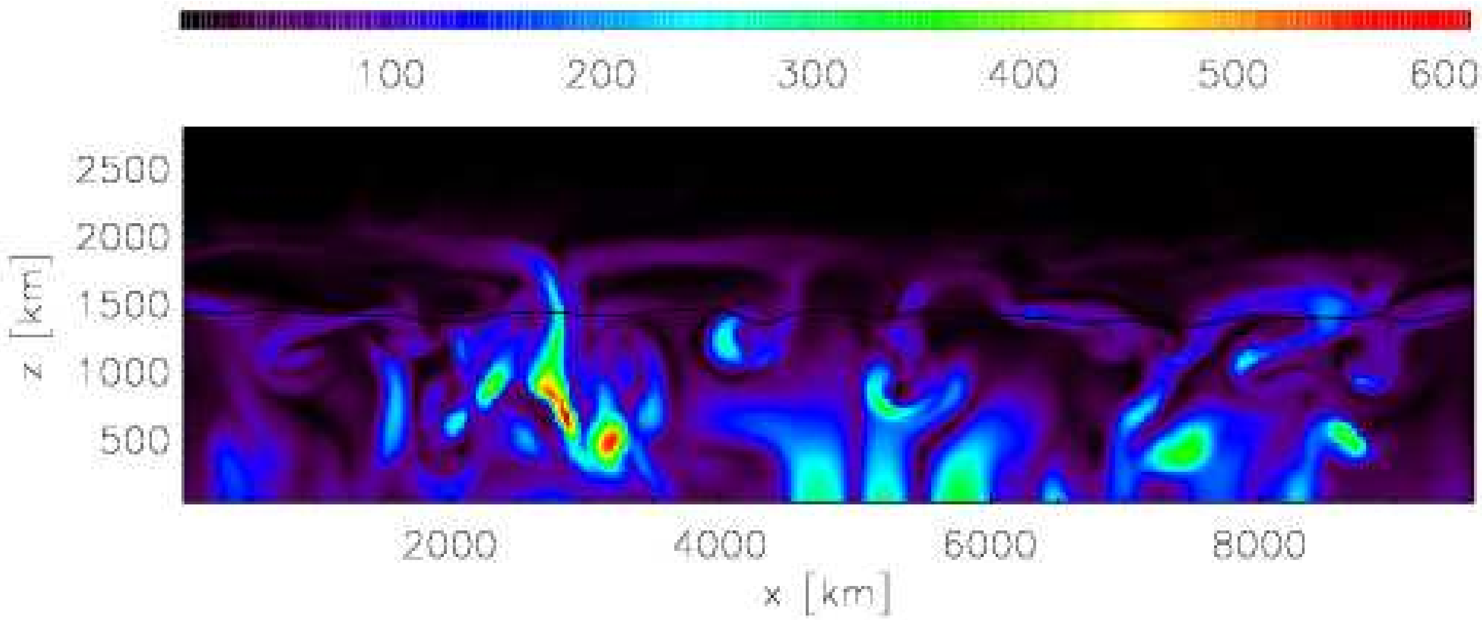

... shows horizontal sheets of enhanced magnetic field strength in the upper photosphere — *the seething magnetic field*. $\longrightarrow$ T movie

Numerical simulation of near surface magnetoconvection (cont.)

Snapshot of $B_{\rm hor}$, $B_{\rm ver}$, and the continuum intensity at 630 nm from *run h20* in the horizontal section of $\langle \tau_{500\,\rm nm} \rangle = 1$.

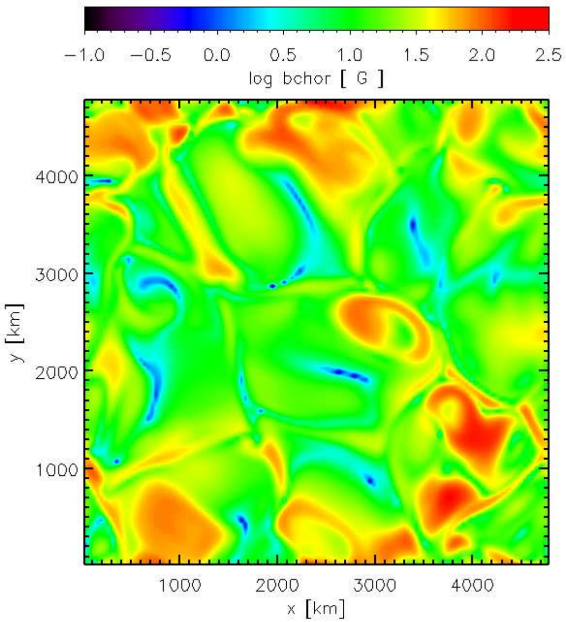

$B_{\rm hor}$

area fraction with

$B_{\rm hor} > 5$ mT $= 17\%$

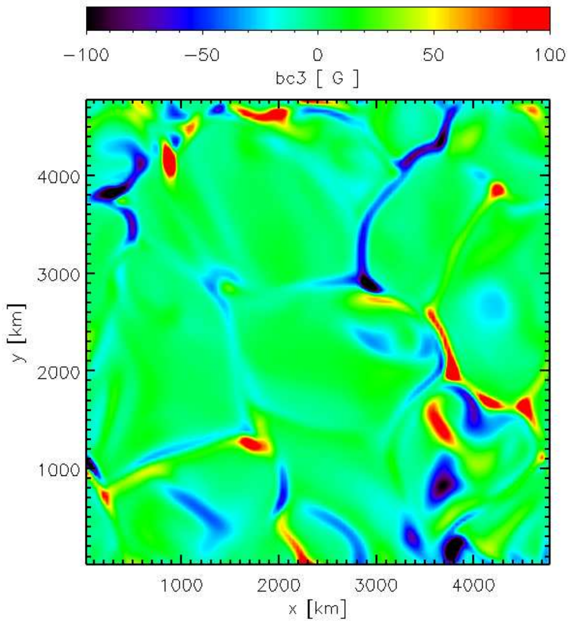

$B_{\rm ver}$

area fraction with

$B_{\rm ver} > 5$ mT $= 2.2\%$

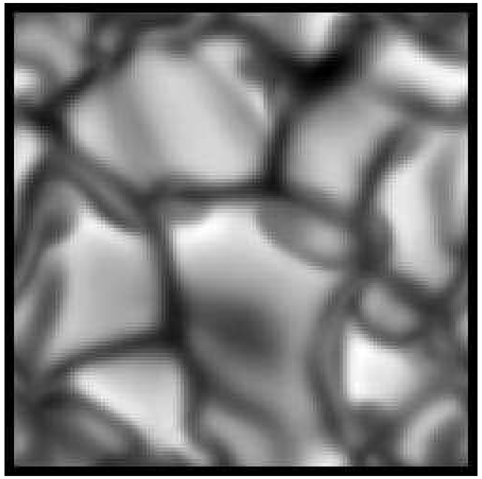

$I_{630\ \rm nm}$

$v_z(\langle \tau_{500\,\rm nm} \rangle = 1)$

Movie

§ 18 Polarimetry

- We synthesized the Stokes profiles of both 630 nm Fe I spectral lines observed by the Hinode SP with a spectral sampling of 2 pm.
- We then compute

$$V_{\rm tot} = \frac{\int_{\lambda_b}^{\lambda_0} V(\lambda){\rm d}\lambda - \int_{\lambda_0}^{\lambda_r} V(\lambda){\rm d}\lambda}{I_c} \ ,$$

and

$$Q_{\rm tot} = \frac{\int Q(\lambda) Q_{\rm mask}(\lambda){\rm d}\lambda}{I_c} \ ,$$

- We subject these quantities to exactly the same calibration procedure for conversion to apparent flux density as was done with the real data by Lites et al. 08.

Polarimetry (cont.)

From the two simulation runs, we synthesized the Stokes profiles of both 630 nm Fe I spectral lines observed by the Hinode SP. Profiles were computed with the radiative transfer code SIR along vertical lines of sight (disk center) with a spectral sampling of 2 pm.

$I_{630\,\mathrm{nm}}$

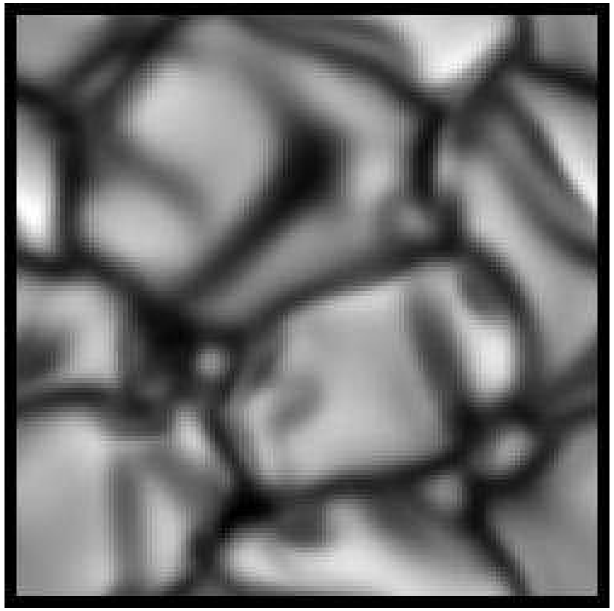

$V_{\mathrm{tot}\;630\,\mathrm{nm}}$

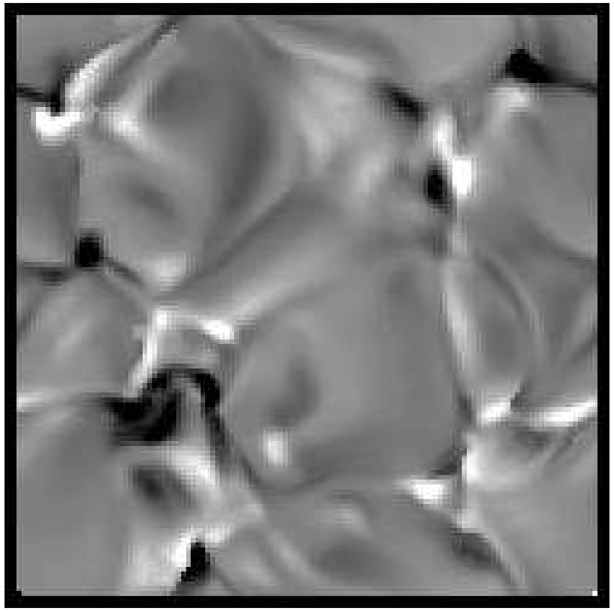

Polarimetry (cont.)

Synthetic continuum intensity ant 630 nm and $V_{\rm tot}$ from a simulation with box size 9.6×9.6 Mm, corresponding to $13'' \times 13''$.

$I_{630\,\rm nm}$

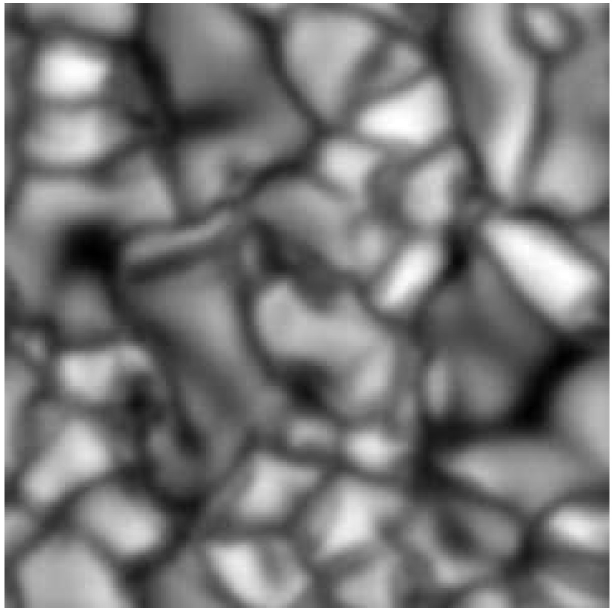

$V_{\rm tot\,630\,nm}$

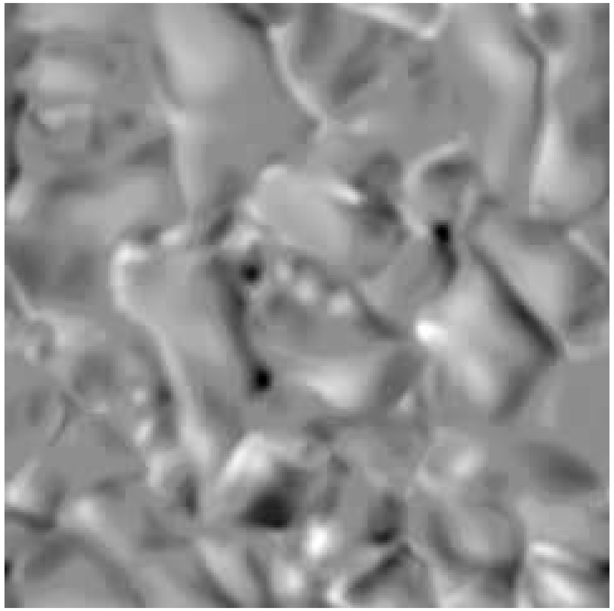

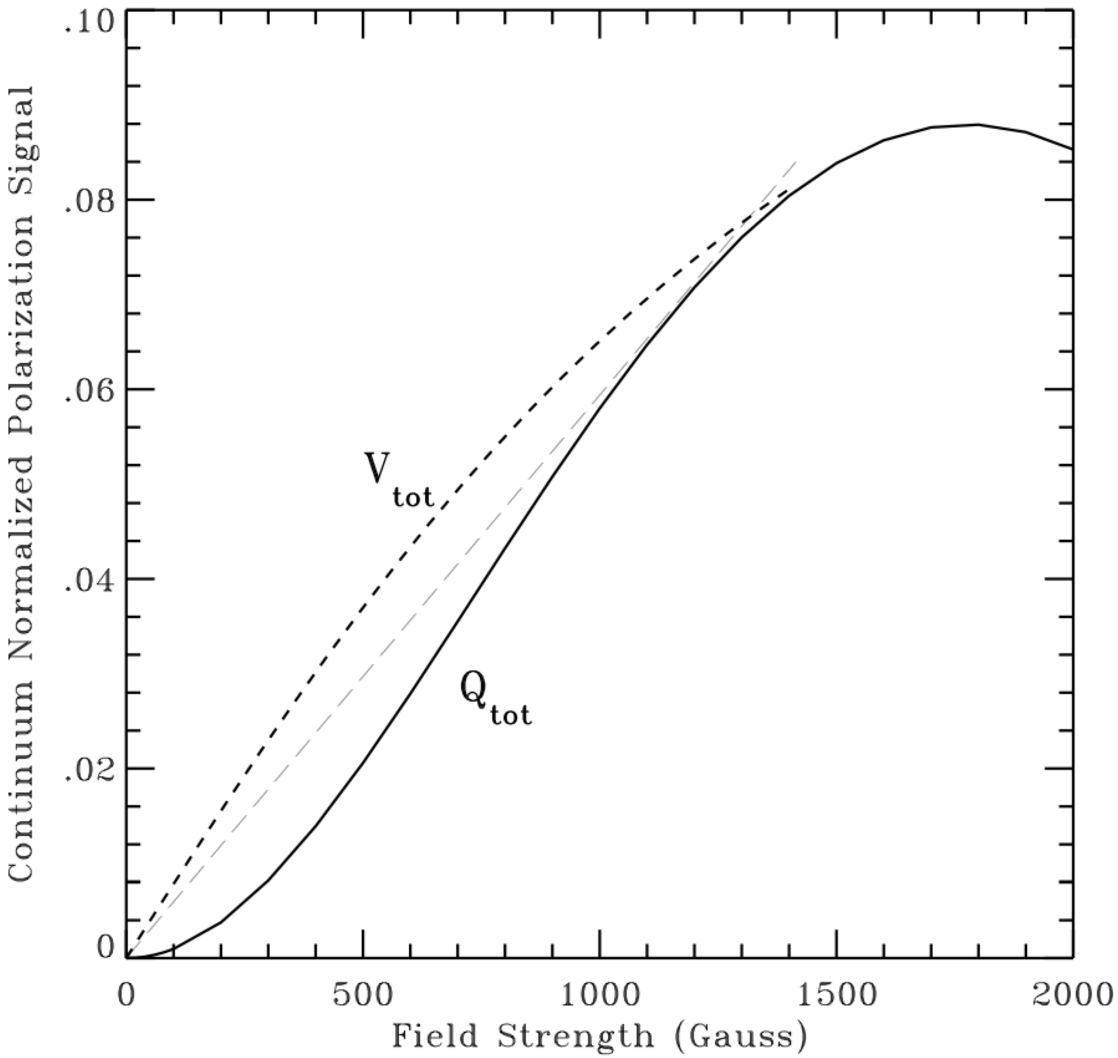

Calibration curve from Lites et al. 07 derived from a Milne-Eddington atmosphere with a homogeneous horizontal magnetic field for $Q_{\rm tot}$ and a magnetic field inclined by 45° for $V_{\rm tot}$.

Polarimetry (cont.)

Lites et al. (2007) found from the deep mode series

$$\frac{\langle B^{\rm T}_{\rm app}\rangle}{\langle B^{\rm L}_{\rm app}\rangle} = \frac{55.3\,\mathsf{Mx\,cm}^{-2}}{11.0\,\mathsf{Mx\,cm}^{-2}} \approx 5\ .$$

From the synthesized Stokes profiles and application of the SOT-PSF we find

$$\frac{\langle B^{\rm T}_{\rm app}\rangle}{\langle B^{\rm L}_{\rm app}\rangle} = \begin{cases} 10.4\,\mathsf{G}/6.6\,\mathsf{G} & = 1.6 \quad \text{for run } \textit{v10} \\ 21.5\,\mathsf{G}/5.0\,\mathsf{G} & = 4.3 \quad \text{for run } \textit{h20} \end{cases} .$$

---

without the PSF we got

$$\frac{\langle B^{\rm T}_{\rm app}\rangle}{\langle B^{\rm L}_{\rm app}\rangle} = \begin{cases} 11.5\,\mathsf{G}/7.5\,\mathsf{G} & = 1.5 \quad \text{for run } \textit{v10} \\ 24.8\,\mathsf{G}/8.8\,\mathsf{G} & = 2.8 \quad \text{for run } \textit{h20} \end{cases} .$$

Polarimetry (cont.)

The vertical field component is more subject to apparent flux cancellation than the horizontal component, because ....

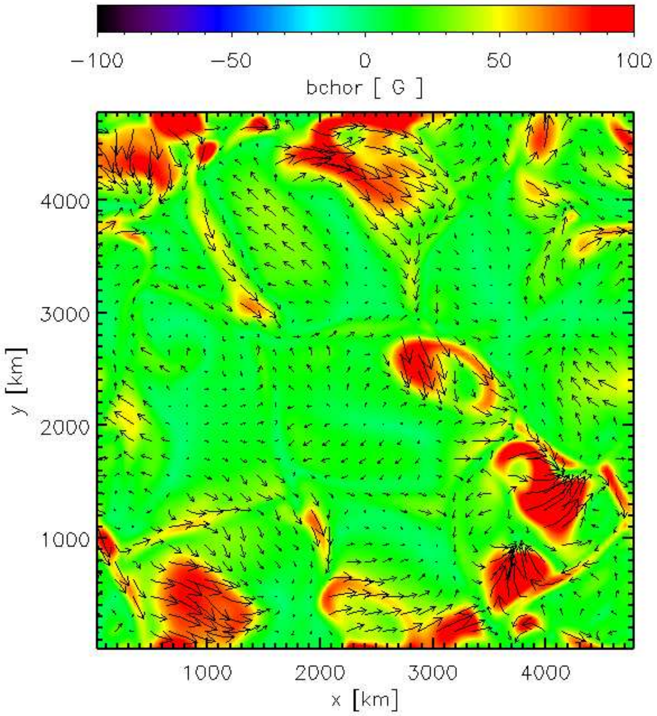

$B_{\rm hor}$

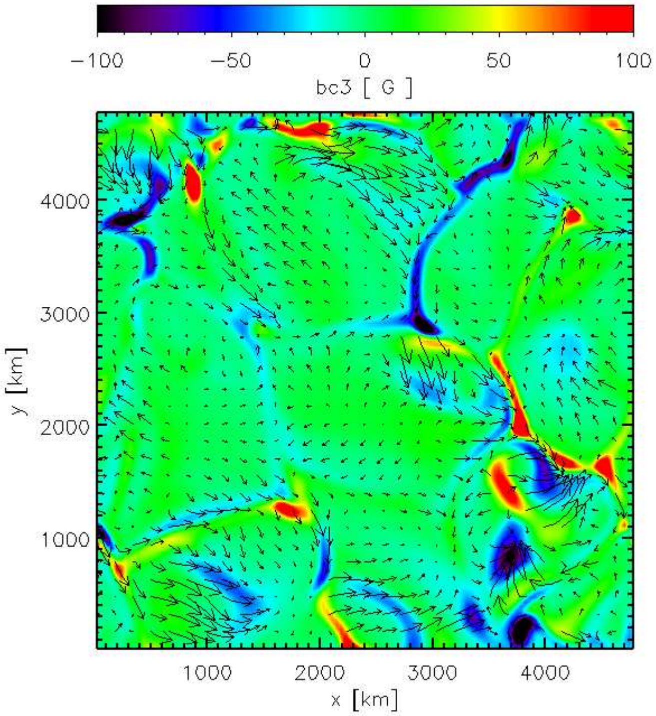

$B_{\rm ver}$

..... the vertical field component has smaller scales and higher intermittency than the horizontal component.

Polarimetry (cont.)

Probability density functions of the magnetic field inclination from *observations of Orozco Suárez et al. (2007)* and simulations

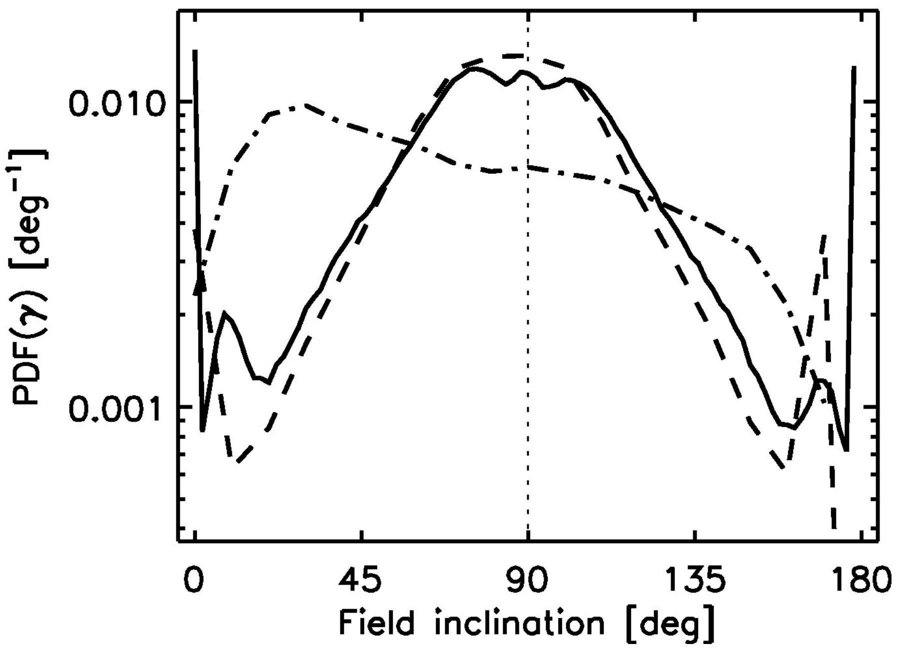

Solid and dashed PDFs represent all pixels in the FOV and the IN regions, respectively. Dot-dashed curve shows PDFs from magnetoconvection *simulations* with a mean flux density of 10 Mx cm^{-2} from *Vögler et al. (2005)*.

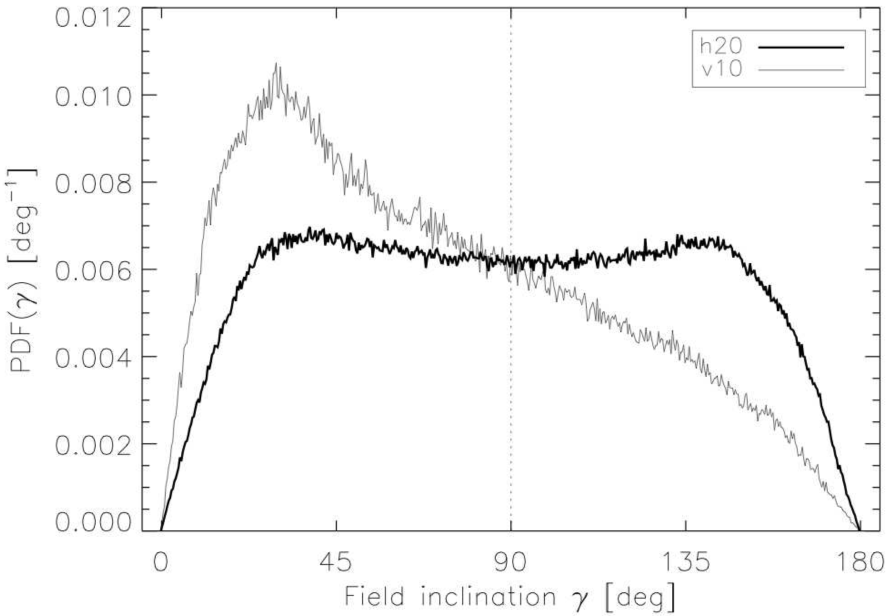

PDF of inclination angle for *simulation* runs h20 and v10 of *Steiner et al. (2008)*.

Center-to-limb variation

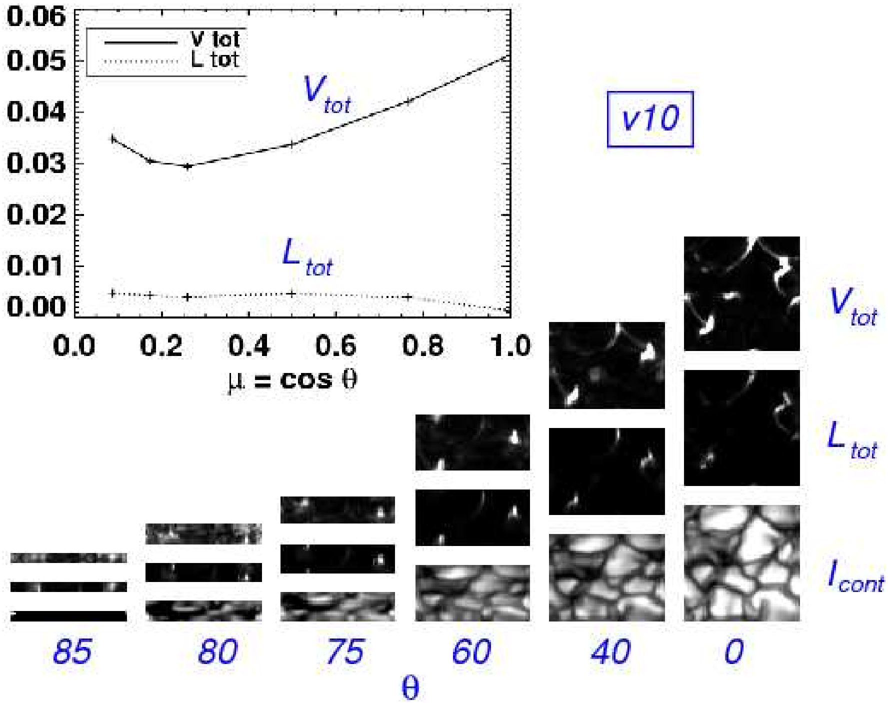

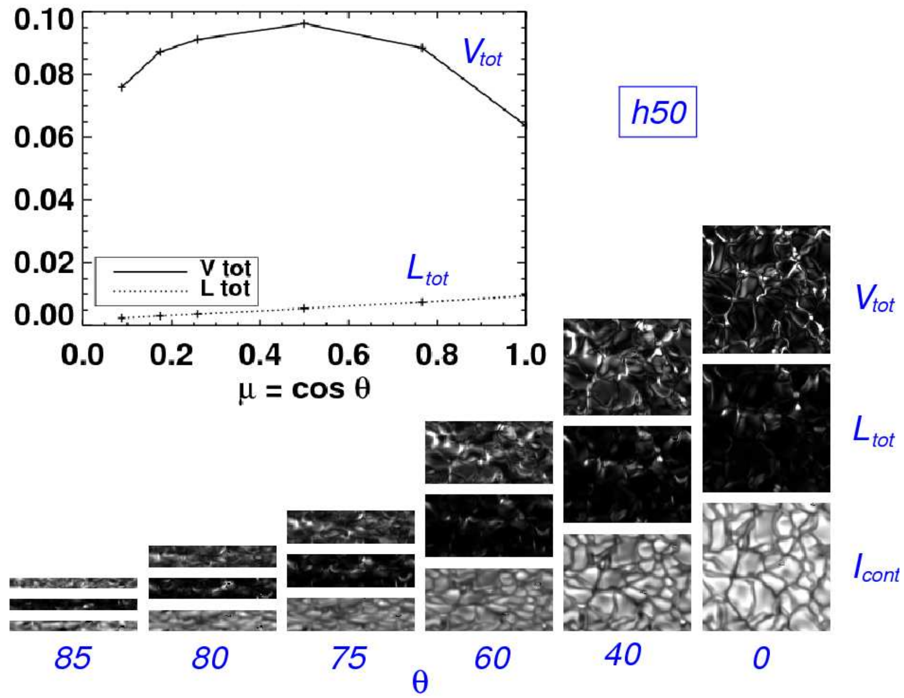

Vertical field dominates in the low photosphere

Horizontal field dominates in the upper photosphere

Horizontal field dominates throughout the photosphere

§ 19 Horizontal magnetic fields: Discussion

The horizontal field can be considered a consequence of the *flux expulsion process* (Weiss, 1966; Galloway & Weiss, 1981): in the same way as magnetic flux is expelled from the granular interior to the intergranular lanes, it also gets pushed to the middle and upper photosphere by overshooting convection, where it tends to form a layer of horizontal field.

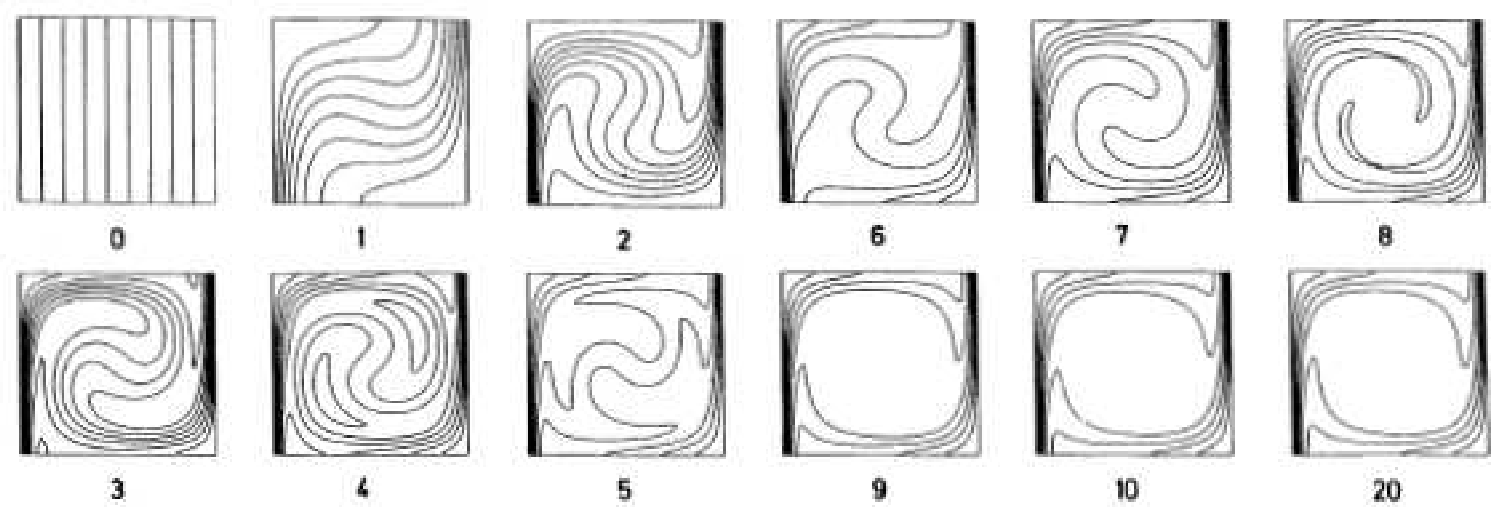

From *Galloway & Weiss, 1981*

Horizontal magnetic fields: Discussion (cont.)

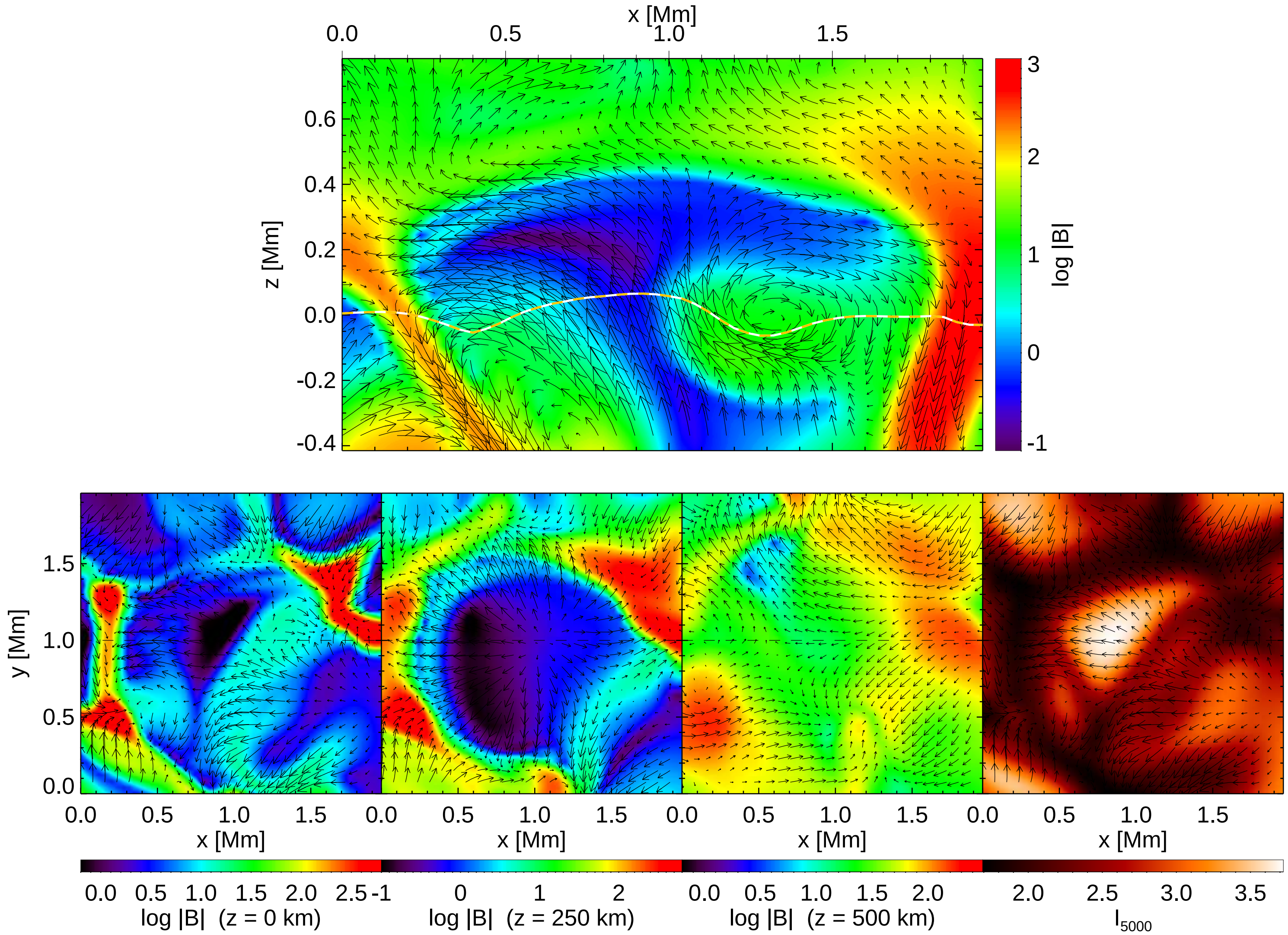

Flux expulsion in a close-up from a MHD simulation by *Schaffenberger et al. (2005)*

Horizontal magnetic fields: Discussion (cont.)

The dominance of the horizontal field “results from the intermittent nature of the dynamo field with polarity mixing on small scales in the surface layers”.

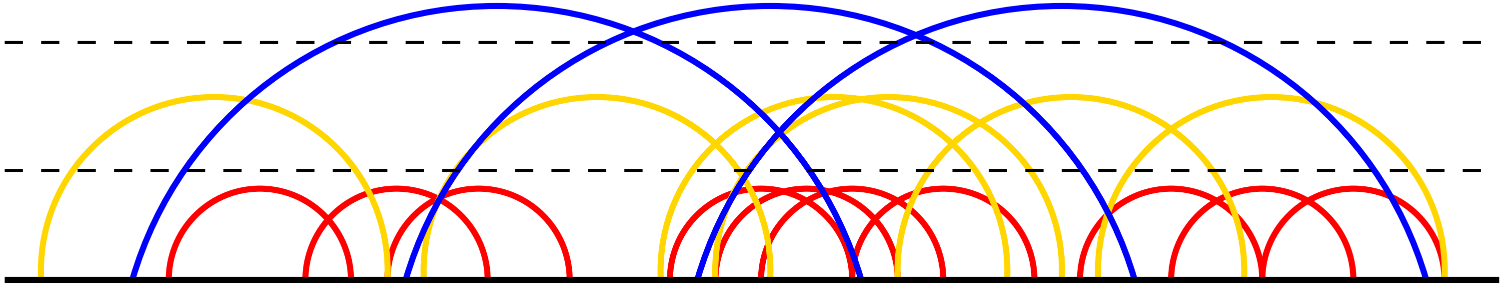

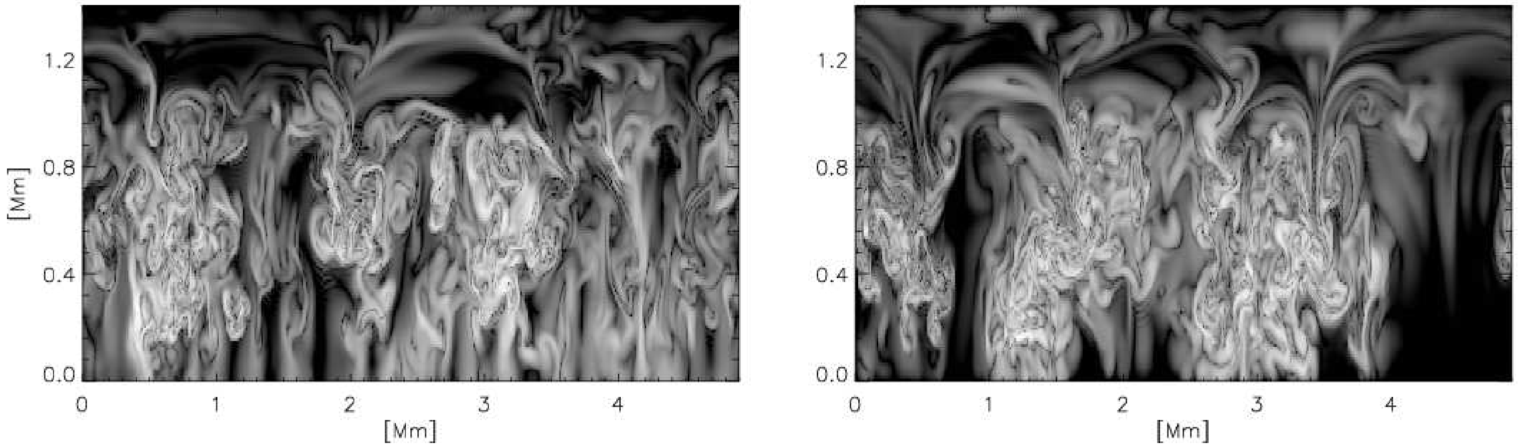

From *Schüssler & Vögler 2008*

Detached horizontal field as a consequence of magnetic reconnection

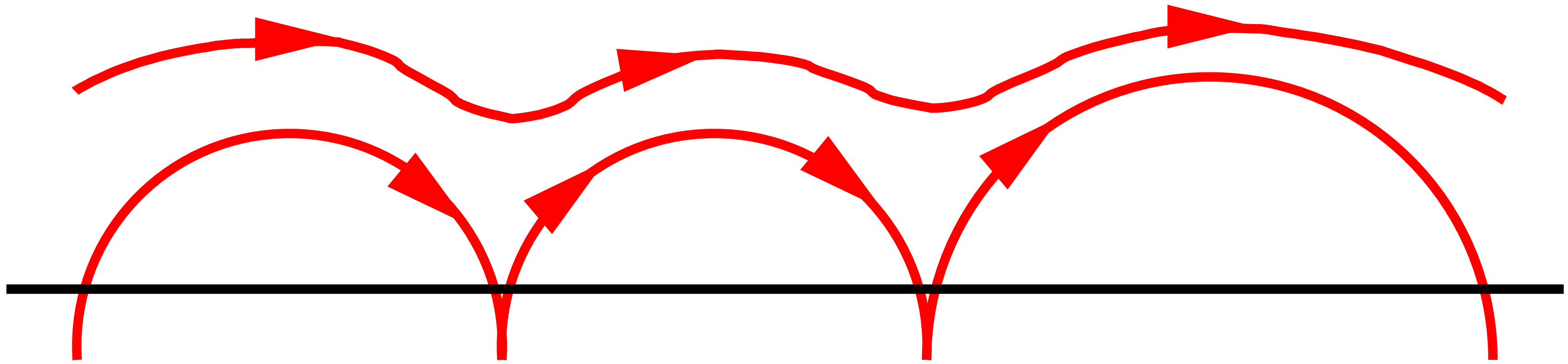

§ 20 Horizontal magnetic fields: Poynting flux

Equation for the total energy:

$$\frac{\partial e}{\partial t} + \nabla\left[(h + \frac{1}{2}v^2)\rho\mathbf{v} + \mathbf{S}\right] - \mathbf{g}\cdot\mathbf{v} = 0\ ,$$

where

$$e = \rho\epsilon + \frac{1}{2}\rho v^2 + \frac{B^2}{2\mu}\ , \qquad h = \epsilon + \frac{p}{\rho}\ ,$$

and

$$\mathbf{S} = \frac{1}{4\pi}(\mathbf{B}\times(\mathbf{v}\times\mathbf{B}))$$

Magnetic energy equation:

$$\frac{\partial}{\partial t}\left(\frac{B^2}{8\pi}\right) = -\nabla\cdot\ \underbrace{(\mathbf{E}\times\mathbf{B})}_{\text{Poynting flux}}\ -\underbrace{\mathbf{u}\cdot(\mathbf{j}\times\mathbf{B})}_{\text{Lorentz work}} - Q_{\mathrm{res}}$$

Horizontal magnetic fields: Poynting flux (cont.)

Vertically directed Poynting flux, $\langle S_z \rangle$, $\langle B_{\rm hor} \rangle$, and $\langle |B_z| \rangle$ as a function of time and height in the atmosphere.

$$\mathbf{S} = \frac{1}{4\pi}(\mathbf{B} \times (\mathbf{v} \times \mathbf{B}))$$

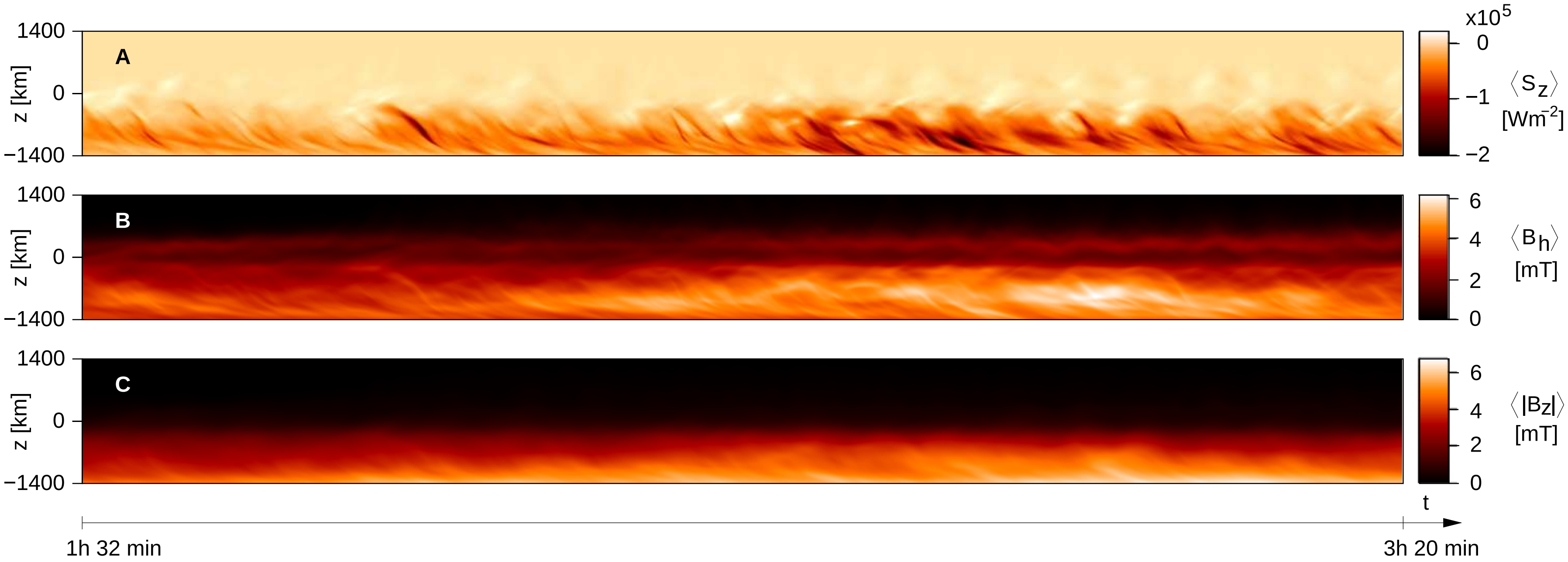

From Steiner, Rezaei, Schaffenberger, & Wedemeyer-Böhm, 2008, ApJ 680, L85-L88

The surface of optical depth unity is a separatrix for the vertically directed Poynting flux.

Horizontal magnetic fields: Poynting flux (cont.)

Vertically directed Poynting flux, $\langle S_z \rangle$, as a function of height in the atmosphere.

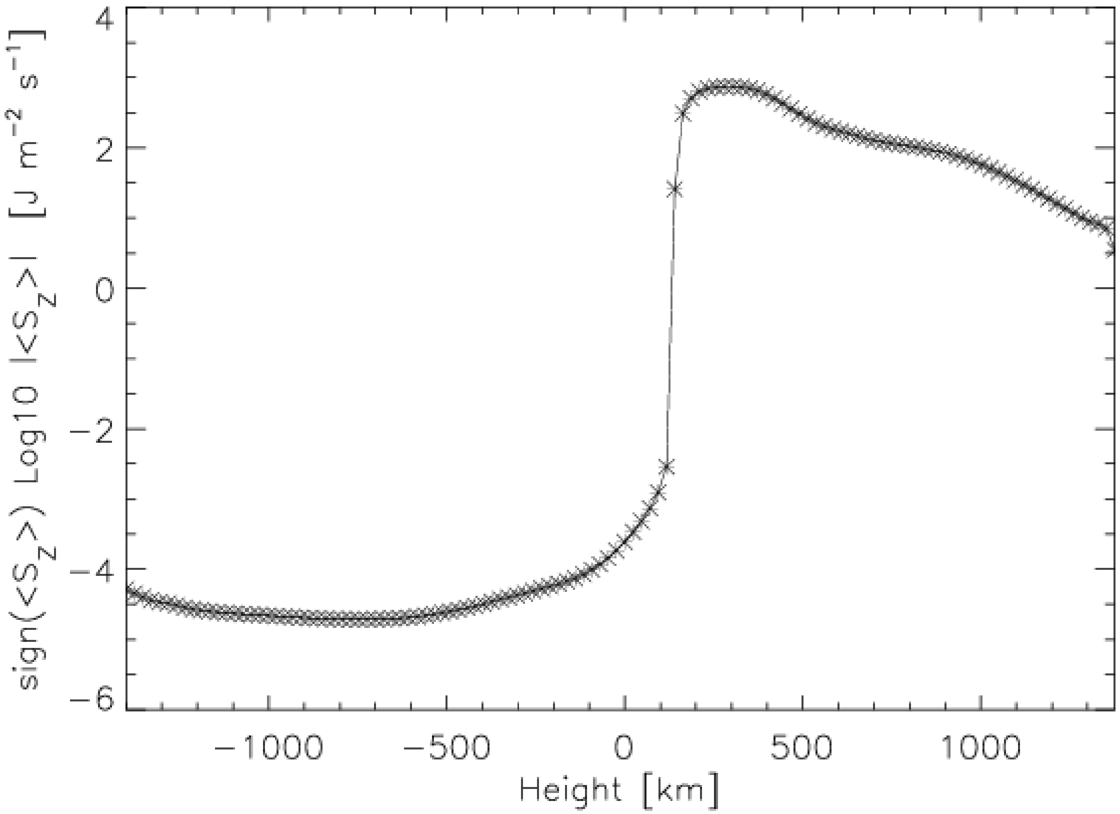

The temporal average of $\langle S_z \rangle$ is maximal 7.4×10^2 Wm^{-2} (at 200 km) and minimal -5.2×10^4 Wm^{-2} (at -800 km). For comparison: the chromospheric radiative energy loss is about 4.3×10^3 Wm^{-2}.

Horizontal magnetic fields: Poynting flux (cont.)

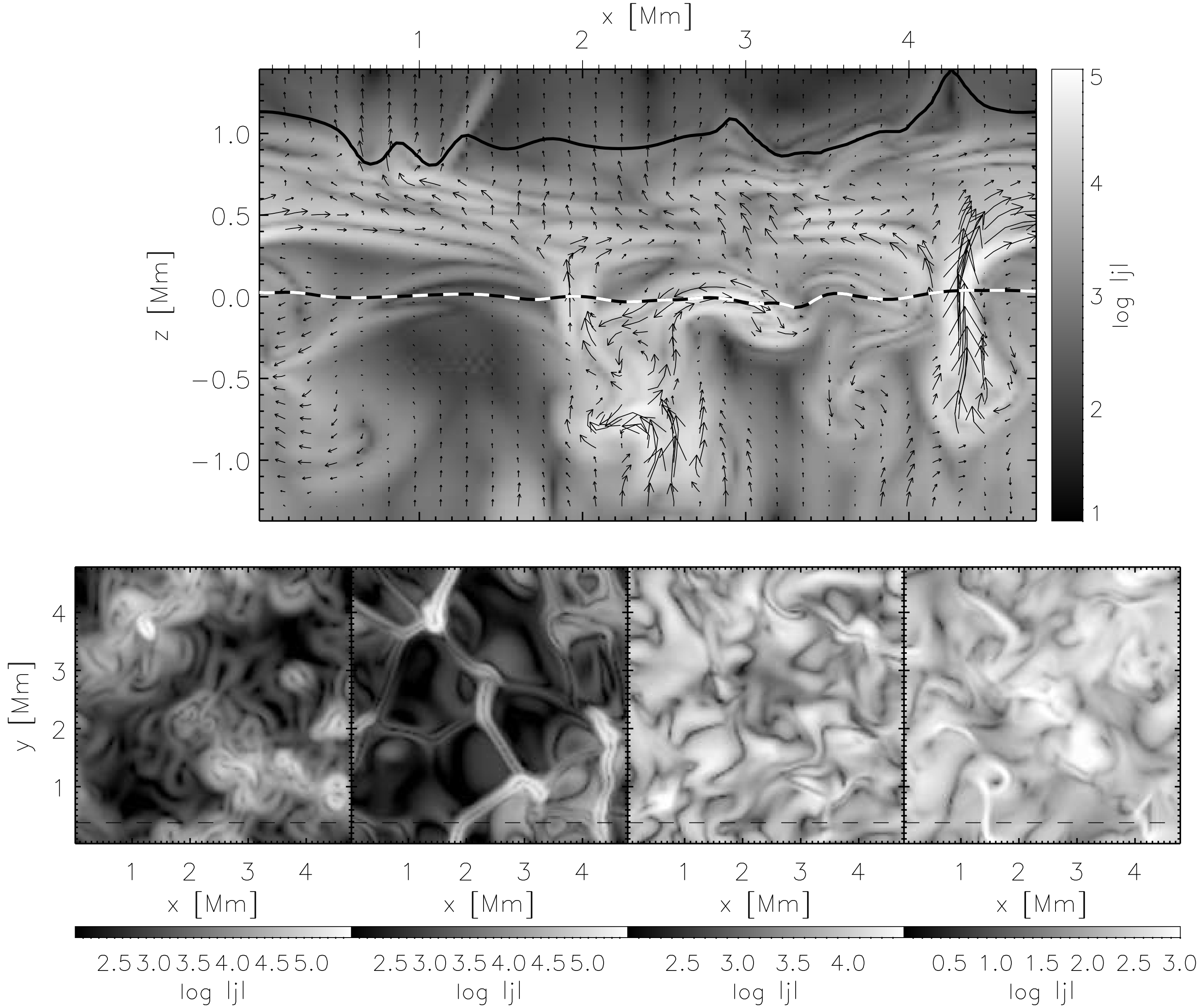

Logarithmic current density, $\log |j|$, in a vertical cross section (top panel) and in four horizontal cross sections in a depth of 1180 km below, and at heights of 90 km, 610 km, and 1310 km above the average height of optical depth unity from left to right, respectively. The arrows in the top panel indicate the *magnetic field* strength and direction.

From Schaffenberger, Wedemeyer-Böhm, Steiner, and Freytag, 2006, ASP Conf. Ser., Vol. 354, p. 345

Horizontal magnetic fields: Poynting flux (cont.)

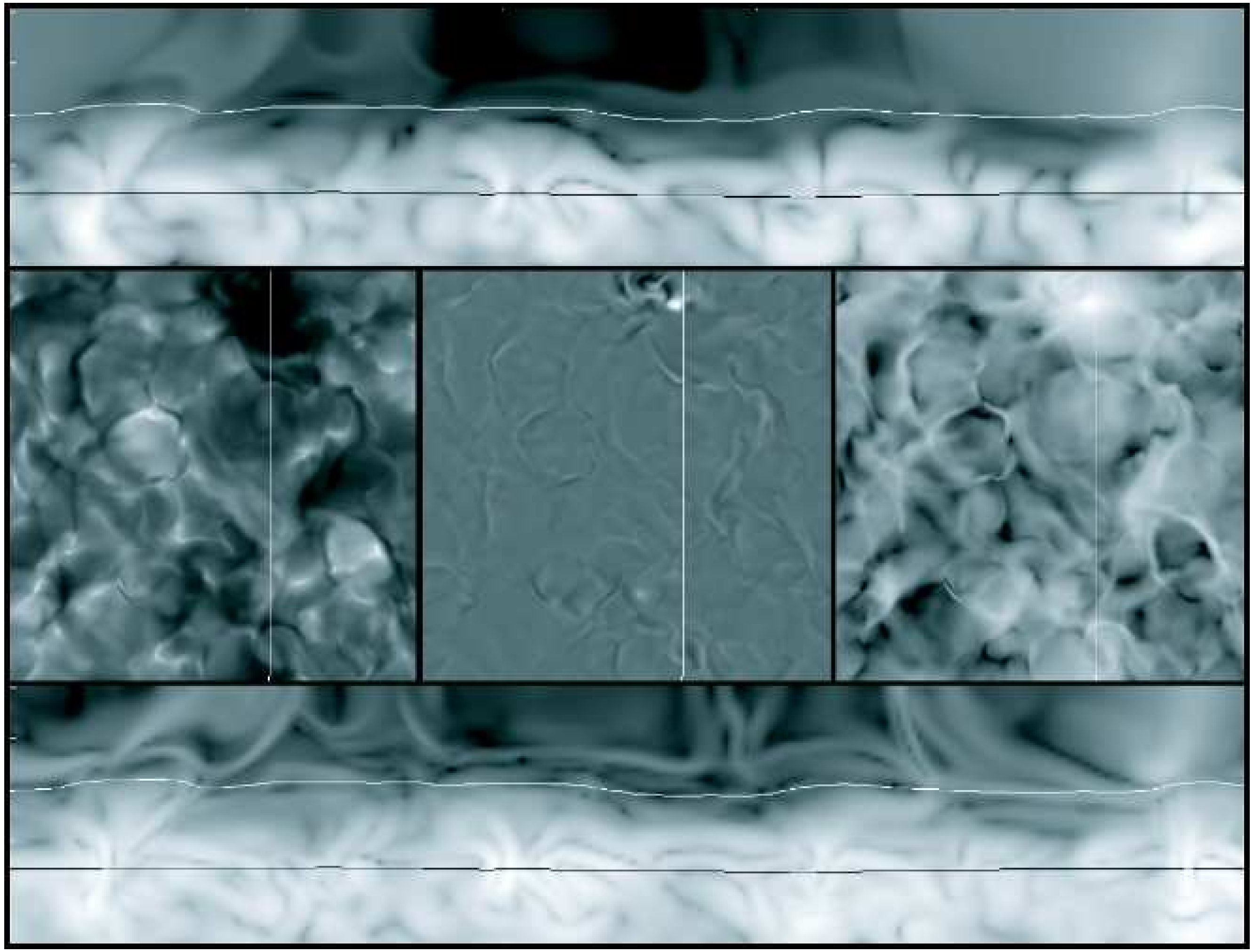

Top: Logarithm of the magnetic field strength. Bottom: Logarithm of the current density.

From *Abbett, ApJ 665, 1469 (2007)*

Horizontal magnetic fields: Poynting flux (cont.)

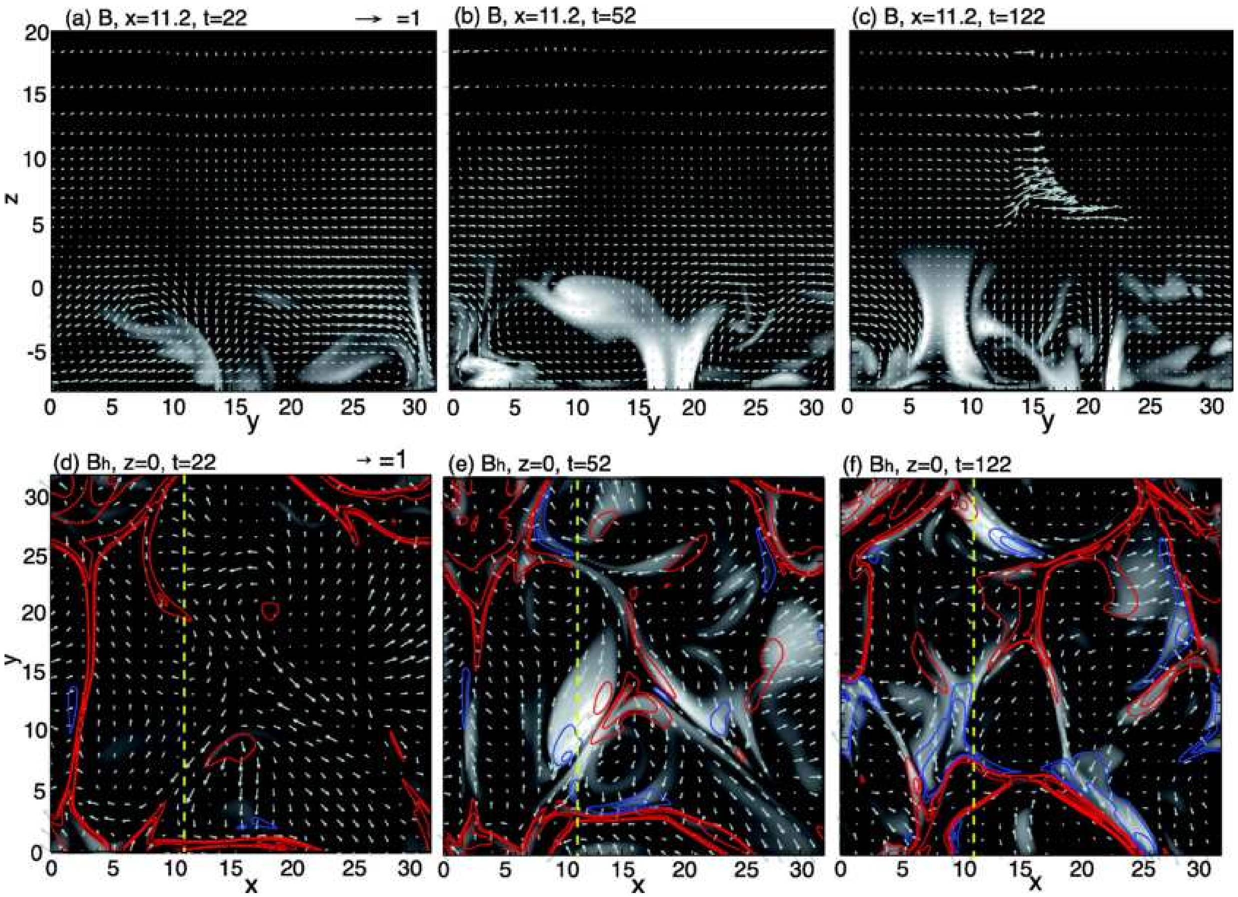

Top: Vertical cross sections of $|B|$ and the velocity vector projected onto the plane.

Bottom: Horizontal cross sections at $z = 0$, showing B_h (gray scale) and B_z (contours), and the magnetic vectors projected onto the plane.

From *Isobe et al., ApJ 679, L57-L60 (2008)*

§ 21 *Case study II:* Structure of internetwork magnetic elements

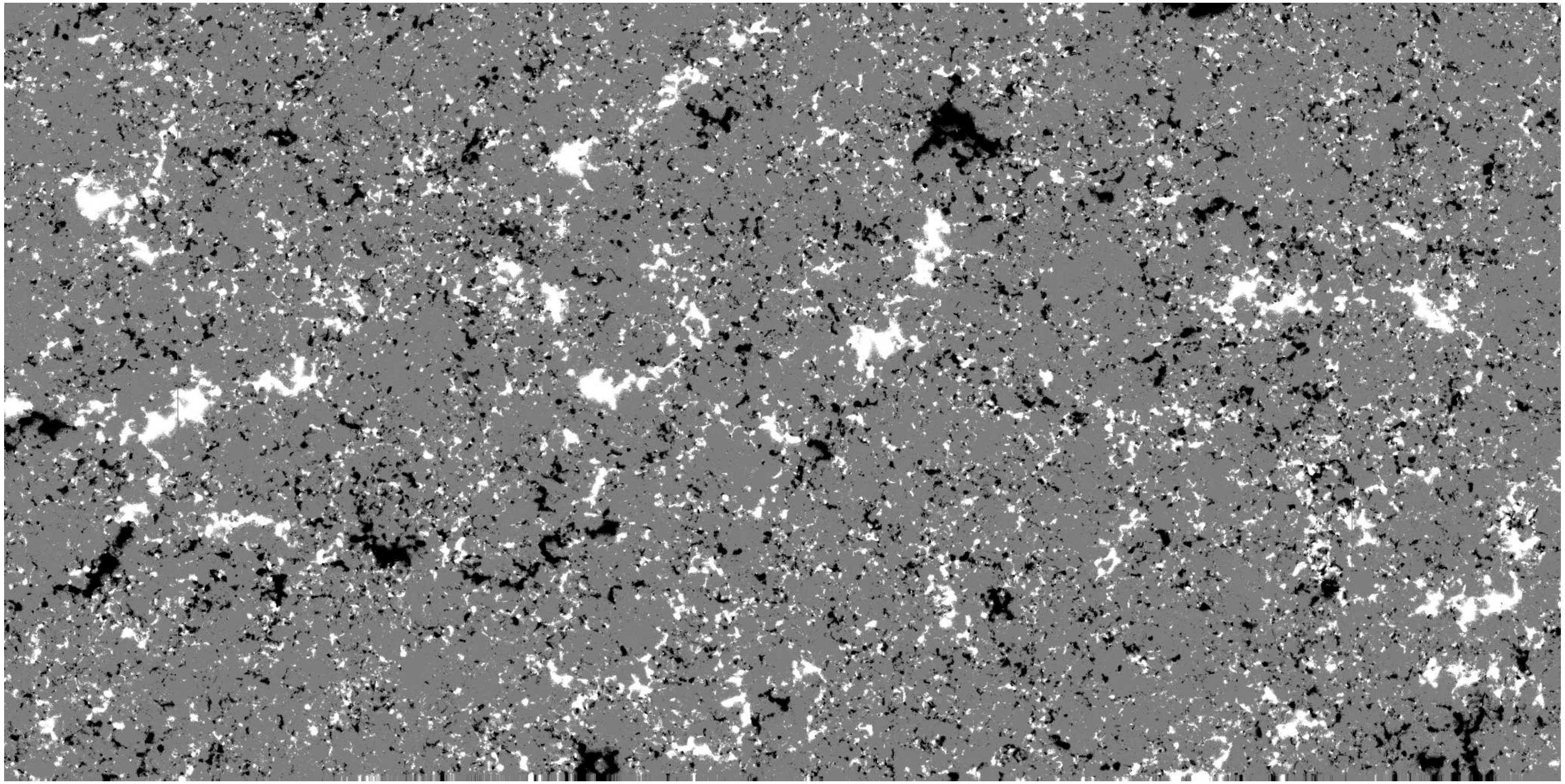

Apparent vertical magnetic flux density $B^{\mathrm{L}}_{\mathrm{app}}$ of the quiet Sun over a field of view of $302'' \times 162''$ observed from the Hinode space observatory. The grey scale saturates at ± 50 Mx cm^{-2}. 2048 steps to 5 s.

Case study II: Structure of internetwork magnetic elements (cont.)

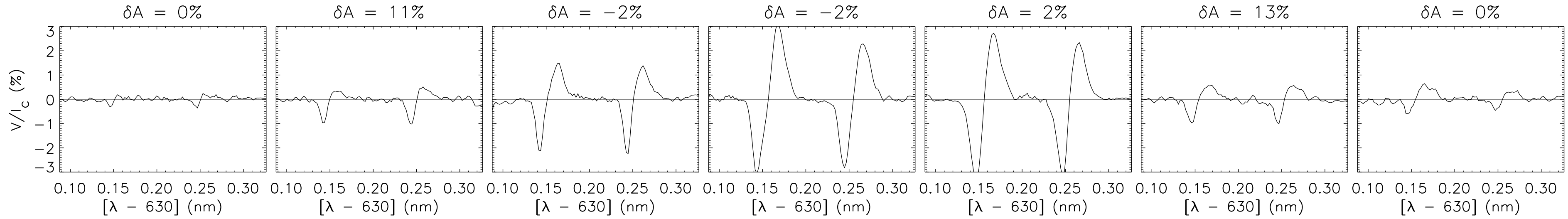

Stokes-V profiles across a magnetic element of the internetwork from the Hinode data.

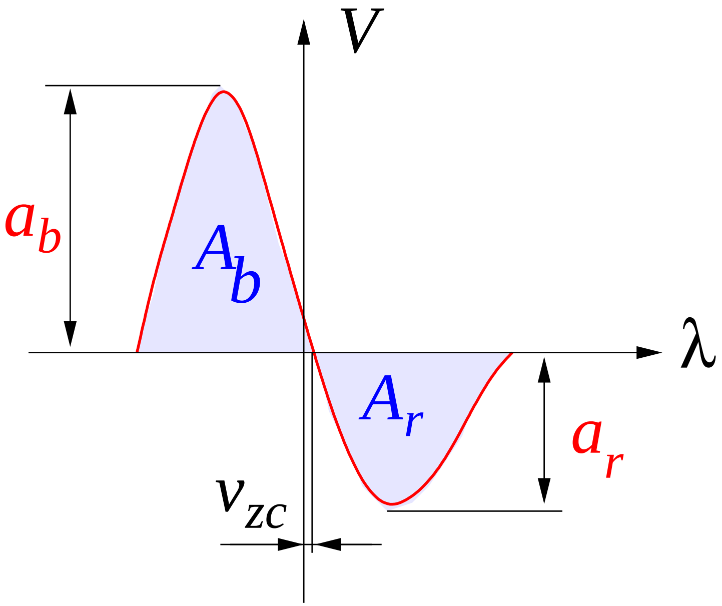

$$\delta A := \frac{A_b - A_r}{A_b + A_r}$$

$$\text{sign}(\delta A) = -\text{sign}\left(\frac{\mathrm{d}|B|}{\mathrm{d}\tau} \cdot \frac{\mathrm{d}v(\tau)}{\mathrm{d}\tau}\right)$$

Solanki & Pahlke, 1988; Sanchez Almeida et al., 1989

Case study II: Structure of internetwork magnetic elements (cont.)

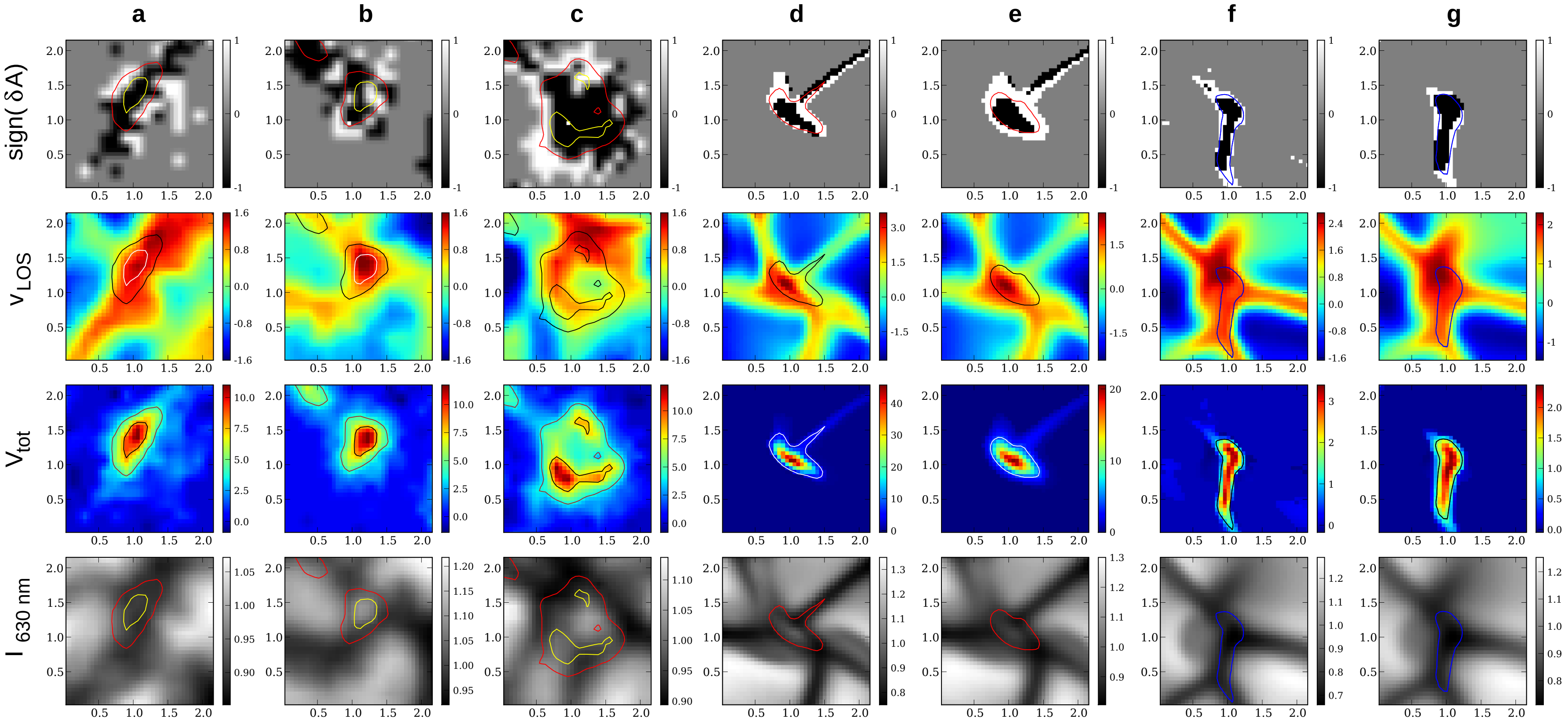

Columns a-c: observational data obtained with the spectro-polarimeter of Hinode/SOT. *Columns d and f*: synthetic data from the 3-D MHD simulation. *Columns e and g*: same as d and f but after application of the SOT-PSF to the synthetic intensity maps. Distance between tick marks is $0.5''$.

From *Rezaei, Steiner, Wedemeyer-Böhm et al. 2007, A&A 476, L33*

Case study II: Structure of internetwork magnetic elements (cont.)

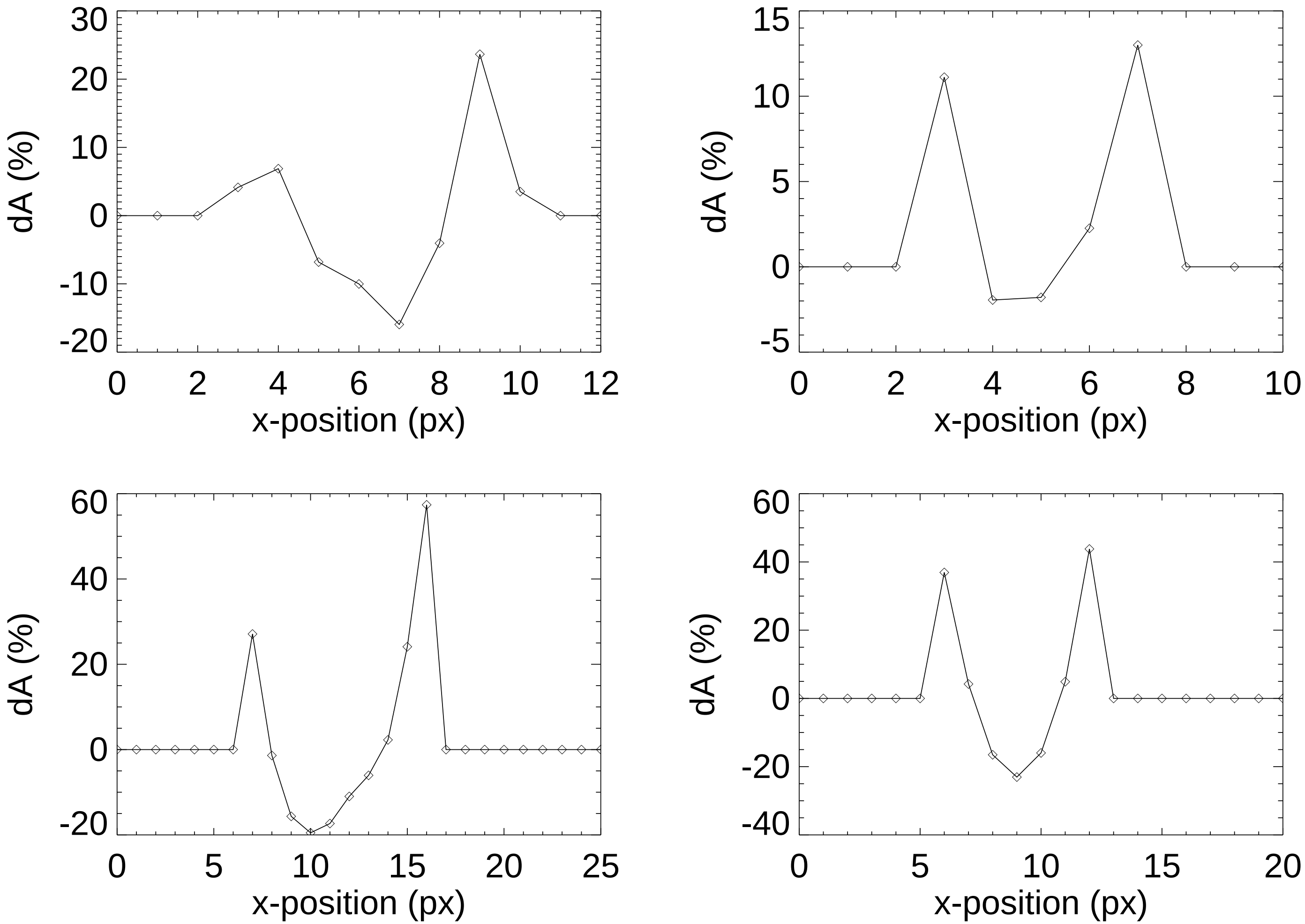

Variation in δA across magnetic elements from the Hinode data *(top row)* and the simulation *(bottom row)*.

Case study II: Structure of internetwork magnetic elements (cont.)

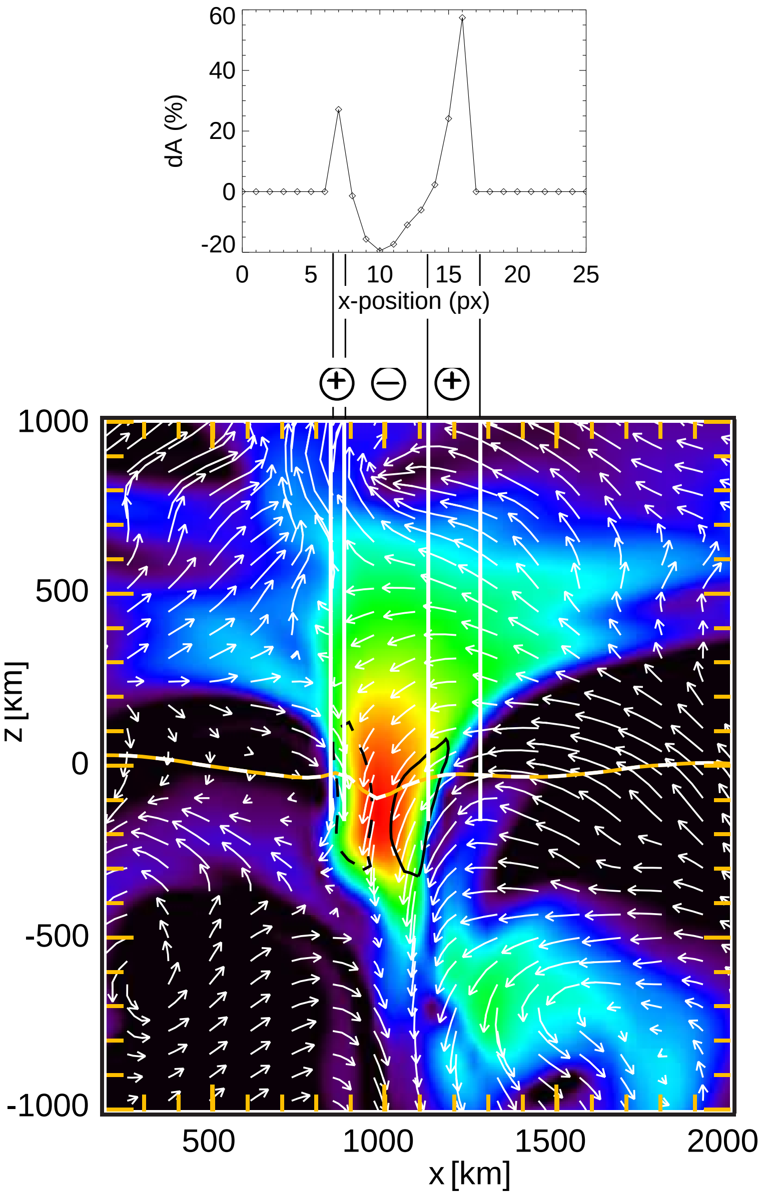

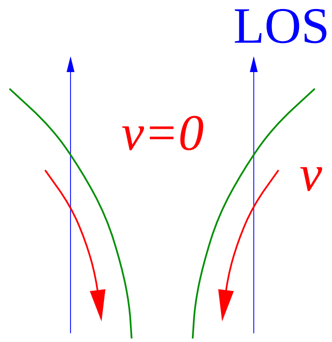

$$\left.\begin{array}{l} \frac{\mathrm{d}|B|}{\mathrm{d}\tau} < 0 \\ \frac{\mathrm{d}v(\tau)}{\mathrm{d}\tau} > 0 \end{array}\right\} \Rightarrow \delta A > 0$$

Vertical cross section through the simulation box. *Colour* displays the logarithmic magnetic field strength, *arrows* the velocity field, *black contours* the electric current density normal to the plane. The *white vertical lines* indicate ranges of either positive or negative area asymmetry, δA.

§ 22 *Case study III:* Wave propagation in a magnetically structured atmosphere

Time sequence of a two-dimensional simulation of magnetoconvection starting with an initial homogeneous vertical magnetic field of 100 G.

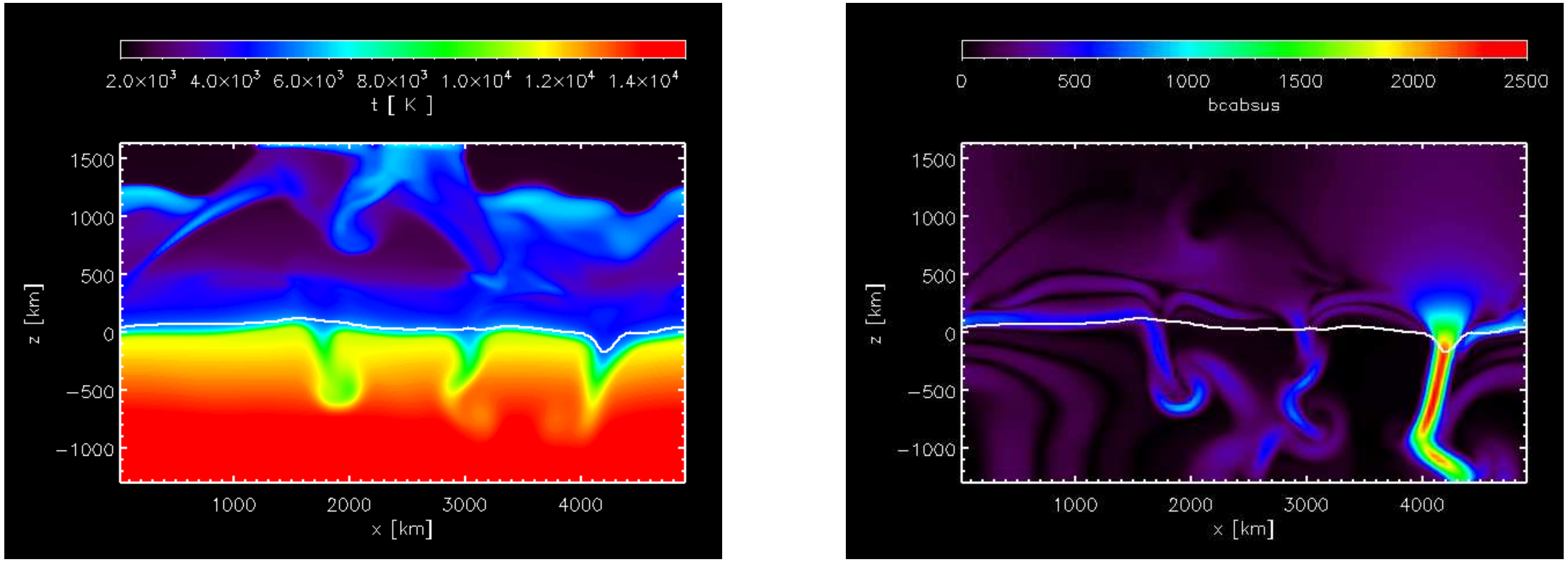

Left: Temperature, *Right:* Absolute magnetic field strength. A magnetic flux sheet has formed at $x \approx 4\,200$ km.

Case study III: Wave propagation in a magnetically structured atmosphere (cont.)

The sequence from $t = 1200$ s to $t = 1450$ s is repeated with a plane parallel, oscillatory velocity perturbation at the bottom boundary with an amplitude of 50 m/s and a frequency of 20 mHz. When subtracting the velocity field of the two sequences, the perturbation becomes visible.

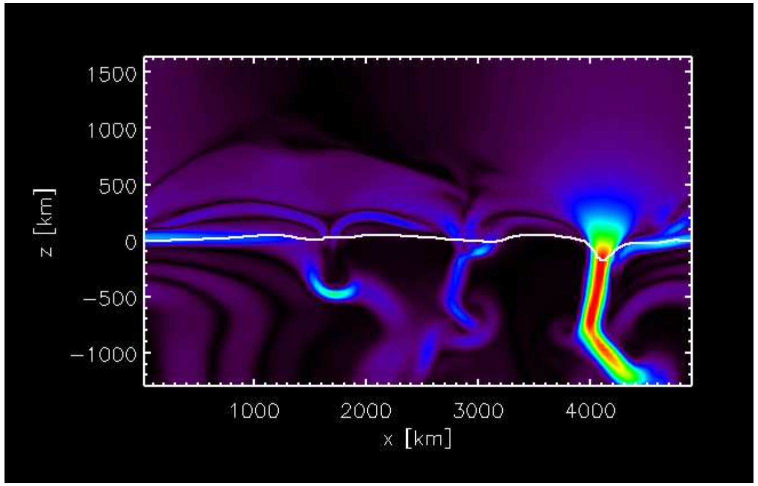

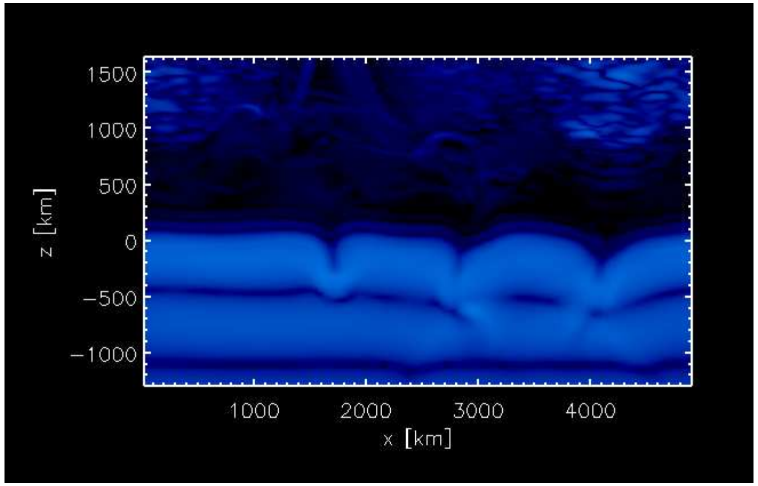

Left: Magnetic field strength. *Right:* Subtractive velocity field 116 s after starting the perturbation.

Residual velocity amplitude due to an oscillatory velocity perturbation along the bottom

$$v_z(t) = v_0 \sin(2\pi(t - t_0)\nu)$$

with an amplitude of $v_0 = 50$ m/s and a frequency of $\nu_0 = 20$ mHz from $t = 1200$ s to $t = 1450$ s. Note the fast magnetic wave that gets refracted.

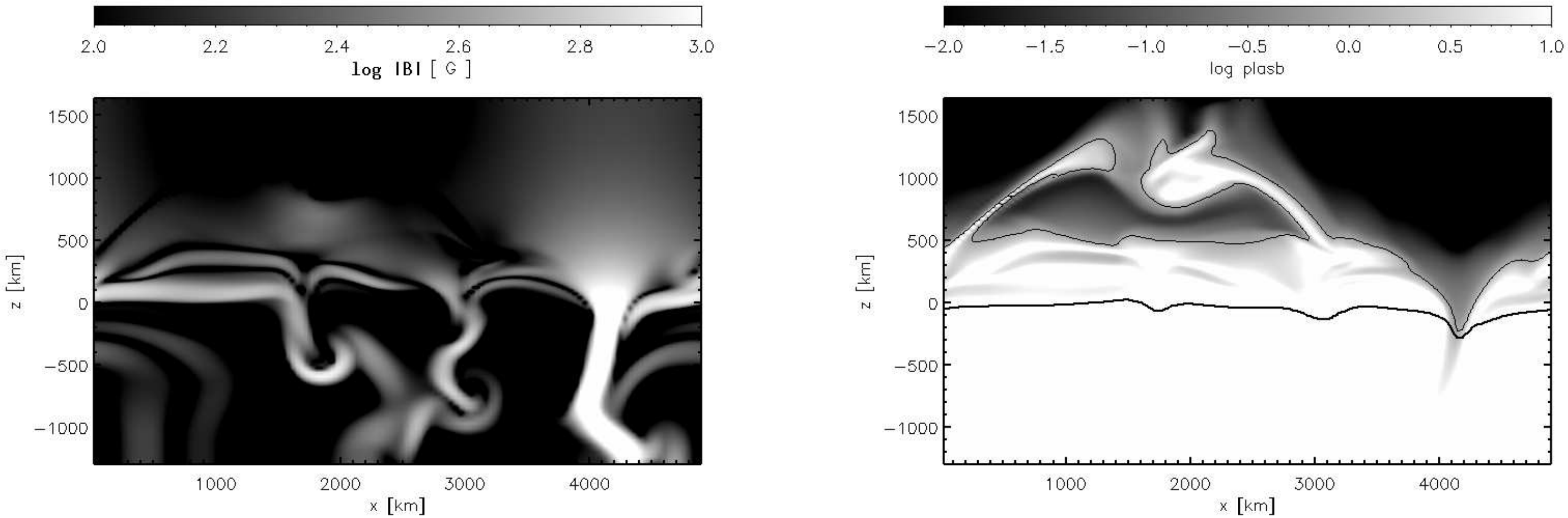

Left: Logarithmic magnetic field strength 1368 s after starting with an initial homogeneous vertical field of 100 G. *Right:* Logarithm of thermal to magnetic energy density (plasma-β) together with the conour of $\beta = 1$.

Case study III: Wave propagation in a magnetically structured atmosphere (cont.)

Wave travel time vs. canopy height.

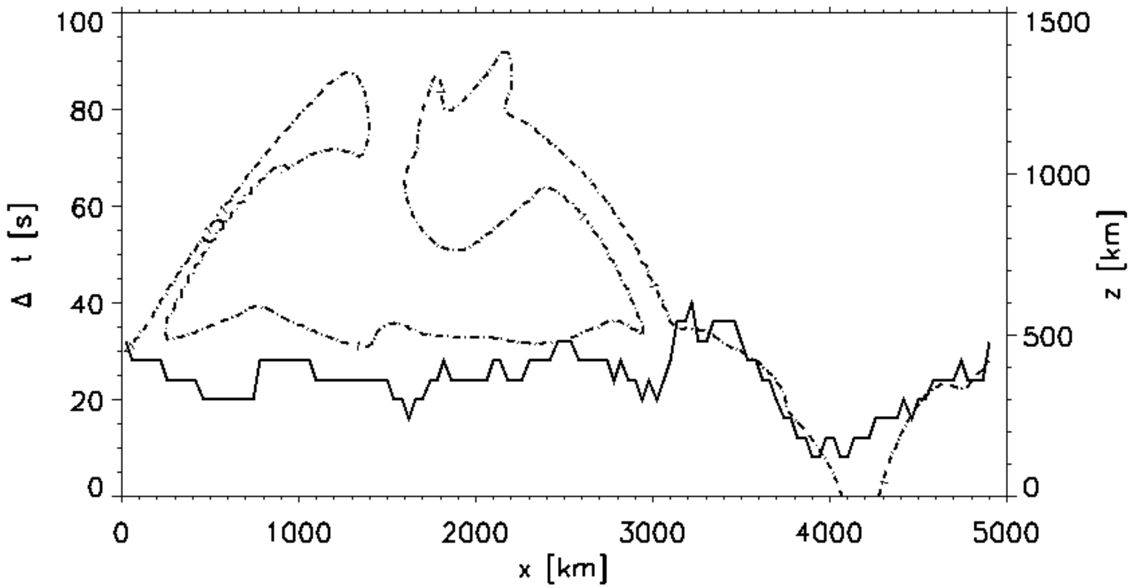

Wave travel time across the layer from $z = 200$ km to $z = 420$ km as a function of horizontal distance (thick solid curve). Superposed is the contour of $\beta = 1$ (magnetic and thermal equipartition), for which the height is indicated in the right hand side ordinate (dash-dotted curve). Note that the travel time markedly decreases where the low β region intrudes this layer. From *Steiner, Vigeesh, Krieger et al. 2007*

Case study III: Wave propagation in a magnetically structured atmosphere (cont.)

Finsterle et al. 2004, ApJ 613, L185 suggest to determine the three-dimensional topography of the $\beta = 1$-surface by measuring the travel time of high frequency waves between lines formed below and above this surface. They use a MOTH-MDI combined data set of 17.8 h duration

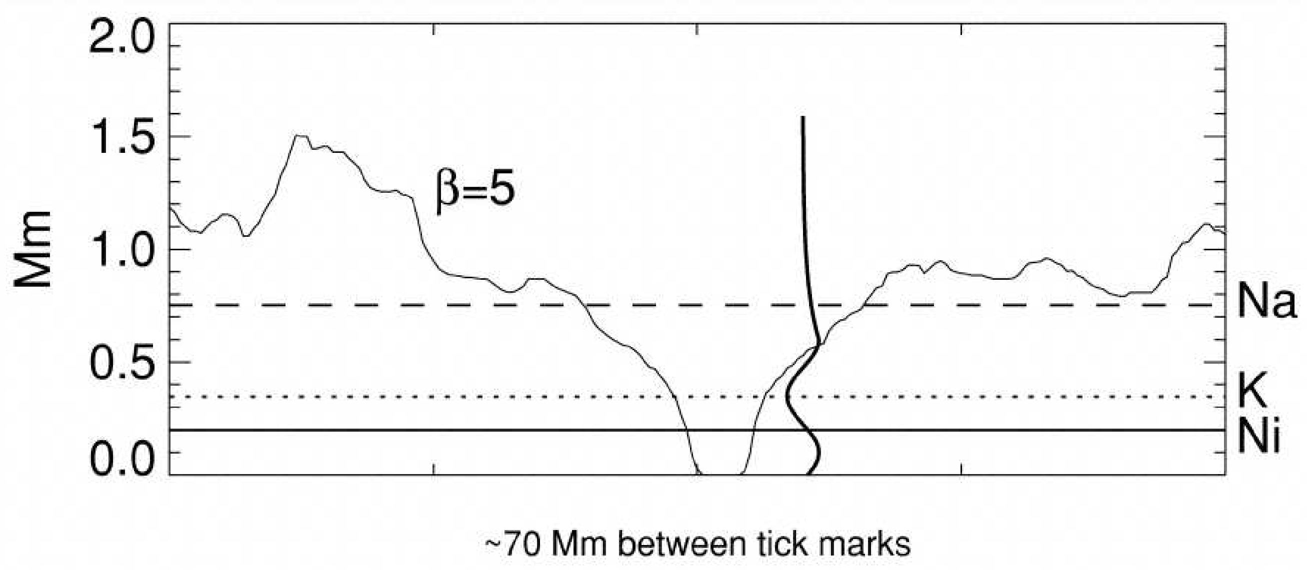

Helioseismic mapping of the magnetic canopy in the solar chromosphere

Case study III: Wave propagation in a magnetically structured atmosphere (cont.)

Maps of travel time for 7 mHz waves between the formation layers of (**a**) Ni and Na, (**b**) K and Na, and (**c**) Ni and K. (**d**) the contemporaneous MDI magnetogram. $\beta \approx 1$ contours at 200 km (white), 420 km (black-white), and 800 km (black) above $\tau_c = 1$.

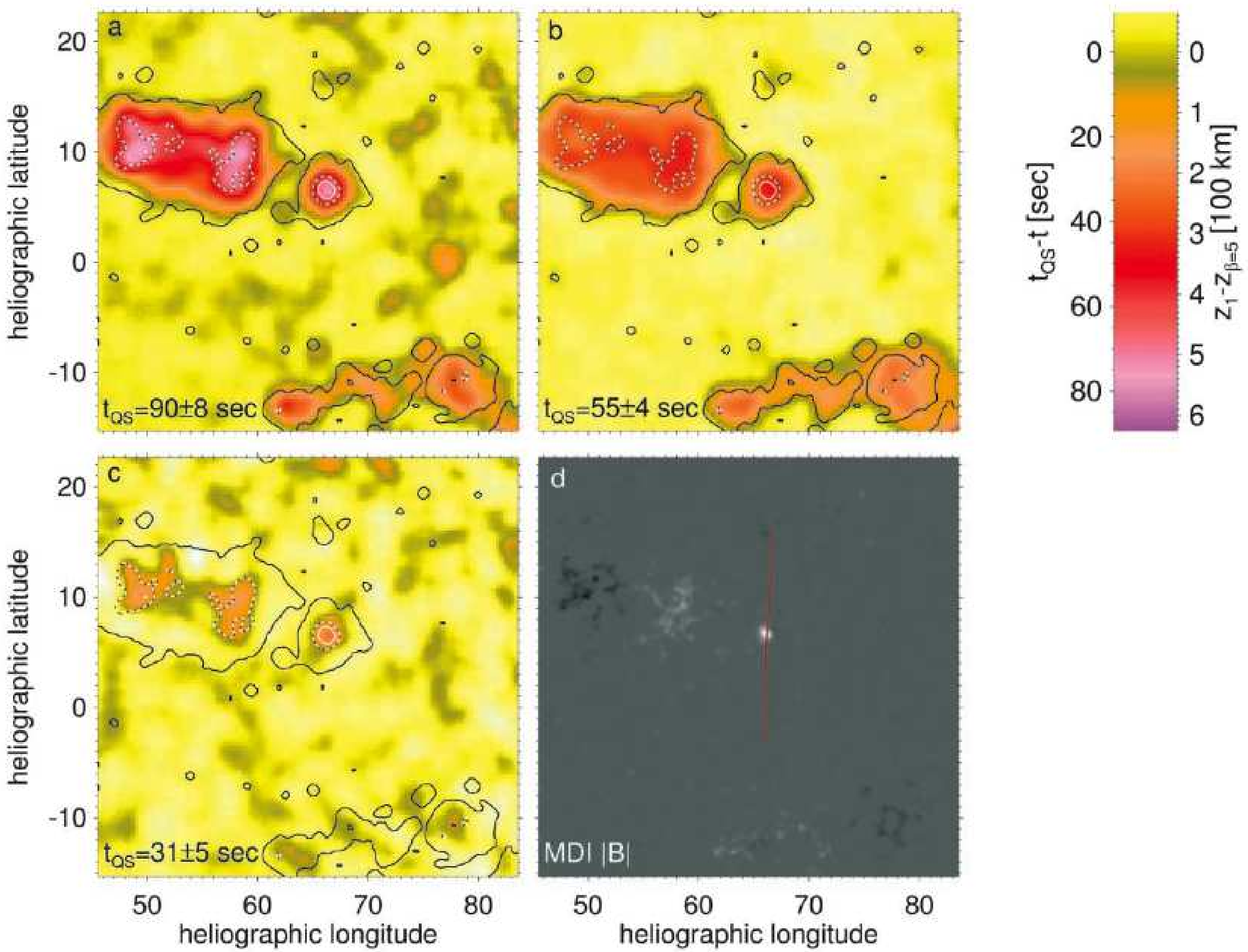

From *Finsterle et al. 2004, ApJ 613, L185*

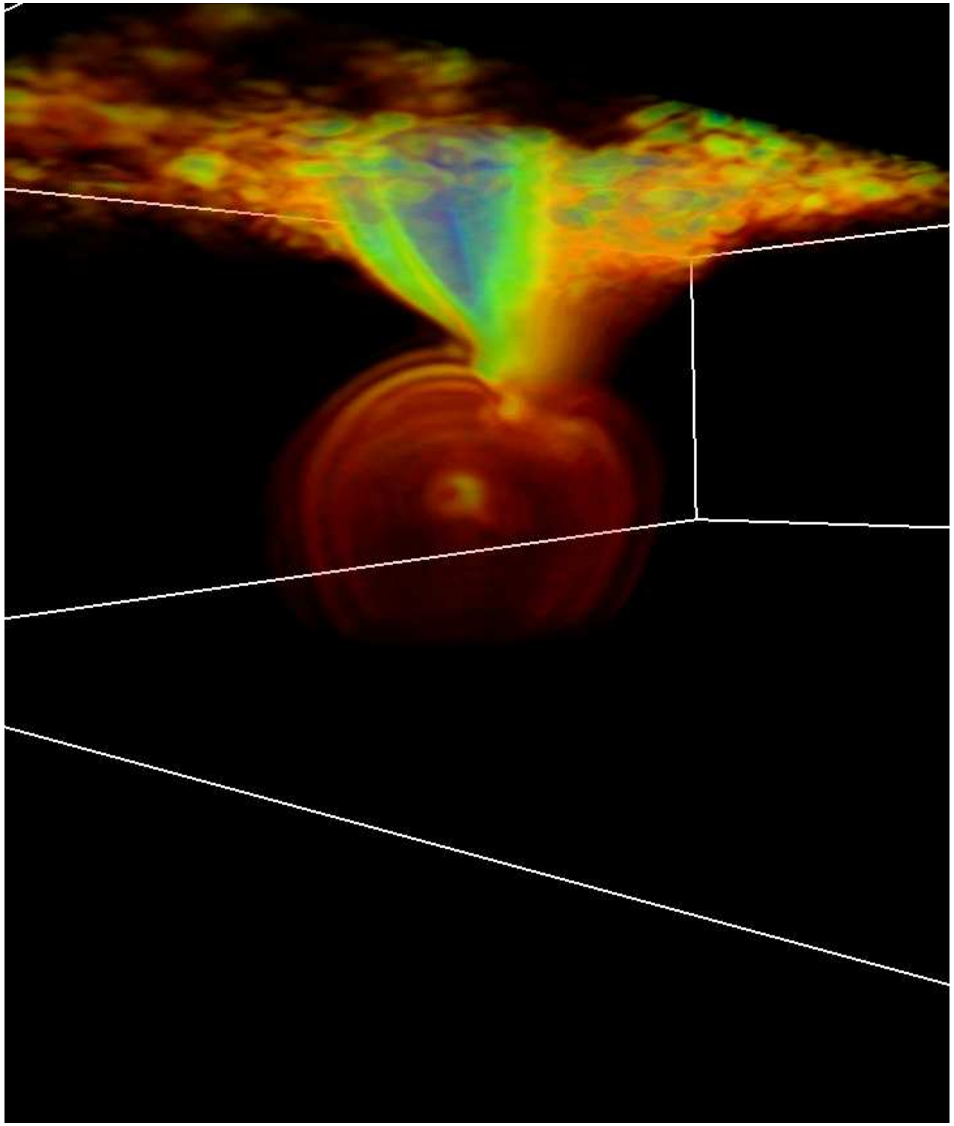

Time instant of a spherical, fast acoustic wave, initiated by a local pressure perturbation in the convection zone. When the wave encounters the low beta magnetic flux concentration in the photosphere it partially converts into a fast magnetic mode, which shows the typical “faning out” already encountered in the 2-D simulation. Colors show absolute velocity perturbation. Courtesy *Christian Nutto, KIS*.

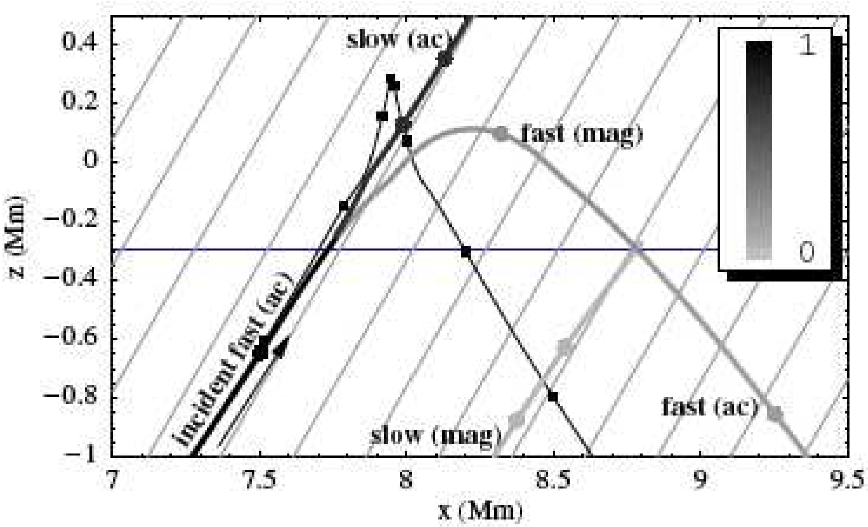

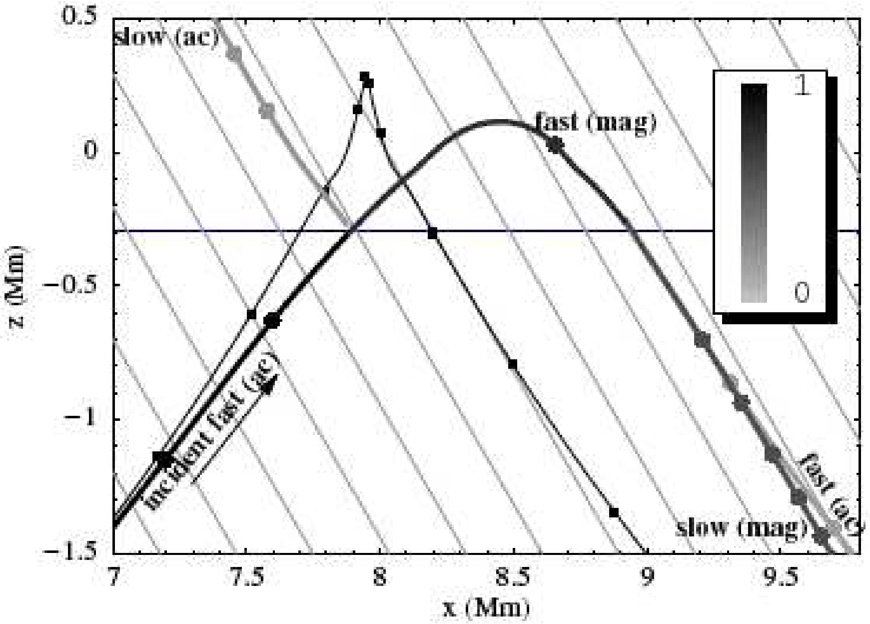

2 kG uniform magnetic field inclined at $\pm 30^\circ$ to the vertical. The incoming 5 mHz rays have lower turning points at $z = -5$ Mm. The horizontal grey line indicates where the sound and Alfvén speeds coincide. The fractional energy remaining in each resulting ray is indicated in grey scales. The dots on the ray paths indicate 1 min group travel time intervals. The thin black curve represents the acoustic ray that would be there in the absence of magnetic field. From *Cally (2007) AN 328, 286*

Movie top panel

Movie bottom panel

Case study III: Wave propagation in a magnetically structured atmosphere (cont.)

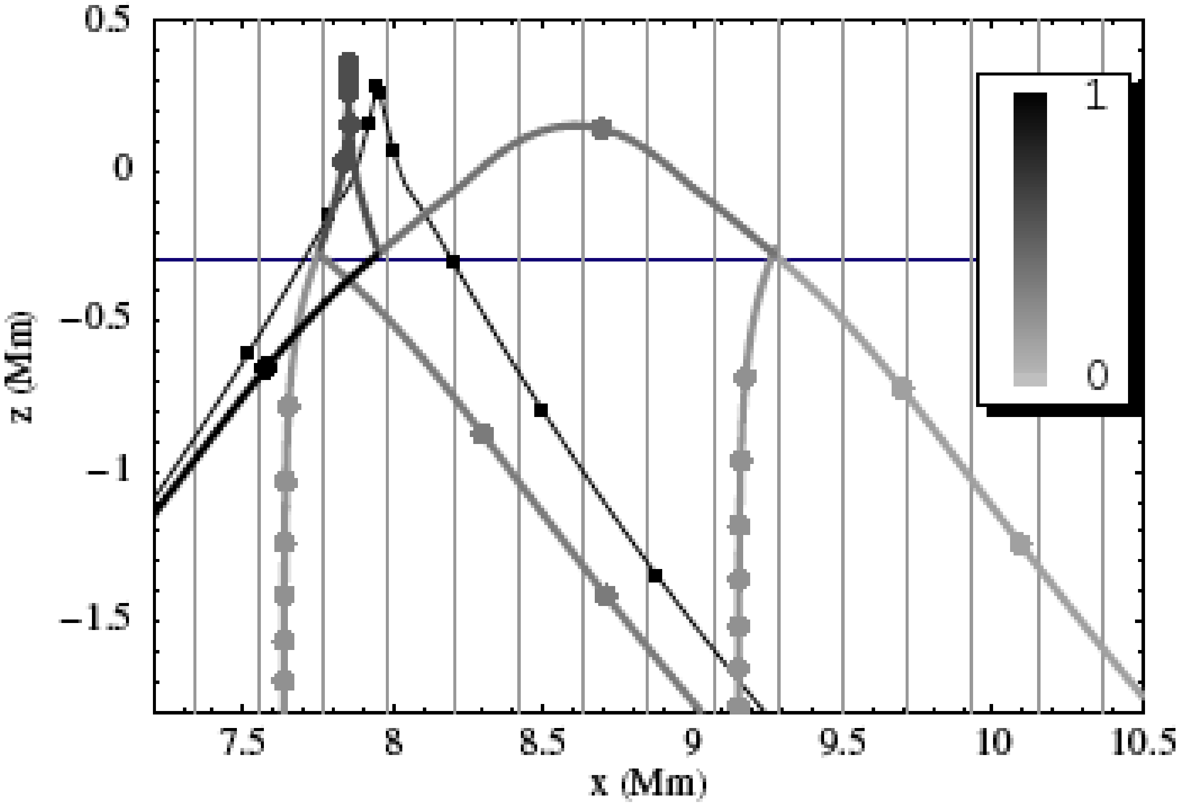

2 kG uniform vertical magnetic field. Here, the 5 mHz frequency is not sufficient to overcome the atmospheric acoustic cutoff (5.2 mHz), and the upgoing slow ray reflects back downward. From *Cally (2007) AN 328, 286*

Case study III: Wave propagation in a magnetically structured atmosphere (cont.)

Transversal, impulsive excitation at the footpoint of a magnetic flux sheet.

$v_x = v_0 \sin(2\pi t/P)$, $P = 24$ s, $v_0 = 750$ ms^{-1}

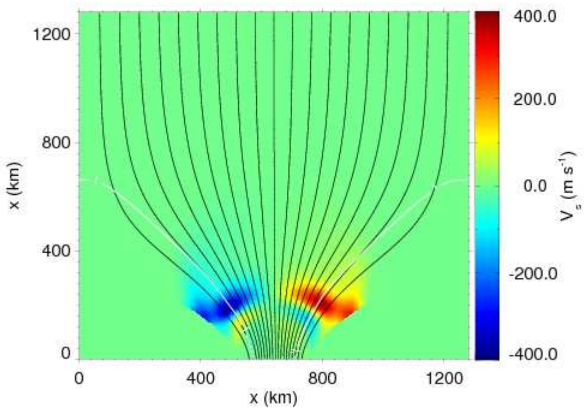

$v_{||}$ after 40 s

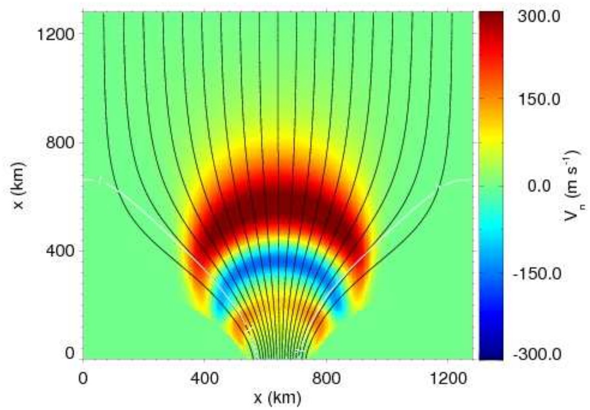

$v_{\perp}$ after 40 s

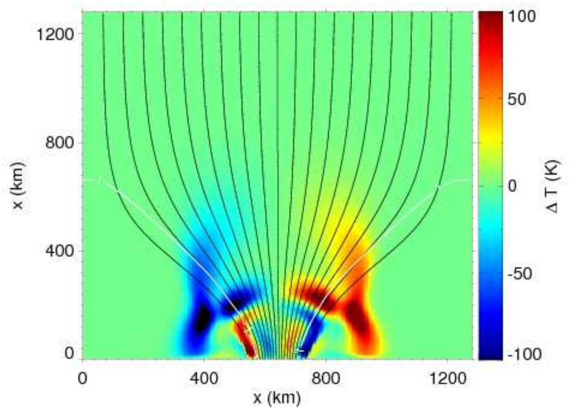

δT after 40 s

§ 22 *Case study IV:* The restless chromosphere

Simulations show a fast changing pattern of enhanced temperatures in the chromosphere, termed the *the fluctosphere*, or *clapotisphere*. It is distinctly different from the pattern of inverse granulation in the middle photosphere, and the granulation itself.

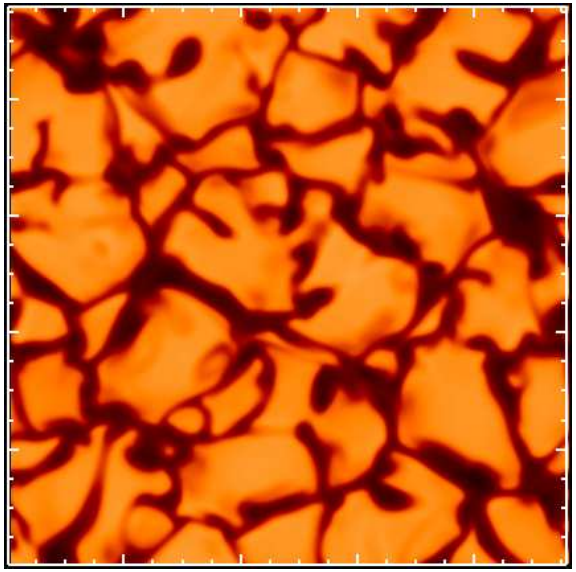

$T(z = -200\mathrm{km})$

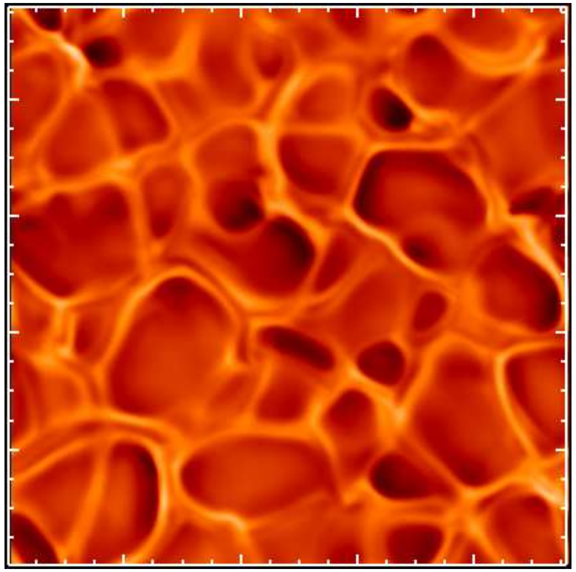

$T(z = +200\mathrm{km})$

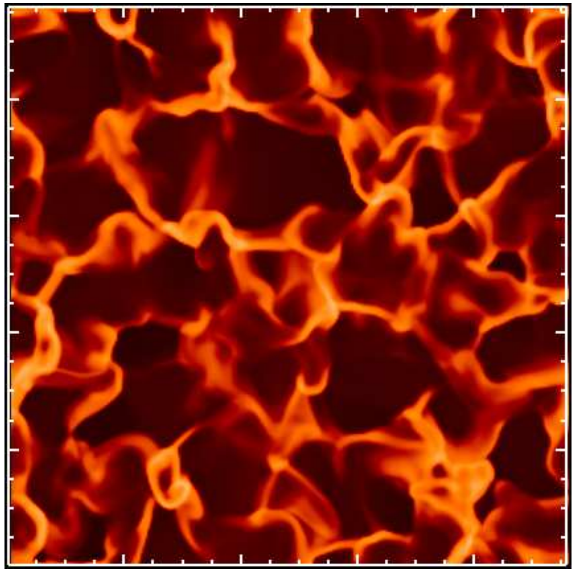

$T(z = +1000\mathrm{km})$

Filtergrams in the infrared line Ca II 854 nm

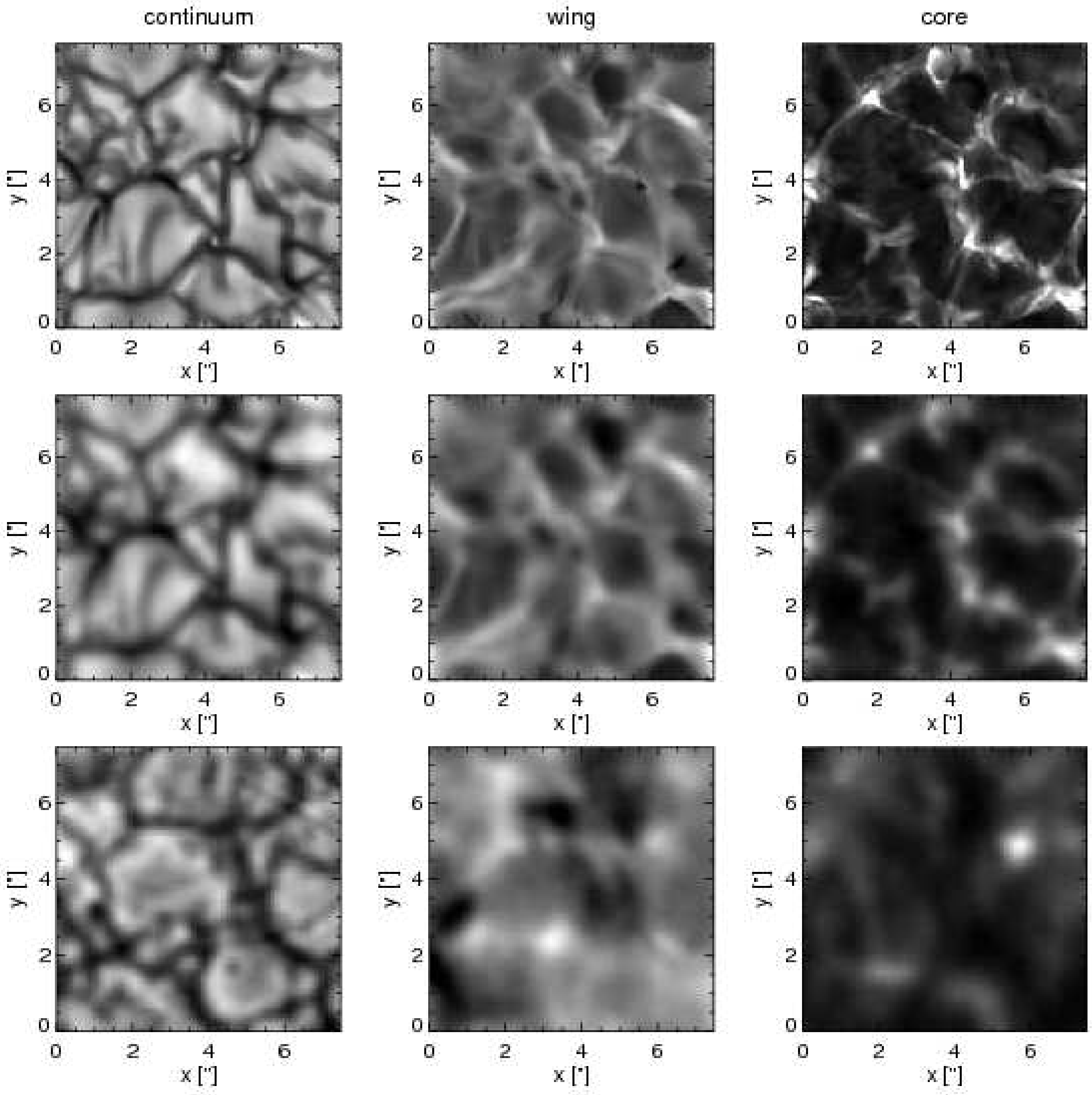

simulation

simulation
+ PSF

observation

Wöger et al. 2006

observed in 0.3 Å filtergrams centred at the Ca II K_{2v} peak a short-lived pattern with a typical spatial scale of 1.95" and a mean evolution time scale of 53 s.

Courtesy, S. Wedemeyer-Böhm

Case study IV: The restless chromosphere (cont.)

Intensity image at $\lambda = 1$ mm of the "fluctosphere" at different spatial resolutions:

a) 0.06" (size of computational grid cells), **b**) 0.3", **c**) 0.6", **d**) 0.9".

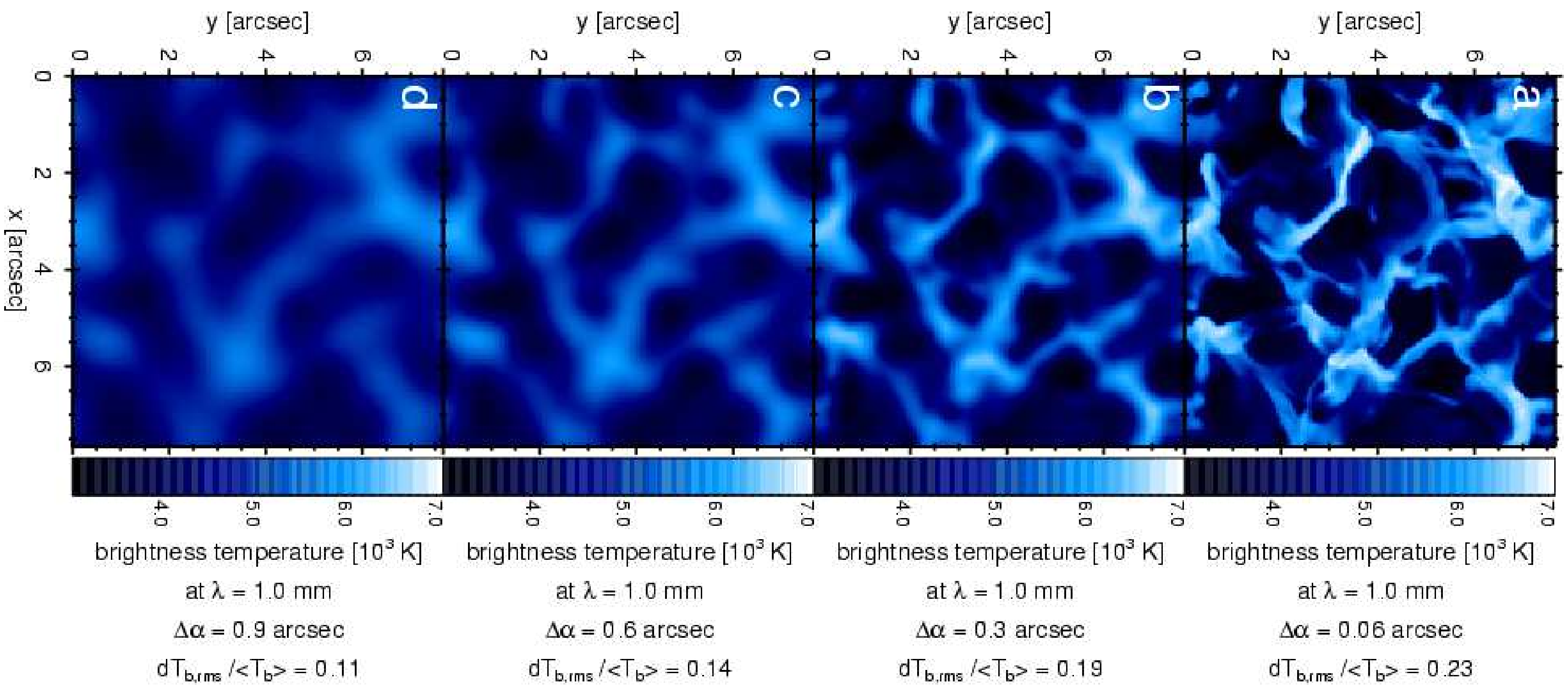

From *Wedemeyer-Böhm et al., A&A 471, 977 (2007)*

Case study IV: The restless chromosphere (cont.)

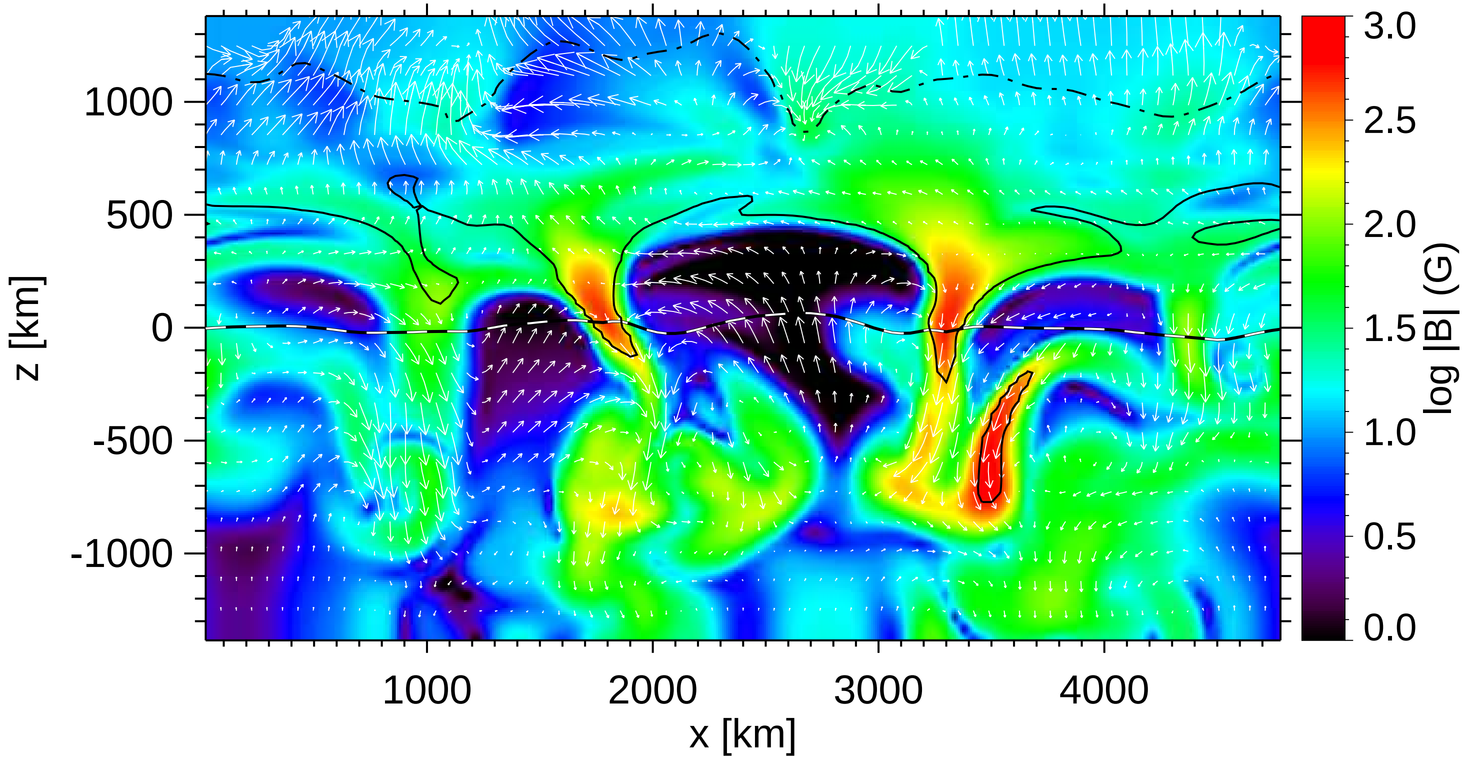

Snapshot of a vertical section showing $\log|B|$ (color coded) and *velocity vectors* projected on the vertical plane (white arrows). The b/w dashed curve shows optical depth unity and the dot-dashed and solid black contours $\beta = 1$ and 100, respectively.

movie with $\beta = 1$ surface

Schaffenberger, Wedemeyer-Böhm, Steiner & Freytag, 2005, in *Chromospheric and Coronal Magnetic Fields*, Innes, Lagg, Solanki, & Danesy (eds.), ESA Publication SP-596

Case study IV: The restless chromosphere (cont.)

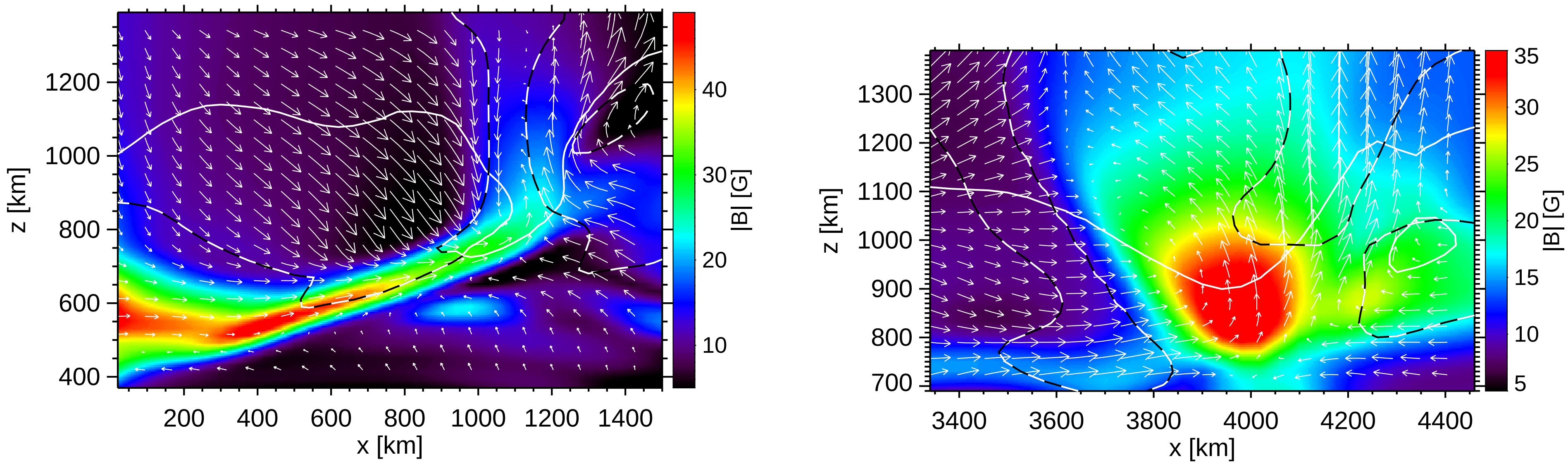

Two instances of shock induced magnetic field compression. Absolute magnetic flux density (colors) with velocity field (arrows), $\mathrm{Mach} = 1$-contour (dashed) and $\beta = 1$-contour (white solid).

References

Abbett, W.P.: 2007, *The Magnetic Connection between the Convection Zone and Corona in the Quiet Sun*, ApJ 665, 1469-1488

Berger, T. E., Rouppe van der Voort, L. H. M., Löfdahl, M. et al.: 2004, A&A 428, 613

Cally, P. S.: 2007, Astronomische Nachrichten/AN, 328, 286

Dunn, R. B. and Zirker, J. B.: 1973, Solar Phys. 33, 281

Finsterle, W., Jefferies, S., Cacciani, A., Rapex, P., McIntosh, S.: 2004, ApJ 613, L185

Galloway, D. J. and Weiss, N. O.: 1981, *Convection and magnetic fields in stars*, ApJ 243, 945

Grossmann-Doerth, Schüssler, M., Steiner, O.: 1998, *Convective intensification of solar surface magnetic fields: results of numerical experiments*, A&A 337, 928-939

Harvey, J. W., Branston, D., Henney, C. J. and Keller, C.U.: 2007, *Seething horizontal magnetic fields in the quiet solar photosphere*, ApJ 659, L177-L180

Ishikawa, R., Tsuneta, S., Ichimoto, K., Isobe, H., Katsukawa, Y., Lites, B. W., Nagata, S., Shimizu, T., Shine, R. A., Suematsu, Y., Tarbell, T. D., & Title, A. M.: 2008, *Transient horizontal magnetic fields in solar plage regions*, A&A 481, L25-L28

Isobe, H., Proctor, M.R.E., and Weiss, N.O.: 2008, *Convection-driven Emergence of Small-Scale Magnetic Fields and their Role in Coronal Heating and Solar Wind Acceleration*, ApJ 679, L57-L60

References (cont.)

Lites, B. W., Kubo, M., Socas-Navarro, H., Berger, T., Frank, Z., Shine, R., Tarbell, T., Title, A., Ichimoto, K., Katsukawa, Y., Tsuneta, S., Suematsu, Y., Shimizu, T., and Nagata, S.: 2008, *The Horizontal Magnetic Flux of the Quiet-Sun Internetwork as Observed with the Hinode Spectro-Polarimeter*. ApJ 672, 1237-1253

Martinez Pillet, V., Lites, B. W., Skumanich, A.: 1997, ApJ 474, 810

Mehltretter, J. P.: 1974, Solar Phys., 38, 43

Meunier, N., Solanki, S. K., Livingston, W. C.: 1998, A&A 332, 771

Muller, R.: 1985, Solar Phys., 100, 237

Orozco Suárez, D., Bellot Rubio, L. R., del Toro Iniesta, J. C., Tsuneta, S., Lites, B. W., Ichimoto, K., Katsukawa, Y., Nagata, S., Shimizu, T., Shine, R. A., Suematsu, Y., Tarbell, T. D., & Title, A. M.: 2007, *Quiet-Sun internetwork magnetic fields from the inversion of HINODE measurements*, ApJ 670, L61-L64

Rezaei, R., Steiner, O., Wedemeyer-Böhm, Schlichenmaier, R., Schmidt, W., and Lites, B.W.: 2008, *Hinode observations reveal boundary layers of magnetic elements in the solar photosphere*, A&A 476, L33-L36

Sánchez Almeida, J., Collados, M., and del Toro Iniesta, J.C.: A&A 222, 311

References cont.

Schaffenberger, W., Wedemeyer-Böhm, S., Steiner, O., and Freytag, B.: 2005, *Magnetohydrodynamic simulation from the convection zone to the chromosphere*, in Chromospheric and Coronal Magnetic Fields, D. Innes, A. Lagg, S.K. Solanki, and D. Danesy (eds.), ESA Publication, SP-596

Schaffenberger, W., Wedemeyer-Böhm, S., Steiner, O., and Freytag, B.: 2006, *Holistic MHD-simulation from the convection zone to the chromosphere*, in Solar MHD: Theory and Observations – a High Spatial Resolution Perspective, J. Leibacher, H. Uitenbroek, & R.F. Stein (eds.), ASP Conference Series

Schüssler, M., & Vögler, A.: 2008, *Strong horizontal photospheric magnetic field in a surface dynamo simulation*, A&A 481, L5-L8

Solanki, S.K. and Pahlke, K.D.: 1988, A&A 201, 143

Steiner, O., Rezaei, R., Schaffenberger, W., and Wedemeyer-Böhm: 2005, *The Horizontal Internetwork Magnetic Field: Numerical Simulations in Comparison to Observations with Hinode*, ApJ 680, L85-L88

References cont.

Steiner, O., Rezaei, R., Schaffenberger, W., Wedemeyer-Böhm, and Schlichenmaier, R.: 2009, *The horizontal magnetic field of the quiet Sun: Numerical simulations in comparison to observations with Hinode*, in ASP Conf. Ser.: Second Hinode Science Meeting: Beyond Discovery – Toward Understanding, M. Cheung, B.W. Lites, T. Magara, J. Mariska, and K. Reeves (eds.), in press

Steiner, O., Vigeesh, G., Krieger, L., et al. 2007: Astronomische Nachrichten/AN, 328, 323

Vögler, A., Shelyag, S., Schüssler, M., Cattaneo, F., Emonet, T., Linde, T.: 2008, *Point spread functions for the Solar Optical Telescope onboard Hinode*, A&A 429, 335-351

Wedemeyer-Böhm, S.: 2008, *Point spread functions for the Solar Optical Telescope onboard Hinode*, A&A 487, 399-412

Wedemeyer-Böhm, S., Lagg, A., and Nordlund, Å.: 2008, Space Science Reviews, 171

Wedemeyer-Böhm, S., Ludwig, H.G., Steffen, M., Leenaarts, J., and Freytag, B.: 2007, 471, 977

Weiss, N. O.: 1966, Royal Society of London Proceedings Series A, 293, 310

Part VI: Future directions

§ 24 Simulations at large scales and high resolution

Big: Efforts are underway to increase the simulation box so as to accommodate a supergranulation cell. Recently, *Stein et al.* carried out a simulation of $48 \times 48 \times 20$ Mm using 500^3 grid cells. With this simulation they hope to find out more about the *origin of supergranulation* and to carry out *helioseismological experiments*.

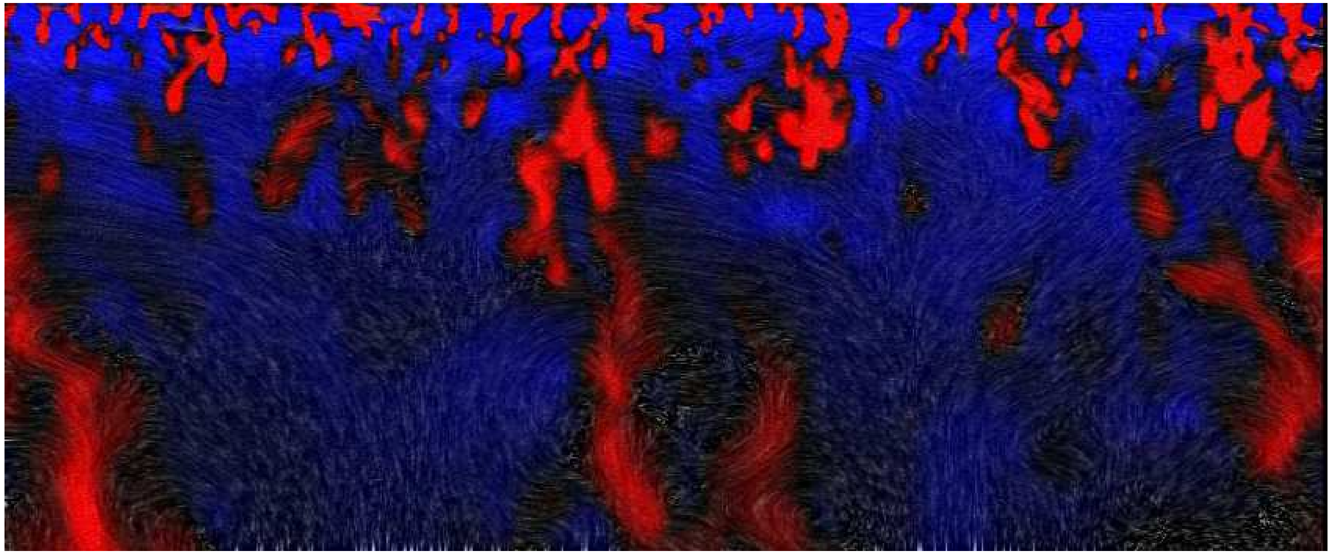

Courtesy, R.F. Stein

Bigger: Numerical simulation of a pair of sunspots: Intensity map.

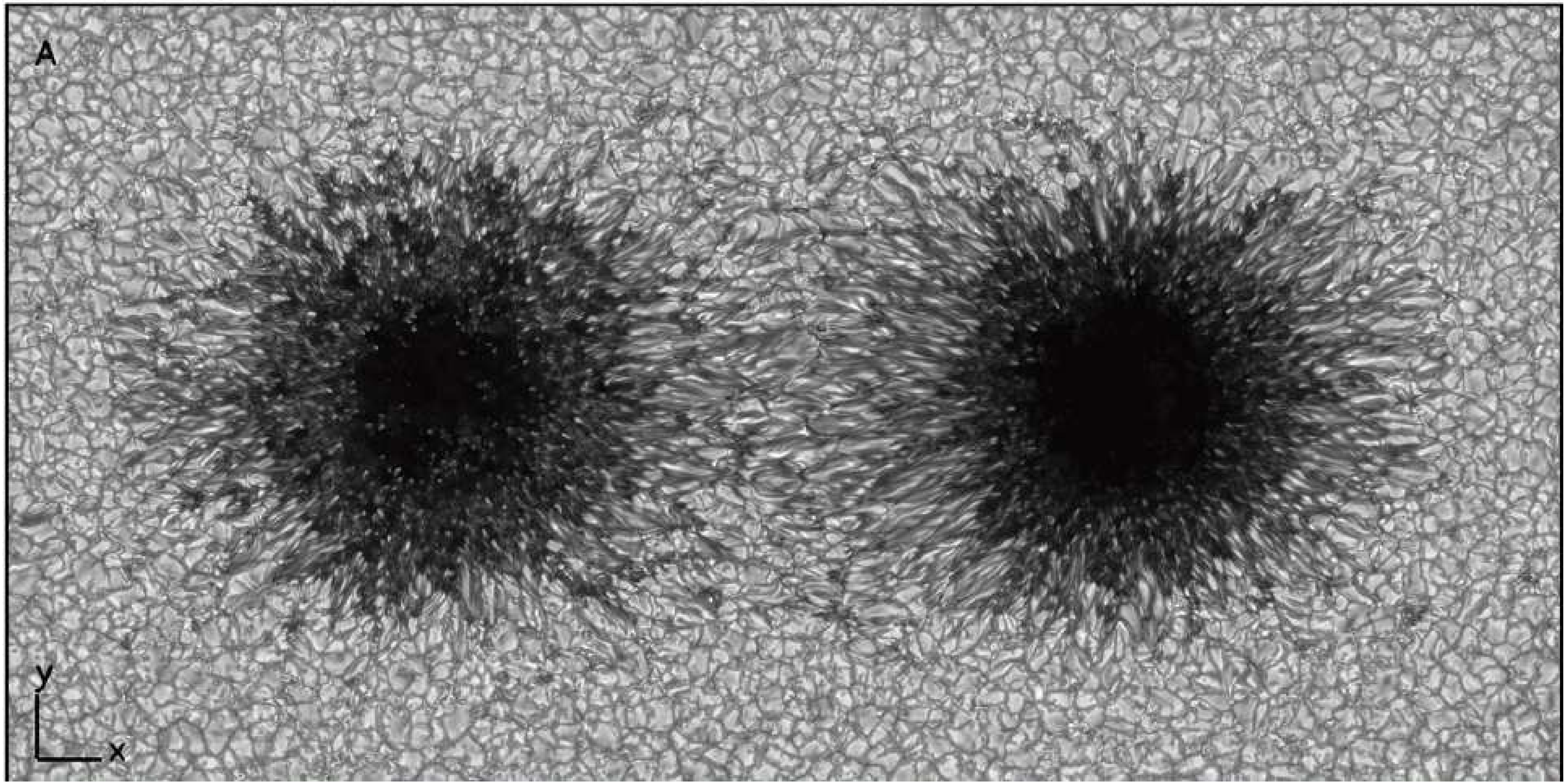

Movie of B_z. *Rempel, M., Schüssler, M., Cameron, R.H., and Knölker, M. (2009)*

Simulations at large scales and high resolution (cont.)

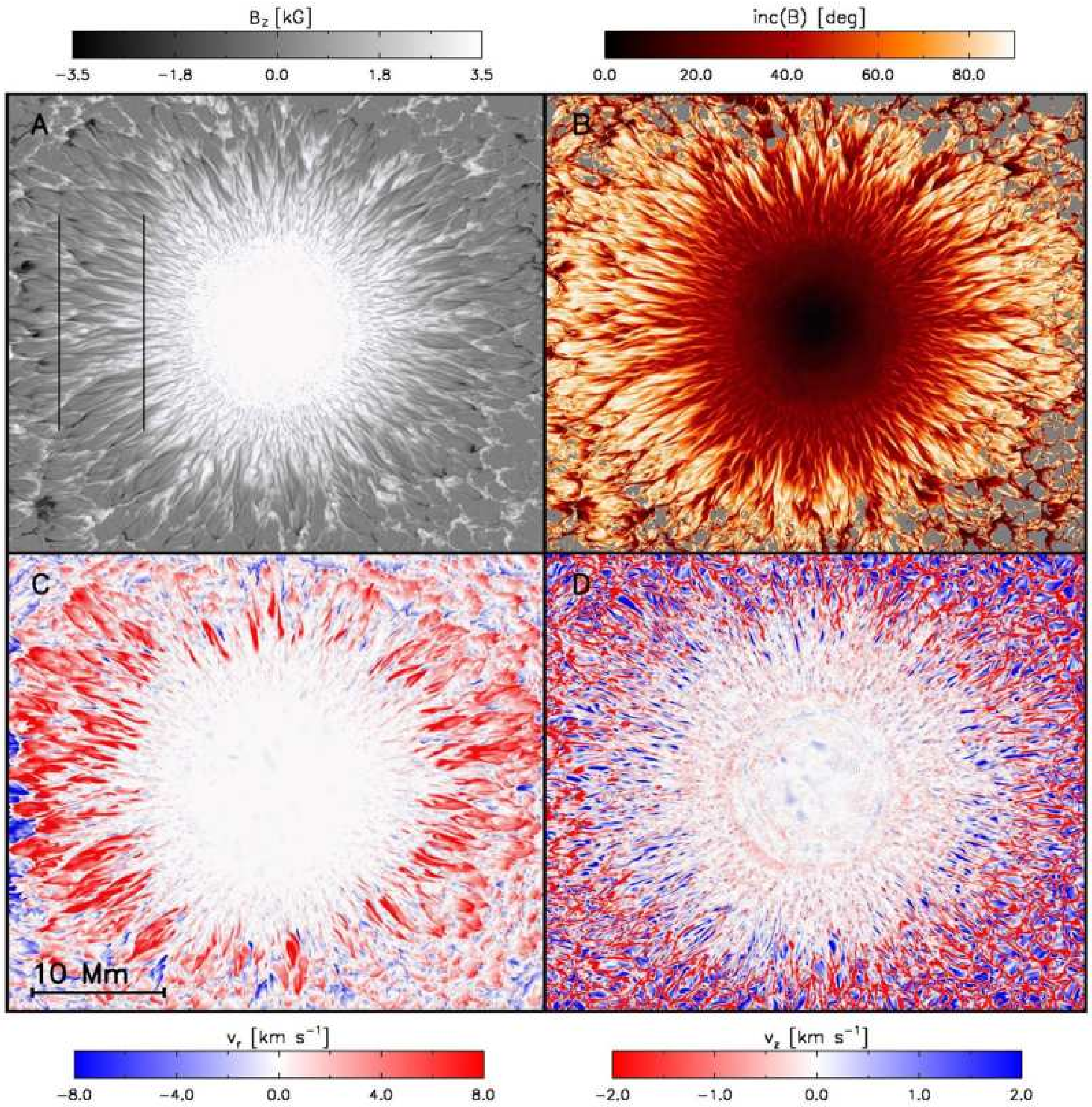

These simulations suggest a unified physical explanation for umbral dots and the penumbrae in terms of magneto-convection in a magnetic field with varying inclination. A consistent physical picture of all observational characteristics of sunspots and their surroundings is emerging.

(A) B_z, *(B)* inclination angle of B, *(C)* radial outflow velocity (red outflow), *(D)* vertical velocity.

Biggest: Global simulation of the solar convection zone.

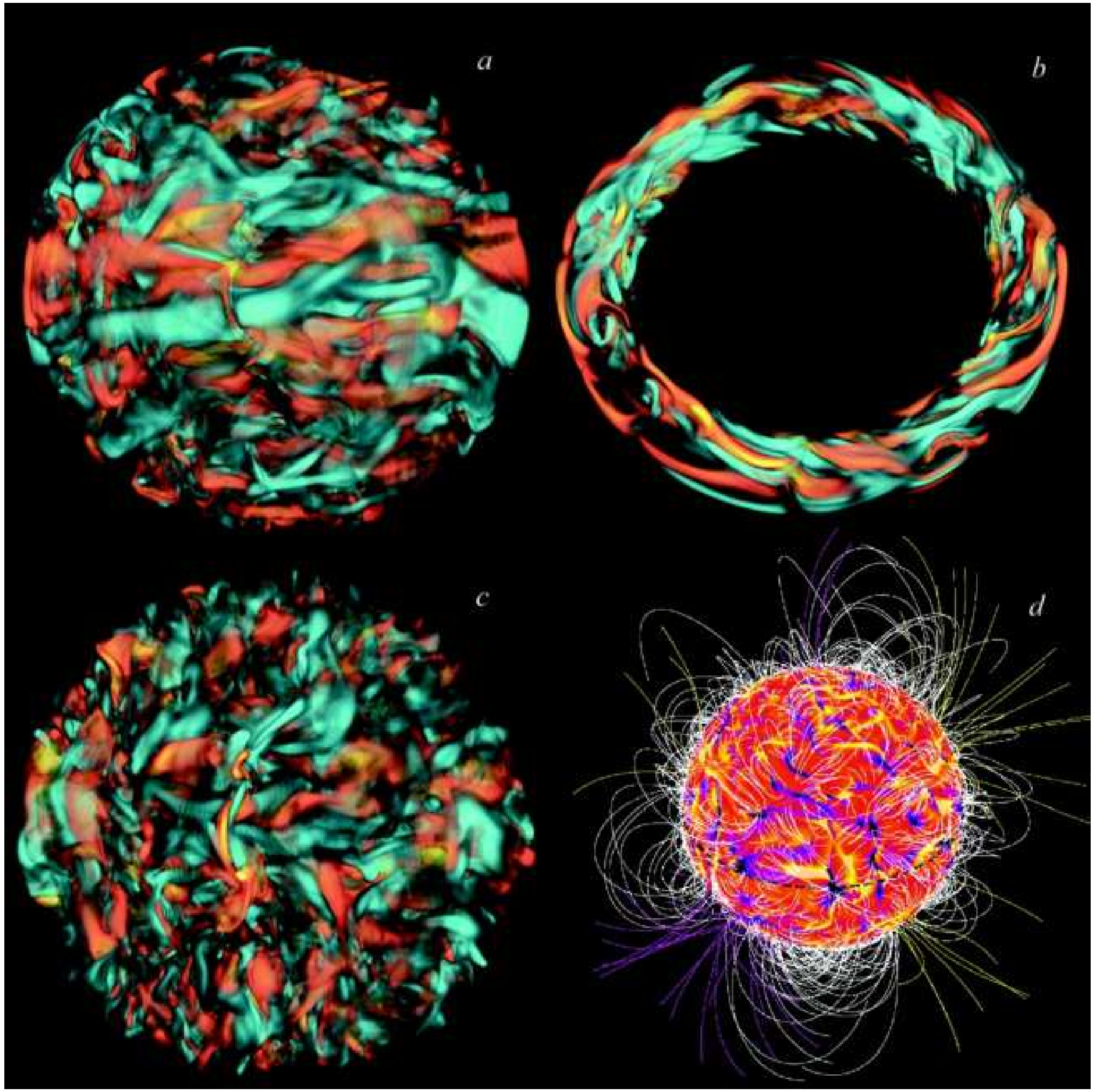

(a,c) Volume renderings of B_Φ and B_r. Red tones indicate prograde fields, and blue tones denote retrograde fields. *(b)* Selected subvolume of B in the equatorial plane. Typical field strengths are about 1000 G for B_r and 3000 G for B_Φ. *(d)* Potential field extrapolation of the radial magnetic field.

Movie: Radial magnetic field in a rotating convective spherical shell. Dark tones for the negative polarity and bright tones for the positive polarity.

Movie: Radial convective velocity. Blue/black tones for downfows and red/yellow tones for upflows.

Brun, Miesch & Toomre (2004)

Simulations at large scales and high resolution (cont.)

"Holistic simulation" encompassing the solar atmosphere from the top layers of the convection zone up into the corona. The formation of jets such as dynamic fibrils, mottles, and spicules in the solar chromosphere are in the focus of such simulations.

Hansteen, Carlsson & Gudiksen (2007)

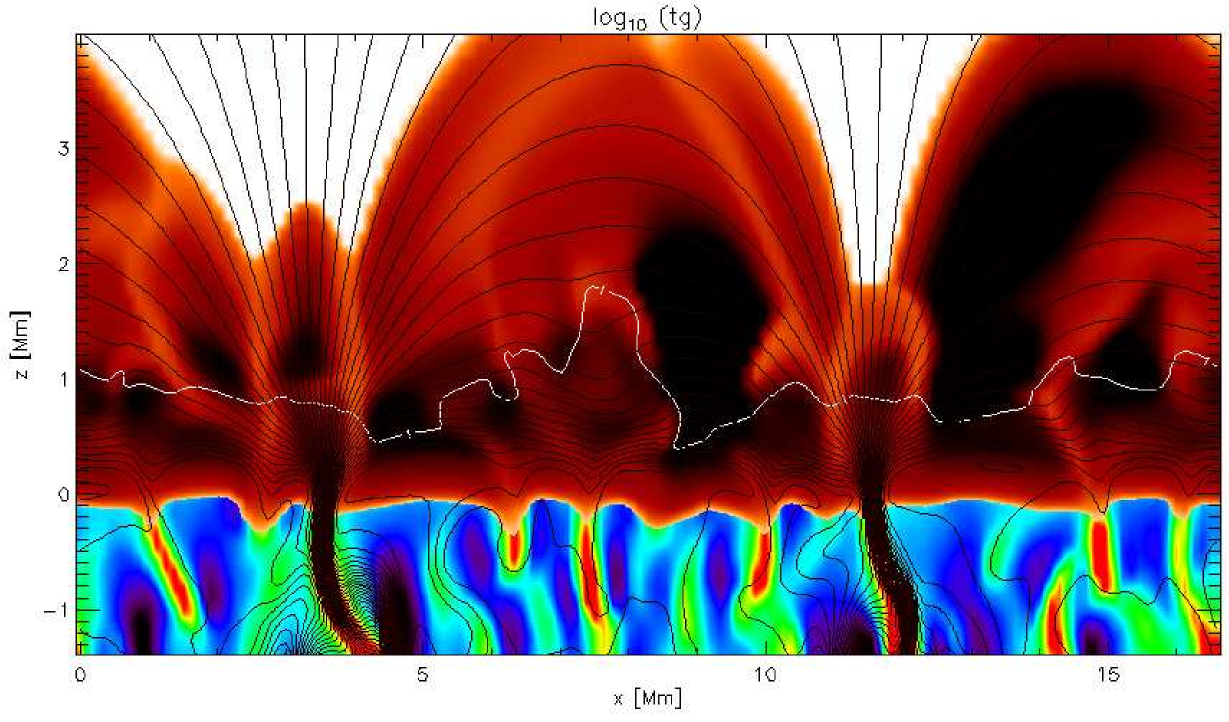

Courtesy, M. Carlsson

Simulations at large scales and high resolution (cont.)

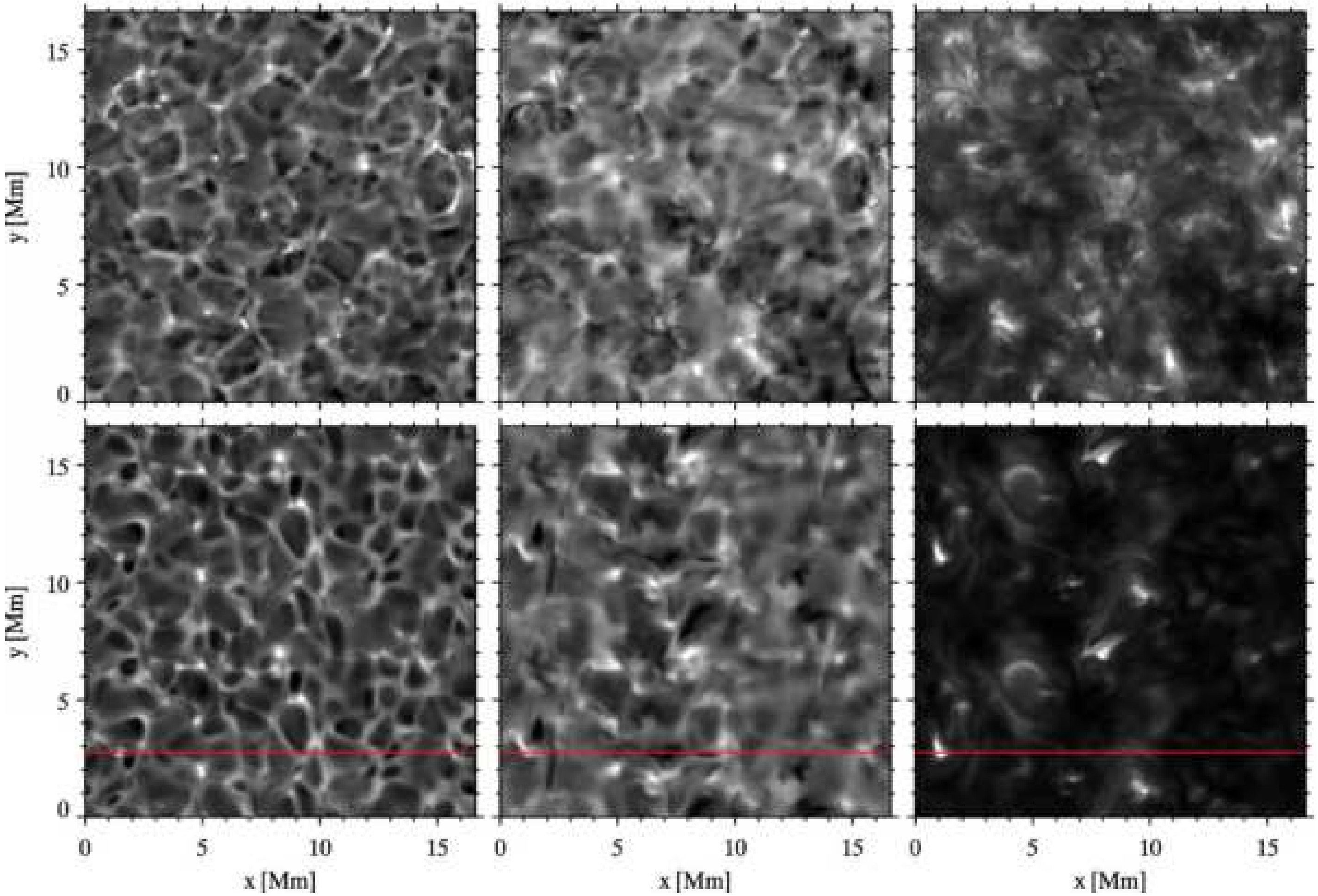

Observed (top row) and synthetic (bottom row) Ca II 854.2 nm images at different positions in the line. *Left:* at $\Delta\lambda = -0.87$ Å; *middle:* close to the line core; *right:* in the line core at $\Delta\lambda = 0$ Å.

References

Braun, D.C., Birch, A.C., Benson, D., Stein, R.F., and Nordlund, Å.: 2007, *Helioseismic Holography of Simulated Solar Convection and Prospects for the Detection of Small-Scale Subsurface Flows*, ApJ 669, 1395-1405

Brun, A.S., Miesch, M.S., and Toomre, J.: 2004, *Global-Scale Turbulent Convection and Magnetic Dynamo Action in the Solar Envelope*, ApJ, 614, 1073-1098

Brun, A.S. & Rempel, M.: 2009, *Large Scale Flows in the Solar Convection Zone*, Space Science Reviews 144, 151-173

Hansteen, V.H., Carlsson, M., and Gudiksen, B.: 2007, *3D Numerical Models of the Chromosphere, Transition Region, and Corona*, in The Physics of Chromospheric Plasmas, ASP Conf. Series, Vol. 368, P. Heinzel, I. Dorotovič, and R.J. Rutten (eds.), p. 107

Leenaarts, J., Carlsson, M., Hansteen, V., and Rouppe van der Voort, L.: 2009, *Three-Dimensional Non-LTE Radiative Transfer Computation of the CA 8542 Infrared Line From a Radiation-MHD Simulation*, ApJ 694, L128-L131

Nordlund, Å., Stein, R.F., and Asplund, M.: 2009, *Solar Surface Convection*, Living Reviews in Solar Physics, Vol. 6, p. 2

References (cont.)

Rempel, M., Schüssler, M., Cameron, R.H., and Knölker, M.: 2009, www.sciencexpress.org / 18 June 2009 / p. 1

Rempel, M., Schüssler, M., and Knölker, M.: 2009, ApJ 691, 640-649

Zhao, J., Georgobiani, D., Kosovichev, A.G., Benson, D., Stein, R.F., and Nordlund, Å.: 2007, *Validation of Time-Distance Helioseismology by Use of Realistic Simulations of Solar Convection*, ApJ 659, 848-857

Boundary conditions for the magnetic field for run v10 and h20

v10

$$B_{x,y} = 0\,; \ \frac{\partial B_z}{\partial z} = 0$$

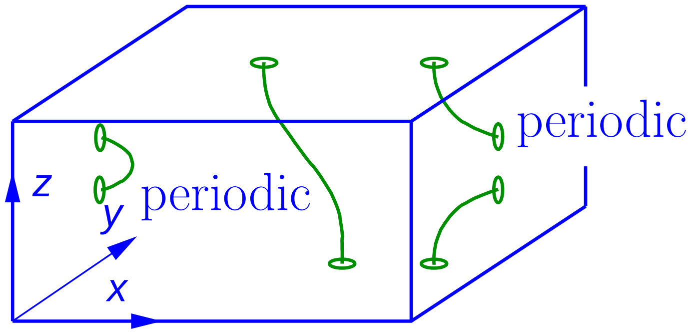

$$B_{x,y} = 0\,; \ \frac{\partial B_z}{\partial z} = 0$$

h20

$$\frac{\partial B_{x,y,z}}{\partial z} = 0$$

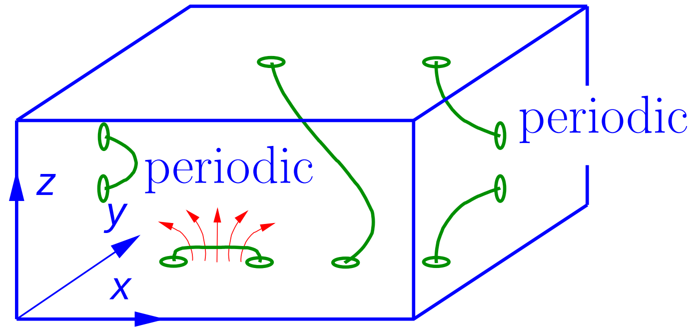

outflow: $\frac{\partial B_{x,y,z}}{\partial z} = 0$

inflow: $B_y = B_z = 0,\, B_x = \text{const.}$

$B_x = 20$ G

$\longrightarrow$ backto § 17.

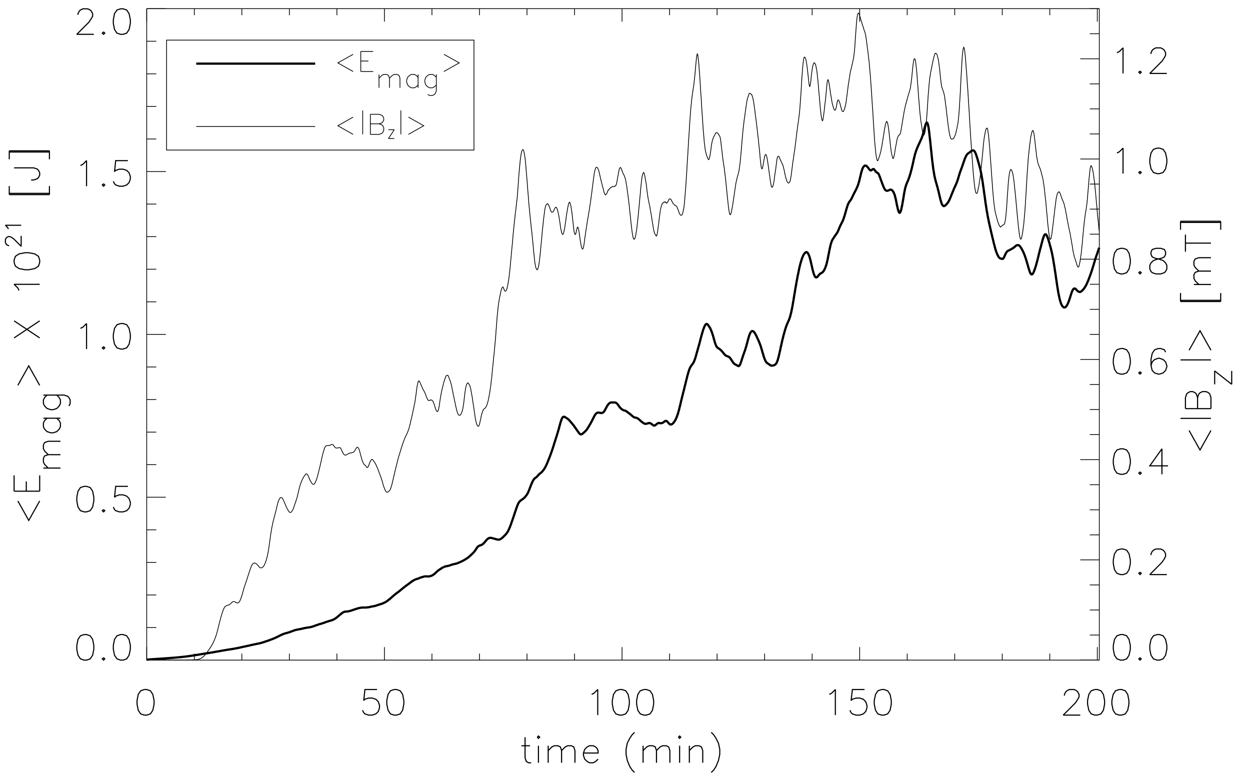

Growth of magnetic energy in the computational box of *run h20* and mean absolute vertical magnetic field strength at a fixed geometrical height corresponding to the mean optical depth unity, $\langle|B_z|\rangle(\langle\tau_{500\,\mathrm{nm}}\rangle = 1)$.

$\longrightarrow$ backto § 17.